Title
Point Defect Engineering of Energy Materials from First-Principles Calculations

Author
Broberg, Daniel

Publication Date
2019

Point Defect Engineering of Energy Materials from First-Principles Calculations

by

Daniel Peter Broberg

A dissertation submitted in partial satisfaction of the

requirements for the degree of

Doctor of Philosophy

in

Engineering - Materials Science and Engineering

and the Designated Emphasis

in

Energy Science and Technology

in the

Graduate Division

of the

University of California, Berkeley

Committee in charge:

Professor Mark Asta, Chair
Professor Jeffrey Neaton
Professor Kristin Persson

Spring 2019

Point Defect Engineering of Energy Materials from First-Principles Calculations

Abstract

Point Defect Engineering of Energy Materials from First-Principles Calculations

by

Daniel Peter Broberg

Doctor of Philosophy in Engineering - Materials Science and Engineering

and the Designated Emphasis in Energy Science and Technology

University of California, Berkeley

Professor Mark Asta, Chair

Atomic scale imperfections, know as point defects, dictate the performance and efficiency of many modern energy materials. The challenges of climate change require the continued improvement and identification of materials which can have point defects engineered in a favorable fashion for the application of interest. With the rise of computer-aided materials design, the possibility of performing high-throughput, first-principles computation on point defects remains an attractive direction for improved screening of new energy materials. Yet major barriers have prevented the large scale implementation of point defect calculations in non-metals - namely, errors arising from the finite size of the computation cell, compounded with errors associated with the underestimation of the band gap. Moreover, the lack of an organized computational framework for storing and analyzing such calculations, as well as the lack of a reliable benchmark for understanding the quantities which can be reliably computed, have prevented high-throughput point defect calculations from being performed in a practical context. In this dissertation, the notion of performing first principles calculations of point defects in semiconductors and insulators in a high-throughput format is investigated. This begins with an overview of the theoretical requirements for performing first principles computation of defects, as well as the presentation of a set of open source command line tools for doing the same. Then three different application areas in the energy space - thermoelectrics for waste heat recovery, solid state electrolyte batteries, and solar cells - are explored with first principles calculations of point defects. Finally, scaling of the previously presented command line tools to a fully automated framework is demonstrated and used for a large benchmark study of fully-automated point defect calculations with semi-local functionals as compared to a set of previously published point defect calculations with hybrid-functionals. This benchmark work outlines the strengths and weaknesses associated with such an automation framework, and advocates for the use of such a framework for qualitative screening of doping limits and general carrier type for high-throughput computational discovery and design of new energy materials.

Contents

Acknowledgments

I would like to thank my advisor, Mark Asta, for his mentorship and patience with the work I have done here at Berkeley. This would also not have been possible with out the various collaborators and mentors I have met with over the past few years, who helped me see this dissertation through to the end: Geoffroy Hautier, Shyam Dwaraknath, Kristin Persson, and Jeffrey Neaton. I would also like to thank the other members of my qualifying exam committee for their helpful feedback and inspiration throughout my graduate experience: Junqiao Wu and Gerbrand Ceder.

In addition, I would like to thank my friends and family for their persistent presence and support during my graduate career. In particular, I want to thank my parents Diane and Peter, my wife Karishma, and my sister Abby, for always being there when it counted so much.

The work presented in this dissertation was primarily funded by the U.S. Department of Energy, Office of Science, Office of Basic Energy Sciences, Materials Sciences and Engineering Division under Contract No. DE-AC02-05-CH11231 : Materials Project program KC23MP. This research used resources of the National Energy Research Scientific Computing Center, which is supported by the Office of Science of the U.S. Department of Energy under Contract No. DE-AC02-05-CH11231.

CHAPTER 1

Introduction

Climate change is the greatest challenge facing humankind today. The ramifications of increasing global temperatures exacerbate current world issues surrounding food security, water access, wildfires, displaced land from sea level rise, reductions in biodiversity, human health and economic growth [1, 2]. In the 2015 Conference of the Parties in Paris, governments around the world reached an agreement to limit temperature increases below 1.5 ^{o}C above pre-industrial levels [3]. According to the Intergovernmental Panel on Climate Change (IPCC) Special Report that followed, limiting global temperature increases to 1.5 ^{o}C will require adhering to a total carbon budget which has been more than 82% drained since pre-industrial years, putting us on track to exceed the amount of allowed carbon by 2050.

To protect the world's remaining carbon budget, drastic action must be taken to electrify the transportation sector and increase the percentage of carbon-free electricity generation and distribution. While great strides have been made towards these goals, improvements in material efficiencies within energy generation and distribution (e.g. photovoltaics and waste heat recovery) as well as improving fundamental limits for energy storage, will remain as challenges for the materials science community for decades to come. The work that follows motivates the importance of high-throughput, theoretical investigations of point-defects for designing new materials which can aid in meeting the requirements of future energy systems.

1.1 Defects in Nature

Any material imperfection which deviates from the surrounding crystalline order can be called a defect [4]. This definition applies to any material which demonstrates some degree of crystalline order [5]. These imperfections give rise to many of the macroscopic properties which concern all of engineering, such as the mechanical response of a material, ionic, electronic and thermal transport, and stability against corrosion and degradation [5]. We can differentiate atomic-scale imperfections (point defects) from other defects which occur on larger length scales (extended defects) [4]. Point defects, the sole focus of this thesis, include intrinsic defects that are entropically stabilized at any finite temperature, and extrinsic solutes that may be intentionally added to dope the material [4].

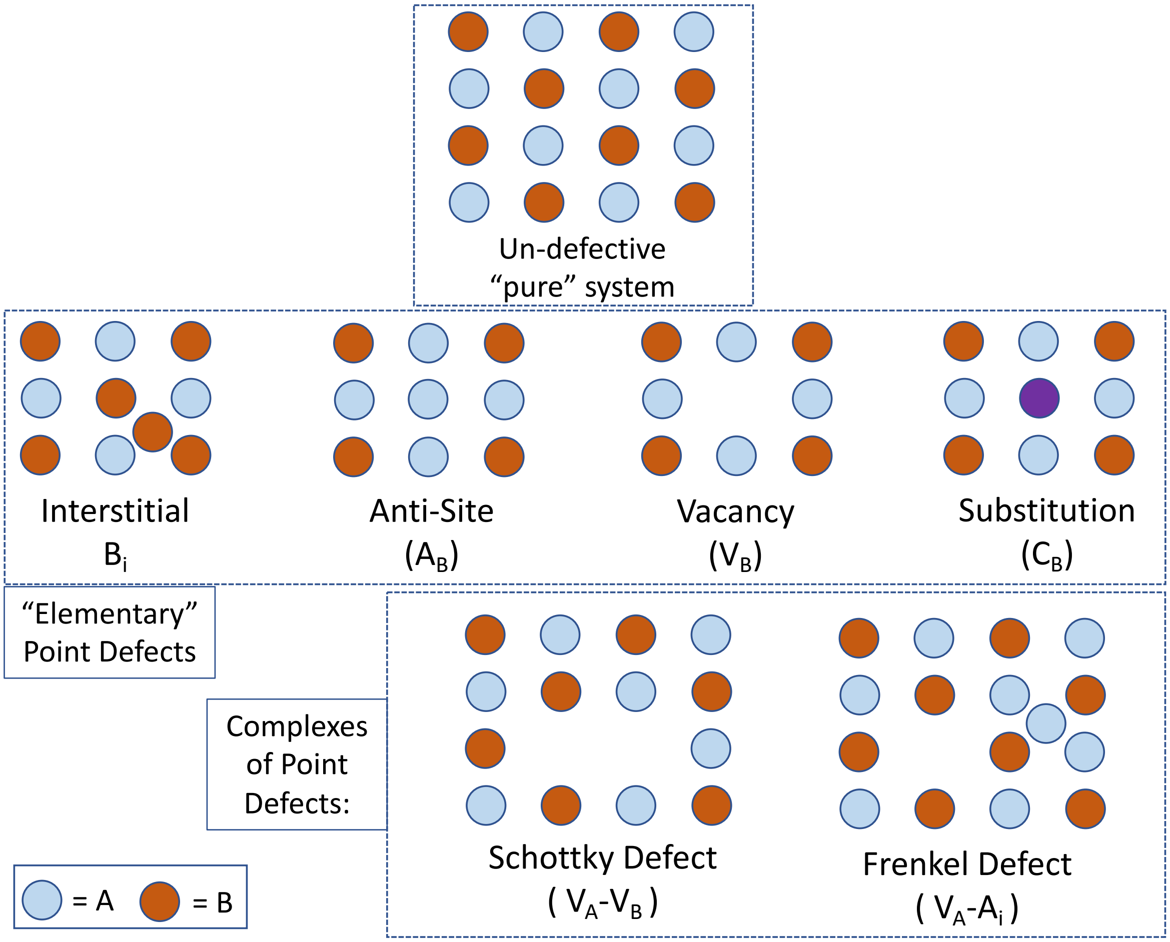

Figure 1.1: Representative defect types for a hypothetical AB system (top). Elementary point defects are single additions or removals of atomic specie from the pure system (middle row). Complexes are combinations of multiple elementary defect types (bottom row).

A set of representative point-defect types are shown schematically in Figure 1.1. Elementary point defects are perturbations of a single site in the un-defective “pure” system, with interstitials corresponding to the occupation of a previously unoccupied sub-lattice of the crystal. Intrinsic defects correspond to the addition and removal of native species (A or B in Figure 1.1), while extrinsic defects correspond to the addition of a foreign specie to the crystal system (C in Figure 1.1). A linear combination of elementary defects becomes a *defect complex*, which may become more energetically favorable than their isolated counterparts as a result of local structure accomodation. Two famous examples of defect complexes are the Schottky and Frenkel defects, which correspond to a pair of vacancies and a combination of a vacancy and an interstitial, respectively.

Typical defect concentrations vary widely from $\sim 10^{10}$ cm^{-3} in undoped semiconductors to degenerately doped concentrations exceeding 10^{22} cm^{-3}. Given such a large quantity of point defects, the difference between a set of "Elementary" point defects and a complex of defects is primarily differentiated by defects which have a large binding energy - that is, a pair of elementary defects which prefer to form near each other is considered a complex, while elementary defects do not have a preference for forming next to neighboring defect types. This is almost a semantic difference, but such a distinction is important to make when considering the vast permutation space that exists for arrangements of defect complexes. This thesis focuses attention solely on the formation of elementary point defects, which is a necessary first step to modeling complexes.

It is typical to define a labeling procedure for quickly defining defects [6]. In this notation the new atomic site occupation is sub-scripted by the original site's occupation (For example, Vac_B is a B-site vacancy and A_B is an A-on-B site antisite in Figure 1.1). For defects in non-metals, charge can become trapped on the defective site and in the adjacent bonding states. For such a case, it is standard practice to include a superscript for the charge state relative to the neutral case, taken to be the formal charge after full removal (and/or addition) of atomic specie(s), with valence electrons included. With this labeling procedure, it is then possible to write reaction equations for the formation of point defects which conserve charge, mass and site.

For example, in rocksalt MgO the formal oxidation state of oxygen is -2, so that upon the removal of a neutral oxygen atom, Vac_O^{+0} is formed with two electrons trapped on the defect. Removal of these extra electrons with an electric field or a temperature fluctuation would cause an "un-occupied" defect state with charge +2: Vac_O^{+2}. The defect equilibria reaction is written as:

$$\begin{array}{ccccc} Mg_{Mg} + O_O & \leftrightarrow & Mg_{Mg} + Vac_O^{+0} + \frac{1}{2}O_2 & \leftrightarrow & Mg_{Mg} + Vac_O^{+2} + 2e^- + \frac{1}{2}O_2 \\ \text{(un-defective state)} & & \text{(occupied defect state)} & & \text{(un-occupied defect state)} \end{array}$$

Where mass conservation is reflected as oxygen being removed from the crystal to form molecular oxygen (O_2), in the gas phase, during the formation of the defect. The above equations give an intuition for the charge compensation requirement for defects forming in non-metals. The un-occupied defect state requires charge compensation by free electrons (e^-), known as *electronic* compensation. Alternatively, charge compensation by other defects can occur, known as *ionic* compensation. This can be written as:

$$\begin{aligned} nil &\leftrightarrow Vac_{Mg}^{-2} + Vac_O^{+2} && \text{(Schottky defect)} \\ O_O^{+0} &\leftrightarrow O_i^{-2} + Vac_O^{+2} && \text{(O-Frenkel defect)} \end{aligned}$$

Where the left side of each equation reflects a perfect crystal and the reactions conserve mass and number of lattice sites. The equilibrium constants for each reaction are determined by the defect formation energies and dictate the more dominant reaction, and, subsequently, determine the concentration of electrons in the crystal.

Given the above discussion, decades of work have gone into attempting to produce universal rules for defects formation in crystals. Such a set of rules would have a large influence on the engineering of new materials with ideal point defect properties for a given application. Early examples of such efforts were Kröger's rules and Pauling's rules, both of which are born out of observed empirical evidence [4, 6]. More recent examples include work by Zunger, which makes observations about the relative stability of defects with regard to the position of band edges on an absolute scale [7]. However, universal rules for defect formation always include important exceptions. For example, general rules for doping predicted p-type GaN to be an impossible achievement, despite being ultimately achievable at concentrations exceeding 10^{18} cm^{-3} and the subject of the 2014 Nobel Prize in Physics [8, 9].

1.2 Importance of Point Defects for Energy Applications

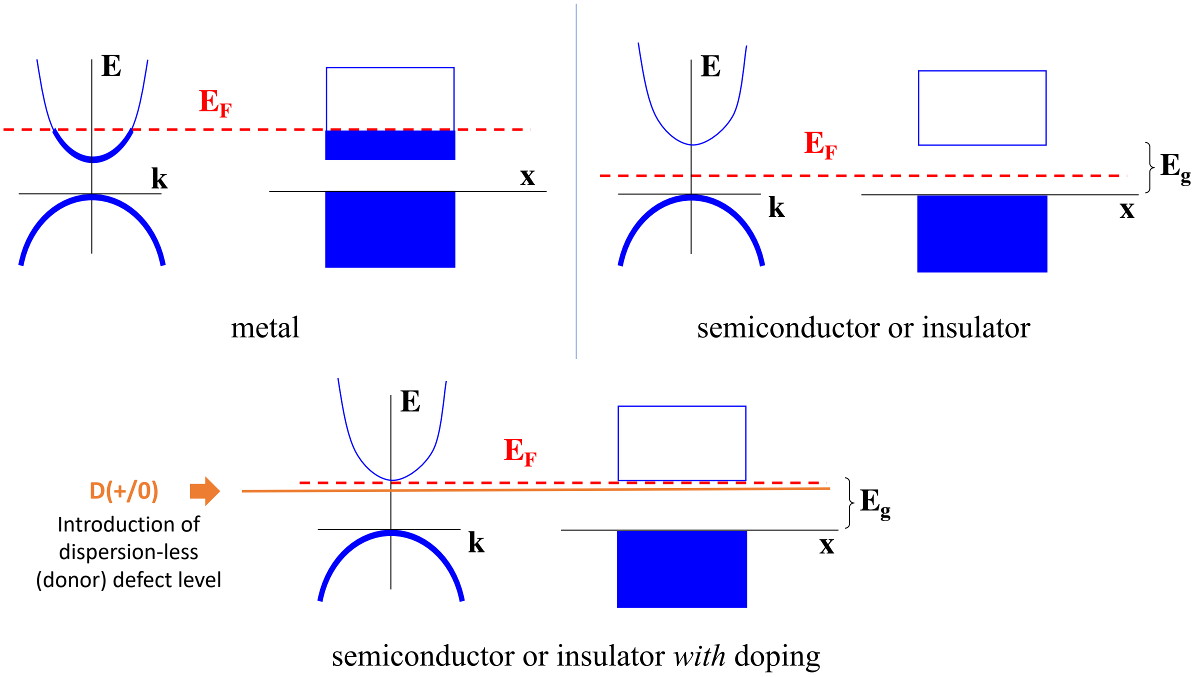

Figure 1.2: Schematic representations of the Fermi level in real and reciprocal space band structures of metals (top left), non-metals (top right), and non-metals with doping (bottom).

Point defects directly impact a given material's performance for energy applications. To provide a simple explanation for the impact on carrier concentrations, Figure 1.2 shows representatives schematics of the Fermi level position relative to band edges in reciprocal and real space band structures. In metals, carrier concentrations are high as a result of the available energy levels within $k_B T$ of the Fermi level (top left of Figure 1.2). The resistance to free carrier motion in a metallic material is strongly dependent on the scattering from defect sites [10]. While the defect-dependence of free carrier dynamics also exists for semiconductors and insulators, the free-carrier concentrations themselves are strongly dependent on the defect concentrations, as discussed for MgO in the previous section. Since the Fermi level of non-metallic materials (without defects) lie in the band gap of unavailable electronic states, thermal energy ($\sim k_B T$) is insufficient to excite free carriers to appreciable concentrations in the absence of defects (top right of Figure 1.2). When dopant defects add occupied electronic levels near the conduction band, thermal excitation is sufficient to excite free electrons to the conduction band, resulting in a modified Fermi level position (bottom of Figure 1.2).

Besides the strong dependence of carrier concentrations on point defects in non-metals, optoelectronic efficiencies are also strongly impacted by the appearance of defect levels in the gap. For example, light emitted diode (LED) photon creation efficiency is strongly dependent on the presence of defect levels which lie deep within the band gap. To illustrate this, Figure 1.3 shows two recombination pathways for electrons and holes in an LED device. In a perfectly functioning LED, the electron and hole directly recombine across the gap via radiative recombination, producing a photon with an energy equal to the size of the band gap (left side of Figure 1.3). In the case with deep defect levels present, a non-radiative process can occur whereby the electron and hole recombine on the defect site, with energy being dissipated in the form of thermal motion (right side of Figure 1.3). This former case therefore decreases the number of photons emitted from an LED device, reducing efficiencies.

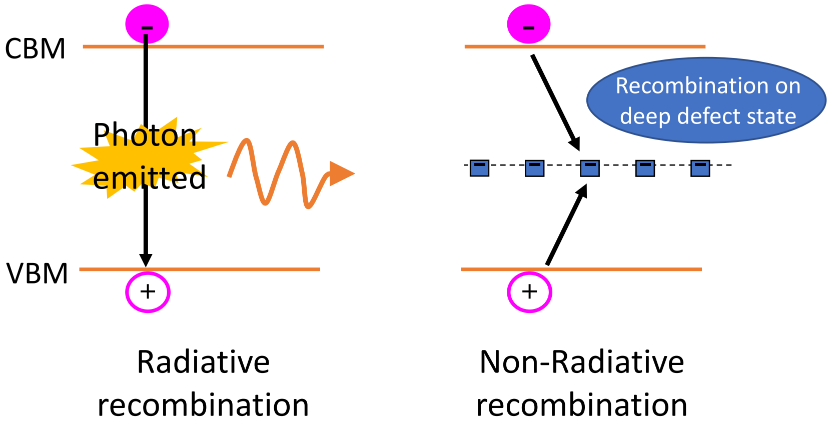

Figure 1.3: Two schematic representations of LED operation: (left) radiative recombination causing photon emission as compared to (right) non-radiative recombination of electron and hole on a deep defect state, which dissipates as thermal energy and leads to worse efficiencies in LED materials.

This mechanism for decreased efficiencies in LED devices is equally important for the operation of solar cell devices, which roughly act as modified LEDs acting in reverse - absorbing solar photons to create an electron-hole pair which is then swept out of the device. For this reason, any solar cell which is available in the global market place received some degree of "defect engineering" for removing defects with deep levels [11–13]. As discussed later in this thesis, defect engineering - or the promotion of certain defects over others - can be done through varying the chemical environment surrounding the crystal growth [8, 14]. Silicon solar cells, traditionally riddled with harmful defects when grown without careful control, serves as a pinnacle example of a material which required decades of empirical observation to remove impurities and achieve extremely pure concentrations that exceed defect detection limits [15, 16].

Rather than relying on decades of empirical trial-and-error to discover the next energy material of interest, modern investigations are able to make use of theoretical calculations, like Density Functional Theory (DFT), which can provide qualitative and quantitative insights into the nature of defect formation in semi-conductor materials during a materials design investigation.

1.3 Fundamentals of First-Principles Calculations

First-principles calculations, such as Density Functional Theory (DFT), have been growing in popularity in the past few decades, due to improvements in parallel computer hardware and the increased availability of computational software [17,18]. A fundamental tenet of DFT is to reduce the many-body Schrödinger equation describing the energy of a material in terms of the interactions between the many electrons and nuclei to a problem with a single electron interacting with an effective mean field [17]. This relies on two theorems by Hohenberg and Kohn, which state that the ground state energy is a functional of the electron density, and that the real ground state density corresponds to the exact ground state energy [17, 19, 20]. The Kohn-Sham equations that result from minimizing the energy functional with respect to the electron density are written as:

$$[\frac{\hbar^2}{2m}\nabla^2 + V(r) + V_H(r) + V_{XC}(r)]\psi_i(r) = \epsilon_i\psi_i(r) \tag{1.1}$$

where terms on the left hand side are the kinetic energy, the coulomb interaction with nuclei, the coulomb interaction with other electrons (Hartree potential), and the exchange and correlation (XC) potential, respectively. This last term is designed to include all other quantum mechanical effects which are not included in the previous three terms [17] and is formally defined as:

$$V_{XC} = \frac{\delta E^{XC}[n](r)}{\delta n(r)}$$

the functional derivative of the exchange and correlation energy with respect to the electron density. The Kohn-Sham wavefunctions (ψ_i) dictate the true ground state density, which is a required input for the potential terms in Equation 1.1. This requires a self-consistent treatment where an initial guess for the density is made, the Schrödinger equation is solved, and a new set of wavefunctions are produced and fed back into the self-consistent treatment until the total energy (or forces) converge to a given tolerance.

The power of DFT is in the reduction of 3N degrees of freedom (3 spatial degrees of freedom for N electrons) to 3 spatial degrees of freedom in the electron density, but the weakness lies in the lack of a rigid definition for the exchange and correlation potential, V_{XC}. A good starting point for approaching V_{XC} is based on exchange-correlation energy of a uniform electron gas; in the Local Density Approximation (LDA) it is assumed that the total exchange correlation energy of an inhomogeneous system can be written as an integral of the exchange correlation energy density of a uniform gas, evaluated at the value of local density [17]. A small improvement over LDA makes use of the local gradient of the electron density, as well as its value: the Generalized Gradient Approximation (GGA), with one popular implementation of GGA published by Perdew, Burke, and Ernzerhof known as PBE-GGA [21, 22]. While these "semi-local" XC functionals are computationally efficient, they are known to suffer from several limitations - most notably, the underestimation of the band gap or the under binding nature of lattice constants in GGA.

It is possible to expand the amount of physics included in the exchange and correlation description, but this often comes at an added computational cost. For example, Hartree-Fock methods have relatively poor computational scaling with the number of electrons in a system, but provide an exact treatment of the exchange energy [17]. Despite having a perfect description of the exchange interaction of electrons, there are no correlation effects included. This has inspired yet another class of approaches know as "hybrid approaches", which involve the mixing of computationally efficient semi-local functionals, like GGA-PBE, with the exact exchange provided by Hartree-Fock. One popular hybrid implementation know as HSE06 has been shown to balance computational efficiency with significant improvements in thermochemical results, as well as improved band gap and lattice constant accuracy [23, 24]. Using DFT to do research requires a careful balance of an adequate description of the physics of interest for the XC potential with the computational requirements that one desires.

In Chapter 2 we outline many of the requirements for performing point defect calculations in non-metals with DFT. A popular approach is to make use of periodic boundary conditions (PBCs) in an embedded supercell [8]. In order to minimize interactions with periodic neighbors, it is necessary to extend the supercell to a large enough size such that the defect wavefunction is fully contained within a single supercell. Regardless of the size of the supercell, many computational artifacts may persist, such as the coulomb interactions between mirror-image defects in neighboring supercells. Corrections to account for these finite-sized effects have been discussed extensively in the literature [8, 25, 26]. For defects in semiconductors and insulators, an under-estimation of the band gap can cause a defect state, which normally would be confined within the band gap, to hybridize with host band states, causing extended delocalization of the defect wavefunction outside of the calculation supercell. This causes compounded errors of the defect state within semi-local functional approaches which may not occur within hybrid functional approaches, leading most modern "state-of-the-art" defect calculations to be performed with hybrid functionals [8, 27–31].

1.4 High-throughput for Materials Discovery

All modern technological materials for energy generation and distribution were found through "Edisonian" approaches that have relied on extensive trial and error approaches, guided by limited theoretical predictions. A more optimistic way to state this is: decades of semi-intelligent "guess-and-check" work led to the development of materials that changed the way we live and work. This includes the use of silicon within solar cells and transistors, lithium iron phosphate cathode materials for lithium-ion batteries, and lead-telluride for thermoelectric devices. Designing new materials which can replace these deeply-entrenched technologies is a monumental challenge which requires rethinking the traditional manner of materials engineering [18].

To approach this materials design challenge with solely experimental efforts would be irresponsible, as the sheer size of the combinatorial design space, as well as the number of parameters which must be engineered for the application of interest, would lead to decades of costly experimentation without much of a guarantee for success. An alternative approach, which has been increasing in popularity in the past decade, is to make use of "high-throughput" computation - wherein a single set of calculations is performed many times, with the results stored and data-mined for quantities of interest. The high-throughput screening materials design approach for next generation energy materials has already shown promise in many applications, including finding better electrode materials for batteries, as well as discovering new materials for solar and thermoelectric applications [18, 32–35]. Moreover, the appearance of openly available data sets, such as the Materials Project (www.materialsproject.org), have allowed for first principles calculations to be more readily disseminated to the materials engineering community [36].

As discussed earlier for silicon, defect engineering in electronic materials is an essential step for improving the potential use of high efficiency optoelectronics devices and other materials which require charge conduction to be actively controlled. Moreover, the practical limits for achieving certain properties - such as dopability - can be eliminated based on a thermodynamic assessment of practical defect formation. Despite this intrinsic requirement of knowledge about defect physics in energy materials, the majority of high-throughput efforts to date have been focused on bulk properties such as thermodynamic stability and band structure characteristics [37–39]. The few studies which include point defect information during the screening stages are limited to tens of defect calculations at a time [27–29, 40]. Two reasons exist for the lack of high-throughput studies on defects: (*i*) there has historically not been a reliable, user-friendly code base for automating and parsing point defect calculations with DFT and (*ii*) there has not been a systematic benchmark study performed for the limits of semi-local functional calculations, making the results of such calculations unclear in their predictive value. Both of these challenges form the primary motivation for this dissertation.

1.5 Dissertation Outline

The rest of this dissertation presents work under the unifying theme of setting up a framework for future high-throughput point defect calculations to be performed with regard to energy applications. In Chapter 2, the fundamental requirements for performing point defect calculations are introduced and a novel new code for automating the setup, parsing, and analysis of charged defect calculations is outlined (the Python Charged Defect Toolkit). Chapter 3 outlines the use of these automation tools for understanding the behavior of materials with relevance to energy; focusing on materials for thermoelectrics, solid-state batteries, and solar cells. In Chapter 4 we perform an in-depth benchmark analysis of semi-local, automated point defect calculations as compared to “gold standard” hybrid calculations previously published by several different experts in the community. Chapter 5 then summarizes the work done and suggests future work that remains to be investigated for the prospect of high-throughput, first-principles studies of point defect formation in energy materials.

CHAPTER 2

Defect Fundamentals and Command Line Tools

Point defects have a strong impact on the performance of semiconductor and insulator materials used in technological applications, spanning microelectronics to energy conversion and storage. The nature of the dominant defect types, how they vary with processing conditions, and their impact on materials properties are central aspects that determine the performance of a material in a certain application. This information is, however, difficult to access directly from experimental measurements. Consequently, computational methods, based on electronic density functional theory (DFT), have found widespread use in the calculation of point-defect properties. Here we have developed the Python Charged Defect Toolkit (PyCDT) to expedite the setup and post-processing of defect calculations with widely used DFT software. PyCDT has a user-friendly command-line interface and provides a direct interface with the Materials Project database. This allows for setting up many charged defect calculations for any material of interest, as well as post-processing and applying state-of-the-art electrostatic correction terms. Our paper serves as a documentation for PyCDT, and demonstrates its use in an application to the well-studied GaAs compound semiconductor, as well as 20 additional zinc blende and oxide systems. We anticipate that the PyCDT code will be useful as a framework for undertaking readily reproducible calculations of charged point-defect properties, and that it will provide a foundation for automated, high-throughput calculations.

2.1 Forward

The work presented in this chapter was published as “PyCDT: A Python toolkit for modeling point defects in semiconductors and insulators” by D. Broberg, B. Medasani, N. E. R. Zimmermann, G. Yu, A. Canning, M. Haranczyk, M. Asta, and G. Hautier in Comp. Phys. Comm., vol. 226, pages 165-179 (2018), and is reproduced here with permission of the co-authors.

2.2 Introduction

Point defects in semiconductors and insulators govern a range of mechanical, transport, electronic, and optoelectronic properties [41–45]. Due to the fact that the properties of these defects are difficult to characterize fully from experiment [8, 45], computational tools have been widely applied. Many applications such as lanthanide-doped scintillator materials [46, 47], transparent conducting oxide materials [48–50], photovoltaic materials [13, 51], and new thermoelectric materials [40, 52] have benefited from leveraging theory for calculating point defect properties in next generation technologies.

For this reason, calculations using electronic density functional theory (DFT) have arisen as a reliable route to explore the dopability of materials at the atomic scale [8, 25, 29, 53]. However, two sources of error in the associated point defect calculations limit the application of charged defect DFT efforts in a high-throughput framework. First, semi-local exchange-correlation approximations (e.g., generalized gradient approximation (GGA)) can severely underestimate the band gap so that usage of post DFT methods becomes pivotal (e.g., GW [54–56] and GGA+U methods [57, 58], and hybrid functionals [59]). Second, applying periodic boundary conditions with finite sized defect supercells to model point defects makes a defect interact with its own images [8, 60], thus, causing departure from the key assumption made in the dilute limit formation energy formalism [8, 60]. In the case of charged point defects, the finite sized supercell assumption also introduces the need for correcting the electrostatic potential [8, 53]. Typically, the strongest defect-defect interaction is the Coulomb interaction between charged point defects. Based on well-known scaling laws, these interactions were first treated with computationally costly supercell scaling methods, which require multiple calculations for each defect [60]. A faster route to computing defect formation energies became available with the development of *a posteriori* correctional techniques. While the *a posteriori* corrections allow for fewer calculations to be performed, their usage requires experience in addressing issues arising from delocalization of the defect wavefunction [53]. Furthermore, the calculations are often resource demanding and tedious because of the large number of pre- and post-processing steps involved.

To address these problems we have developed the Python Charged Defects Toolkit (PyCDT), which enables expanded applications in the context of materials discovery and design. Our python-based tools automate the setup and analysis of DFT calculations of isolated intrinsic and extrinsic point defects (vacancies, antisites, substitutions, and interstitials) in semiconductors and insulators. While other efforts have recently been made available with similar objectives [61–63], PyCDT is unique in its direct queries to the Materials Project [64] database (expediting chemical potential and stability analysis for Perdew–Burke–Ernzerhof (PBE) GGA calculations) [21].

A central objective of defects modeling in non-metallic systems is determining the relative stability of different defect charge states. PyCDT therefore implements the defect formation energy formalism reviewed in Sections 2.3.1, 2.3.2, 2.3.3 and 2.3.4. To minimize the errors in defect formation energies arising from the periodic boundary conditions, PyCDT supports the commonly used correction scheme due to Freysoldt et al. [65] and its extension to anisotropic systems by Kumagai and Oba [66] (Section 2.3.4). Our tools also include charge-state assignment procedures developed on the basis of extensive literature data (Section 2.3.5) and an effective interstitial-finding algorithm [67] (Section 2.3.6). Furthermore, PyCDT provides a user-friendly command-line interface that provides ready access to all tools. We demonstrate the setup and analysis of the defect calculations from the command line in Section 2.4 using gallium arsenide (GaAs) as an example system and by employing the widely-used VIENNA AB INITIO SIMULATION PACKAGE (VASP) [68, 69] as a backend DFT software. In Section 2.5, we validate the finite-size charge correction schemes implemented and verify the results obtained for GaAs. We emphasize that our approaches and implementations are entirely general, thus, seamlessly facilitating extensions to other DFT packages.

2.3 Background and Methods

In general, point defects can be divided into two categories: intrinsic and extrinsic [45]. Intrinsic (or native [8, 45]) point defects (Figure 2.1: top) involve only chemical species that are part of the perfect bulk material (e.g., Si in silicon). For elemental materials, there are two basic intrinsic defect types: vacancies (e.g., $\mathrm{vac}_{\mathrm{Si}}$, denoting a vacancy on Si site) and self-interstitials (e.g., Si_i). For compounds (e.g., GaAs), there is an additional defect type: antisites (e.g., $\mathrm{As}_{\mathrm{Ga}}$). Because intrinsic point defects are equilibrium defects due to configurational entropy, they can be well described and their occurrence understood in the framework of equilibrium thermodynamics (formation energies, E^{f}, used to predict equilibrium concentrations, c).

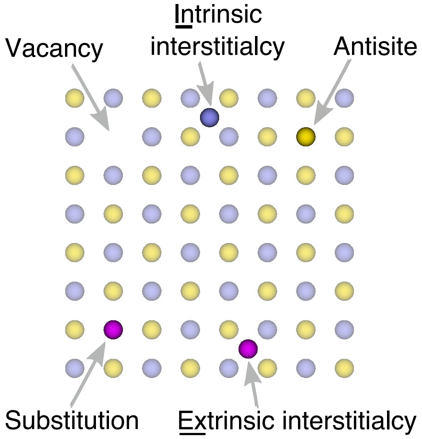

Figure 2.1: Intrinsic point defects (top: vacancy, intrinsic interstitialcy, antisite) and extrinsic point defects (bottom: substitution, extrinsic interstitialcy).

Extrinsic defects (Figure 2.1: bottom), which are also referred to as impurities [8, 45], introduce a foreign chemical species into the perfect bulk material [41]. These include substitutional defects (e.g., $\mathrm{Mn_{Ga}}$) and extrinsic interstitials (e.g., Mn_i). We distinguish between extrinsic and intrinsic defects because impurities are often inserted on purpose (intentional doping) under well-defined conditions to achieve desired material properties; in particular, electrical and optoeletronic properties [45]. The conditions under which extrinsic defects are inserted (e.g., via implantation or quenching) often differ extremely from the thermodynamic equilibrium assumption made in the assessment of intrinsic point defects. Despite the limited conceptual applicability, the thermodynamic framework still represents the most commonly pursued route to assessing "dopability" of materials [8, 13, 40, 46–52].

In contrast to metals, point defects in semiconductors and insulators can carry a charge [45] localized around the defect site. Physically, these charged point defects introduce states within the band gap which can trap charge carriers (electrons and holes). Defect states that are close to the band edges are able to ionize to create free carriers, while states that are deep in the gap lead to strong carrier trapping. This may be wanted (e.g., in photovoltaics [51]) or not (e.g., solid-state electrolyte batteries [70]). Because many technological applications use intentional doping to improve performance, knowledge of the capacity to dope a material ("dopability") is desirable and motivates the exploration of defect properties with theoretical methods.

2.3.1 Formalism for equilibrium point defects

The thermodynamics of point defects has been the subject of many excellent reviews (see, for example, refs. [8, 25, 53] and references therein), which have presented and discussed the underlying physics and properties in great detail. In the following sections, we focus on describing the procedures implemented in PyCDT for computing quantities of interest for point defects (i.e., formation energies and transition levels) with DFT calculations. The applications of the defect formalism to be described are limited by the intrinsic shortcomings of DFT (e.g., the well-known underestimation of the band gap [53]).

There is a hierarchy of DFT-based methods that can be used within the defect formalism implemented by PyCDT. The simplest approximation in DFT is the use of a semilocal functional (i.e., local-density approximation (LDA), GGA), which is computationally most efficient, but has well-known limitations due to band gap inaccuracies. Higher levels of theory include hybrid-functionals and meta-GGA, both of which can be used to achieve higher accuracy, however, at an increased computational cost [71, 72]. Despite the limitations of semilocal DFT, defect calculations have proven useful for revealing the dominating defects under different growth conditions encountered in many experiments, such as the III-V semiconductors [73]. While recent developments in hybrid functionals and meta-GGA have shown promise in addressing the inherent limitations in accuracy associated with semi-local functionals [71, 72], recent evidence shows that new improvements to the approximations for exchange and correlation in one system do not always yield universal improvements for other systems with similar chemistries [74]. With this fact considered, semi-local approximations at least have the benefit of having predictable errors which can be corrected with appropriate techniques [53].

While PyCDT's unique interface with the Materials Project (MP) database, which is composed of GGA and GGA+U level data, suggests a restriction to semi-local approaches, PyCDT has many functionalities which help place defect formation energetics closer to those obtained from higher levels of theory. One feature that is particularly useful is the ability for PyCDT to help expedite the setup and parsing stages of defect calculations performed on higher levels of DFT theory (*e.g.* for improved chemical potentials, setting up a user's personal phase diagram calculation based on a composition of interest). These features are described further in the following sections.

2.3.2 Defect Formation Energies

The primary quantity of interest is the formation energy, $E^{\mathrm{f}}[X]$, which is the energy cost to form or create an isolated defect, X, in a bulk or host material. The formation energy of an isolated defect (i.e., in the dilute limit) depends on the defect charge state, q: $E^{\mathrm{f}}[X^q]$. It can be calculated from DFT supercells using:

$$E^{\mathrm{f}}[X^q] = E_{\mathrm{tot}}[X^q] - E_{\mathrm{tot}}[\mathrm{bulk}] - \sum_i n_i \mu_i + qE_{\mathrm{F}} + E_{\mathrm{corr}} \tag{2.1}$$

We illustrate this equation graphically in Figure 2.2 and note that each term will be described in detail in subsequent sub-sections. $E_{\mathrm{tot}}[X^q]$ and $E_{\mathrm{tot}}[\mathrm{bulk}]$ are the total DFT-derived energies of the defective and pristine bulk supercells, respectively. The third term, $-\sum_i n_i \mu_i$, is a summation over the atomic chemical potentials, or the energy cost of an atom, μ_i, being added ($n_i = +1$) or removed ($n_i = -1$) from the bulk undefective supercell. The atomic chemical potential can reflect the growth conditions of the material, allowing this formalism to be used to guide defect engineering approaches (cf., Section 2.3.3). The fourth term, qE_{F}, represents the energetic cost of adding or removing electrons, where E_{F} is the Fermi energy, which serves as the chemical potential of the electron reservoir. The Fermi energy is usually referenced to the valence band maximum from a band structure calculation, such that the formation energy can be plotted as a function of the Fermi energy across the band gap. Finally, E_{corr} is a correction term due to the presence of periodic images that becomes necessary for charged defects in DFT supercell calculations. This correction has drawn significant attention from the defects modeling community, resulting in a number of alternative computational approaches that are discussed in more detail in Section 2.3.4.

2.3.3 Chemical Potentials

The atomic chemical potential is associated with the thermodynamic energy cost for exchanging atoms between the defect and a thermodynamic reservoir. The individual chemical potentials are set by the composition of the material (e.g., the mole fraction of As in GaAs) which itself is determined by the defect formation energies. Hence, two approaches

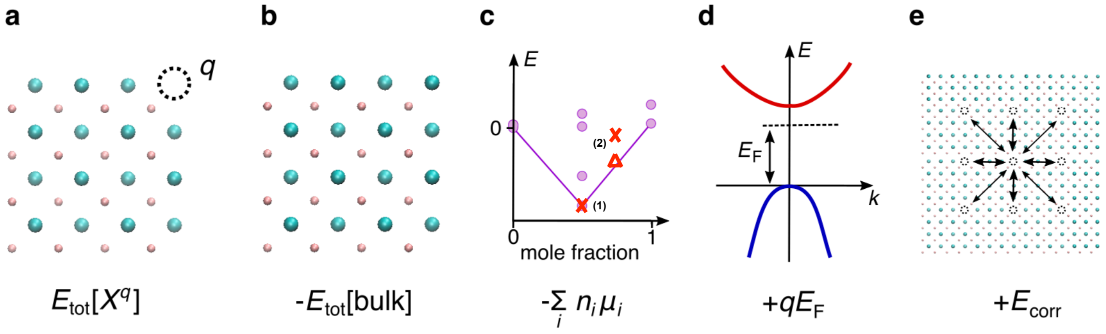

Figure 2.2: Different contributions to the formation energy: (a) energy of defective supercell in charge state q, (b) energy of pristine bulk supercell, (c) atomic chemical potential computed from the ground state hull, (d) electron/hole chemical potential generated from electron reservoir, and (e) correction terms to account for defect-defect interactions arising from periodic boundary conditions as well as for the homogeneous background charge which requires potential re-alignment. The different labeled X's given in 2.2c show stable and metastable compounds. The latter case yields a complication which will be discussed in Section 2.3.3.

can be used to derive the individual chemical potentials. One involves the use of a statistical thermodynamic formalism (*canonical* ensemble approach), to compute the concentration dependent free energy of the compound and to derive the relationship between the chemical potentials and composition [75]. More frequently, bounds on the chemical potentials are set (*grand-canonical* ensemble approach), in a manner first defined by Zhang and Northrup [14], from zero-temperature energies alone. Only the grand-canonical approach is currently included in PyCDT, whereas future versions will also support canonical approaches to chemical potential calculations. Below we demonstrate the grand-canonical approach for the simple example of GaAs.

The bulk energy (or free energy at finite temperature) per formula unit, μ^0_{GaAs}, fixes a relation for the chemical potentials of gallium, μ_{Ga}, and arsenic, μ_{As}, respectively: $\mu^0_{GaAs} = \mu_{Ga} + \mu_{As}$. For Ga-rich compositions, the values of μ_{Ga} are constrained by stability of the compound relative to the precipitation of excess Ga to form a bulk Ga phase. At zero temperature, this constraint can be expressed as $\mu_{Ga} < \mu^0_{Ga}$, where μ^0_{Ga} is the energy per atom of bulk Ga. Thus, one extremum can be selected as the "Ga-rich" limit, where $\mu_{Ga} = \mu^0_{Ga}$. The atomic chemical potential of As is then fixed: $\mu_{As} = \mu^0_{GaAs} - \mu^0_{Ga}$. The same approach holds for As-rich compositions (above: interchange Ga and As labels with each other). While the Ga-As system has a phase diagram with just one unique compound, the more general case has multiple stable compounds, which requires the limits of stability to be expressed in terms of the formation of compounds with neighboring compositions within the phase diagram. In general, the chemical potentials in an n-component system will be defined in PyCDT by defining the limits of stability for the different possible n-phase states of equilibria.

As an example, consider the Sn-Se system which has a 0 K ground-state hull that contains the phases Sn, SnSe, $SnSe_2$ and Se. When calculating defects in the SnSe phase, the "Se-rich" limit would instead be defined by equilibrium with the $SnSe_2$ phase (Equation 2.2), combined with the stability condition for bulk SnSe (Equation 2.3). This forms a system of equations for the chemical potentials of μ_{Sn} and μ_{Se}.

$$\mu^0_{SnSe_2} > \mu_{Sn} + 2\mu_{Se} \tag{2.2}$$

$$\mu^0_{SnSe} = \mu_{Sn} + \mu_{Se} \tag{2.3}$$

This formalism for calculating equilibrium bounds on the chemical potentials requires knowledge of the ground-state hull, which governs the zero-temperature limit of the phase diagram of the system. The advantage of this formalism is that defect formation energies can be obtained entirely from first principles calculations, rendering experimental input unnecessary. The drawback is that one must compute the full phase diagram of the system using the same functional choice used for the defect calculations. In applications of the PyCDT code based on the PBE-GGA exchange-correlation potential, PyCDT uses the ground-state hulls that are made available through the MP database [64]. PyCDT has integrated functionality that queries the MP database for every computed DFT entry in the phase diagram so that no new calculations are required to compute the bounds on the chemical potentials. Note that correct usage of the MP data for defect calculations requires consistency between personal defect calculations and the calculations from the MP. This is easily checked through the compatibility tools available in pymatgen [76]. If the bulk phase is thermodynamically stable and is not already computed in the MP database, PyCDT manually inserts the computed phase into the phase diagram and then provides all of the associated bounds on the chemical potentials. If a user prefers to compute chemical potentials on a different level of theory than is provided by the MP, the core code of PyCDT can be used to setup and calculate atomic chemical potentials through first pulling the composition's phase diagram, and using the structural information to setup a personal phase diagram calculation for the user. In a similar manner, this information can be setup for any DFT code desired by the user through the use of Pymatgen's code agnostic classes.

For highly correlated systems such as transition metal oxides, MP settings default to GGA+U. When computing the phase diagram that contains a mixture of GGA and GGA+U computed phases, MP employs the mixing scheme of Jain et al. [77], which adds an empirical correction to the energies of GGA+U compounds. The mixing scheme was shown to give formation energies that are consistent with experimental data with a mean absolute relative error of under 2%. The resulting correction term to the chemical potentials was found to be important in several defect studies [78, 79].

One complication that should be mentioned is the case where the compound under consideration does not reside on the convex hull. That is, the compound is higher in energy than another compound with the same composition or with respect to phase separation to compounds with other compositions. In this instance, the calculation is predicting the compound to not be present in the equilibrium phase diagram in the limit of zero temperature. For small energy-above-hull values, this situation could indicate that the compound is stabilized by entropic contributions at finite tempearture [80], or could be an artifact of the previously mentioned inaccuracies of DFT [81], or the experimentally synthesized phase exists in a state of metastable equilibrium [82]. Regardless of the reason, a positive energy-above-hull value presents a practical problem for defining the chemical potential.

In such cases, PyCDT issues a warning and the chemical potentials used are with respect to the phases in equilibrium at the given composition in the phase diagram. In figure 2.2c, this situation is graphically represented by the data points labeled “(2)”, where the red X above the hull is the compound of interest and PyCDT uses the red triangle to define a set of compounds in equilibrium for defining the atomic chemical potentials. In these instances, the computed defect physics should be interpreted with caution. The user may wish to define the chemical-potential limits based on more detailed knowledge of the growth conditions or compute the chemical potentials from a full finite-temperature free energy model of the compound of interest.

2.3.4 Periodic Supercell Corrections

Periodic boundary conditions (PBCs) are the standard way to deal with the regular arrangement of crystalline solids in DFT calculations. Once a defect is introduced, PBCs can give rise to sizable interactions of the defect with its periodic images, contrasting the assumption made above for the dilute-defect limit. Because this limit is consistent with the thermodynamic formalism outlined in Sec. 2.3.2, the interactions between neighboring defect images should be minimized to yield accurate formation energies. For charged defects in semiconductors and insulators, Coulombic interaction with neighboring images exists, which decays as 1/L, where L is the supercell periodic length. The charge interactions are the dominant effect that need to be taken into account when correcting the formation energy of defects in non-metals. Elastically-mediated interactions which are due to the strain fields induced when the positions of atoms near the defects also exist, but decay more rapidly in real space, and are often minimal [8]. In cases where these interactions are important, methods have been developed to account for them (see [8] and references therein), which will not be addressed in the following discussion.

To account for the charge correction one approach has been to create successively larger defect supercells. Scaling laws for the electrostatic interactions with respect to system size are then used in order to extrapolate E^{f} to the dilute limit [26,83]. An alternative approach is based on an *a posteriori* analysis of the electrostatic potential for a single supercell calculation [65,84]. An important requirement for the alternative approach is that the charge be sufficiently localized within the vicinity of the defect. If so, a moderately sized defect supercell typically suffices, hence, offering a computationally more efficient route to calculating reliable defect formation energies. The latter methodology, referred to as “correction methods” in the following, is employed in PyCDT.

Correction methods address two issues:

1. the electrostatic energy from the interaction between the charged defect and its images, and

2. a potential alignment term that corrects for a fictitious jellium background required to maintain overall charge neutrality in the system.

Many different methods have been proposed to correct for these two terms, as summarized in several comprehensive reviews (see, e.g., [8,25,53,60] and references therein).

The theoretical starting point for the correction methods considers a periodic array of point charges (cf., Figure 2.2e) with an associated Madelung energy, E_{M}:

$$E_{\mathrm{M}} = \frac{qV_{\mathrm{M}}}{2} = \frac{q^2\alpha}{2\epsilon L} \tag{2.4}$$

where V_{M} is the Madelung potential, ϵ is the dielectric constant, and α is the Madelung constant which solely depends on the geometry of the periodic array. Makov and Payne [85] introduced one of the earliest charge correction methodologies by deriving the next leading order term to the interaction potential. This results in a term that scales as L^{-3}, and, therefore, most supercell scaling approaches fit uncorrected formation energies to the form of $aL^{-1} + bL^{-3}$. Komsa *et al.* [86] used this supercell scaling method for evaluating the performance of different correction methods that are based on single supercell calculations. They concluded that the correction by Freysoldt *et al.* [65] produces the most reliable charge corrections for defects with charges that are well localized within the supercell. From all considered defects, the authors calculated a mean absolute error of 0.09 eV in the formation energy between the estimate from the 64-atom supercell with charge corrections and the estimate from the supercell-scaling method (i.e., using extrapolation toward the dilute-defect limit, but without applying any charge correction).

PyCDT includes a Python implementation of the correction scheme derived by Freysoldt *et al.* [65] and implemented in the open-source DFT software S/PHI/nX [87]. The approach is based on a separation of the long-range and short-range interactions between charged defects, using information directly outputted from a DFT calculation. Originally, an isotropic dielectric constant was assumed. Recently, Kumagai and Oba [66] extended the approach to anisotropic systems, by considering the full dielectric tensor. The analytic expression of the Madelung potential under isotropic conditions facilitates the use of a Gaussian distribution for the defect charge, whereas the analytic expression of Madelung potential for anisotropic systems is limited to point charges.

The authors of the two correction methods suggest different approaches to calculating the potential alignment correction. The isotropic correction by Freysoldt *et al.* uses a planar average of the electrostatic short range potential while the anisotropic correction by Kumagai and Oba takes averages of this same potential at each atomic site outside a given radius from the defect. Both approaches are available in the PyCDT code, with the isotropic correction by Freysoldt *et al.* being the default. The planar averaging method can become problematic when large relaxation occurs, as the atomic sites contribute heavily to the change in electrostatic potential. The atomic site averaging method can become problematic if a small cell size results in a small number of atoms being sampled, causing statistical sampling errors. While, in principle, these alignment corrections should be equivalent, tests that we conducted revealed non-negligible discrepancies. However, the potential-alignment term often tends to be small ($\sim$0.1 eV), and, therefore, to not change overall trends in defect formation energies.

The correction methods used for point defects in semiconductors and insulators have been an intensely debated topic in the past decade [8]. One issue upon which there is common agreement is that large defect-defect interactions change the energetics of the system so that the computed defect formation energies are no longer relevant for physical quantities like defect concentrations or thermodynamic transition levels. These unwanted defect-defect interactions frequently lead to delocalization of the defect charges, the instance of which has to be ascertained manually. Several methods that address delocalization can be found in the literature [8, 26, 53].

If we assume that the defect charge can indeed be localized within the level of DFT used, then best practice demands to balance computational expediency (supercell size) with sufficient localization of the charge around a defect as indicated by the outputs of the charge correction method chosen. In the original derivation of the isotropic correction by Freysoldt *et al.*, the middle "plateau" region of the electrostatic potential yields information about the separation of long range and short range effects. A flat plateau indicates that the Coulomb potential has been removed from the total potential generated by DFT, and short range effects have not delocalized throughout the entire supercell. As a result, Freysoldt *et al.* [65] suggested that the flatness of the resultant "plateau" yields a qualitative metric for the success of the calculation. When running the isotropic correction by Freysoldt *et al.* in PyCDT, the planar averaged electrostatic potential is analyzed for variations larger than 0.2 eV—a number that stems from experience, and can be altered in the code if the user prefers to. If this criterion is not met, the code raises a warning. In such a case, the user should consider the possibility of delocalization.

For users who desire additional corrections related to improving corrections with semilocal functional approaches, the development branch of PyCDT also includes the ability to include band edge level alignment with respect to the average electrostatic potential, shallow level corrections based on the values for band edge alignment, and Moss-Burnstein band filling corrections [53]. Parts of these corrections require some subjective judgment calls to be made by the user, so they are not included in the automation procedure by default.

2.3.5 Charge Ranges

Charge ranges, $[q_{\text{min}}, q_{\text{max}}]$, have to be estimated beforehand for a given defect X, and for this purpose ionic models typically form the basis of such predictions [28]. Known oxidation states of the element(s) involved in X can then be used to define the charge states to be considered. However, common ionic models do not always predict the most stable defect. Tahini *et al.* have, in this context, shown that combining gallium or aluminum with group-V elements can yield negatively charged anion vacancies, whereas an ionic model predicts a +3 charge state [73]. In PyCDT, we implemented different procedures to determine the range of defect charges for semiconductors and insulators. Users can choose between either of these two options and a custom range of defect charges for each defect, as described in Section 2.4.1.

To address the issue of uncommon charge states found in semiconductors, we developed a data-driven approach that combines elemental oxidation states with results from literature for determining the optimal charge assignment process. We compiled a list of stable charge states (Table A.1 in the Appendix) from previous studies for various defects in zinc blende and diamond-like semiconductor structures [28, 59, 73, 88–93]. Procedures adhering more or less strictly to ionic models resulted in too few charge states when compared with the literature. The most effective approach that we found employs a bond-valence estimation scheme [76, 94] to obtain formal charges of elements in the bulk structure, as well as minima and maxima of common oxidation states of bulk and defect elements. The formal charges and common oxidation-state ranges are subsequently used in a defect type-dependent assignment procedure:

1. *Vacancies*: Use the formal charge of the species originally located on the vacant site, oxi, to define the charge range: $[-oxi, +oxi]$. For GaAs, this procedure results in defect charges ranging from -3 to 3 for both $\mathrm{V_{Ga}}$ and $\mathrm{V_{As}}$.

2. *Anti-sites*: Use the minimum and the maximum from combining all oxidation states of *all* elements in the bulk structure, $oxis_{\mathrm{bulk}}$, to define the relevant charge range: $[\min(oxis_{\mathrm{bulk}}), \max(oxis_{\mathrm{bulk}})]$. Data mining determined that the upper range limit can, in fact, be decreased by 2: $[\min(oxis_{\mathrm{bulk}}), \max(oxis_{\mathrm{bulk}}) - 2]$. With this procedure, the antisites in GaAs are assigned charge values from -3 to +3.

3. *Substitutions*: Determine the oxidation states of the foreign (or, extrinsic) species, $oxis_{\mathrm{ex}}$. Then subtract the formal charge of the site species to be replaced from this list. Use the minimum and maximum of this set to produce $[\min(oxis_{\mathrm{sub}}), \max(oxis_{\mathrm{sub}})]$. Data mining determined that, if the new range has more than 3 charge states and has an upper bound larger than 2, one can cap the range by 3 to prevent excessively high charge states. For example, when GaAs is doped with Si, $\mathrm{Si_{Ga}}$ generates charges in the range of [-7,1], and $\mathrm{Si_{As}}$ generates charges in the range of [-1,4].

4. *Interstitials*: Use the minimum and maximum of all oxidation states of the interstitial species:
   $[\min(oxis_{\mathrm{int}}), \max(oxis_{\mathrm{int}})]$. If 0 is not included, data mining suggests that we extend the range to 0 accordingly. For As interstitials in GaAs, the resulting defect charges are in the range [-3, 5].

The algorithm successfully includes all charge states from our benchmark list in Table A.1 by yielding, on an average, 6.4 states per defect. The average number of states produced too much per defect in comparison to literature (excess charge states) are 1.1 is 1.9 at the lower (more negative) and at the upper (more positive) charge bound, respectively. This is desirable because including more charge states on either side ensures no extra states become stabilized when varying the Fermi level within the band gap. Hence, the effective relative excess in charge states is 20% and, thus, acceptable.

For insulators, the number of defect charge states is typically less than for the above discussed semiconductors. For example, the charge states in MgO range from -2 to 0 and 0 to $+2$ for cation and anion vacancies, respectively [95]. Any other charge state is not considered because of the high ionization energy required to form Mg^{3+} and the high electron affinity of O^{2-} to form O^{3-}. Hence, the oxidation states of cations and anions are limited to $[0, y]$ and $[-x, 0]$ for a binary A_xB_y insulator, where A is a cation and B is an anion.

2.3.6 Interstitials

PyCDT uses an effective and easily extendable approach for interstitial site finding (Interstitial Finding Tool: InFiT) that has been recently introduced by Zimmermann *et al.* [67]. The procedure systematically searches for tentative interstitial sites by employing coordination pattern-recognition capabilities [96, 97] implemented in pymatgen [76]. In Algorithm 1 (Figure 2.3), we provide a simplified pseudo-code representation of the approach. The detected interstitial sites exhibit coordination patterns that resemble basic structural motifs (e.g., tetrahedral and octahedral environments). Such interstitial sites are particularly important because several [98–107] β^- emission channeling measurements [108, 109] have identified them as the most prevalent types of isolated defects after substitutions for impurities implanted into similar materials as we consider here (zinc blende/wurtzite-like and diamond-like structures). Bond-center interstitials in a so-called split-vacancy configuration are also observed frequently. However, these are defect complexes—not isolated defects—and, thus, beyond the scope of the present PyCDT implementation. The interstitial search approach should also be suitable for intercalation and ion diffusion applications because related design rules typically rely on detection of tetrahedral, octahedral, bcc-, and fcc-like environments [110, 111].

2.3.7 Default DFT Calculation Details

PyCDT includes mechanisms to input user-defined settings for all DFT calculations. If no user settings are specified, then the following initial settings are specified for the calculation. The ions in the defective supercells are geometrically relaxed at constant volume until the force on each ion is less than 0.01 eV Å. At each geometric step, the energy of the supercell is converged to 10^{-6} eV. By default, spin polarization is turned on, and crystal symmetry is ignored to account for any symmetry breaking relaxations such as Jahn-Teller distortions. Electronic states are populated using a Gaussian smearing method [112] with a width of 0.05 eV. While no geometric relaxation is performed for the non-defective bulk supercell, a calculation that is necessary for the charge correction, the electronic degrees of

Algorithm 1 Interstitial Site Searching

```
GetNeighbors(struct, inter_trial_site, dmin, delta)   ▷ Get a list of neighbors of site inter_trial_site in struct that are within a sphere of $(1 + delta)$ dmin.
GetCoordinationDescriptor(point, neighs, coord_type)  ▷ Calculate the value of the descriptor for the target coordination environment coord_type of an atom at point with neighbors neighs.

procedure GetCoordinationPatternInterstitials(struct, inter_elem, all_coord_types= [tet, oct], thresh = [0.3, 0.5], dl = 0.2, dstart = 0.1, ddelta = 0.1, dend = 0.7)
    Let inter_sites be a new empty list
    Let coord_descr be a new empty list
    for point on a regularly mashed grid in struct with resolution dl do
        Let dmin be the distance from point to the closest crystal atom
        if $dmin > 1$ Å then
            Let inter_trial_site be a new Site object of type inter_elem located at point
            Let struct_plus_inter be a new Structure object ← struct appended by inter_trial_site
            for delta starting from dstart in ddelta steps to dend do
                Let neighs be a new list ← GetNeighbors(struct_plus_inter, inter_trial_site, dmin, delta)
                for coord_type having index icoord in all_coord_types do
                    Let this_coord_descr be a float number ← GetCoordinationDescriptor(point, neighs, coord_type)
                    if $this\_coord\_descr > thresh[icoord]$ then
                        Add entry to inter_sites list ← inter_trial_site
                        Add entry to coord_descr list ← this_coord_descr
                        break
    Let labels be a list of coord_type-specific cluster labels for each entry in inter_sites which are found with a distance threshold of 1.01 dl.
    Let include be a new empty list.
    for unique_label in labels do
        Find site with index imax in inter_sites that has highest coord_descr among site with this unique_label.
        Add entry to include ← imax
    final_inter_sites ← Prune the inter_sites in include further to include symmetrically distinct sites only
    return final_inter_sites
```

Figure 2.3: Algorithm for Interstitial Site Searching

freedom are optimized with the same settings applied to the defect-supercell calculations. A $2 \times 2 \times 2$ Monkhorst-Pack k-point mesh is used for the defect calculations. For any other parameters, we adopt the standard MP settings [76]. Finally, we emphasize that PyCDT also includes mechanisms to input user-defined settings for DFT calculations which can be used for extending calculations beyond the exchange and correlation approximation of GGA. The practical implementation of user-defined settings is described at length in Appendix B.

2.4 PyCDT Usage and Examples

PyCDT was developed in a way that reflects different analysis stages (Figure 2.4): setup of DFT calculations, parsing of finished jobs, computation of a correction term, and plotting of formation energies. This allows reuse and integration of parts of the code in other packages. Our package has a dependency on pymatgen [76], matplotlib [113] and numpy [114], and it was developed and tested for Linux and Mac OS X. However, we also expect it to work on Windows (with cygwin).

It is possible to designate three levels of involvement which an end user may desire from the PyCDT code. Ranked in increasing order of involvement required these are: (Level

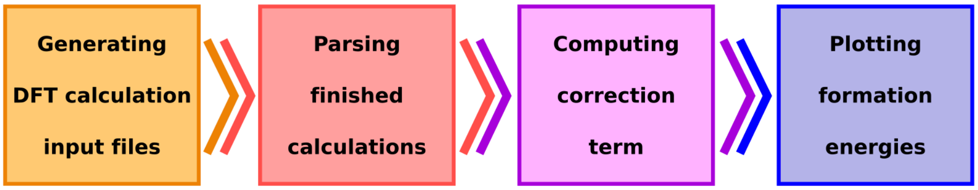

Figure 2.4: Steps in the computation of charged-defect formation energies with PyCDT.

1) standard command-line user interface calls, (Level 2) isolated python scripts mimicking command-line calls but for more personalized user involvement, and (Level 3) user customized workflows for performing personalized high-throughput defect calculations. In the subsections that follow, we illustrate these three levels of user involvement in the example of zinc-blende GaAs with VASP [68, 69] as the backend DFT code. In order to be involved at (Level 2) and (Level 3) it is neccessary to first understand the manner in which the PyCDT command line tool makes use of the PyCDT core functionality. Accordingly, in sections 2.4.1-2.4.4 we describe how the command line approach to PyCDT (Level 1) can be used for each step of the general charged-defect calculation workflow outlined in Figure 2.4.

For users interested in further customized applications of PyCDT (Levels 2 and 3), Appendix B includes a description of the code's structure and the manner in which the command line code makes use of the core functionality of PyCDT. This helps to reiterate that the core classes within PyCDT are entirely general and can be used for any desired applications that involves setting up, computing charge corrections for, and/or parsing defect calculations. As a brief example of user customization beyond the command line tool, Appendix B also demonstrates customizable approaches to (a) initializing and parsing a personalized phase diagram for chemical potentials and (b) screening over non-intuitive charge states of defects in a computationally efficient manner. As a demonstration of the brute power of these tools, Subsection 2.4.5 displays a test set of high-throughput computation of defects (Level 3) by performing intrinsic defect calculations on 15 additional zinc blende systems beyond GaAs and 5 oxide systems.

2.4.1 Setup of DFT Defect Calculations

The starting point for setting up charged defect calculations is the crystal structure. The user can provide the bulk structure in one of two ways:

1. by the name of a structure file of conventional format (e.g., cif, cssr), or code specific formats such as POSCAR that are recognized by pymatgen, or
2. via a Materials Project identifier (MPID).

Crystal structures from MP [64] are obtained through the Materials Application Programming Interface (MAPI) [76]. In the MP database, each structure is assigned a unique identifier. These MPIDs have the format *mp-XXX* in which *mp-* is prefixed to a positive integer *XXX*. In the following, we use GaAs (*mp-2534*), which has the zinc-blende structure, as an example for performing all different stages of charged defect-property calculations with PyCDT.

We first generate the defect supercells and the bulk supercell using pymatgen's defect structure generator and the defect structure classes in the core of PyCDT. The two steps for generating the input files are combined into a single command:

```
▷ pycdt generate_input   (   --structure_file   ⟨structure file⟩   |   --mpid ⟨mpid⟩   )
                         [   --mapi_key         ⟨mapi_key⟩                          ]
                         [   --nmax             ⟨max_no_atoms_in_supercell⟩         ]
```

With *--nmax*, the user defines the maximal number of atoms in the defect supercell. If the parameter is not given, a default value of 128 is used, which was shown to result in well converged defect formation energies after finite size corrections were included in systems with dielectric constants greater than 5.0 [59, 86]. The mapi_key is required if querying the MP database, and is found on the Dashboard after logging into the MP website.

The input file-generation command creates a folder, representing the reduced chemical formula of the crystal structure (e.g., *GaAs*). It contains several subfolders, whose names are indicative of the calculations to be performed:

- *bulk*: calculation of pristine crystal structure,
- *dielectric*: calculation of macroscopic static dielectric tensor (ion clamped high frequency, ϵ_{∞}, plus the ionic contribution, ϵ_{ion}) from DFT perturbation theory, (used by the charged defect correction)
- *deftype_n_info*: calculation of the n-th symmetrically distinct defect of type *deftype* (vacancies: *vac*; antisites: *as*; substitutions: *sub*; interstitials: *inter*) with properties *info*.

By default, the above command generates vacancy and antisite defects only. Hence, there are four defect folders for GaAs, which has two sublattices, corresponding to one antisite and one vacancy defect on each sublattice. Table 2.1 summarizes the default defect types and resulting folder names for GaAs.

Table 2.1: Default defects set up for GaAs with PyCDT

Defect Type	Folder Name
Vac_{Ga}	GaAs/vac_1_Ga
Vac_{As}	GaAs/vac_2_As
Ga_{As}	GaAs/as_1_Ga_on_As
As_{Ga}	GaAs/as_2_As_on_Ga

Substitutional and interstitial defects have to be invoked explicitly with the keyword *--sub host_species substitution_species*. Multiple substitutional defects can be generated by repeating the *--sub* keyword with the desired host species and the corresponding substituting species. The substitution folders are labeled in the same manner as the antisites, only changing *as* to *sub*.

The setup of coordination-pattern resembling interstitials is invoked by the *--include_interstitials* command-line option. PyCDT produces intrinsic interstitials as per default only. Extrinsic interstitials can be achieved by providing a list of elements as positional arguments (e.g., *--include_interstitials Mn*). To obtain both intrinsic and extrinsic interstitials the intrinsic elements have to be explicitly mentioned (e.g., *--include_interstitials Ga As Mn*). As for the other defect types, PyCDT enumerates the interstitial calculation folders according to symmetrically distinct sites found. The *info* part of the interstitial folder names indicate (1) the type of the atom located on an interstitial site having a certain (2) coordination pattern and (3) chemical environment. For example, *inter_1_As_oct_Ga6* shows that we are dealing with an As interstitial that is octahedrally coordinated by six Ga atoms.

For each defect type in semiconductors, multiple charge states are considered according to the algorithm outlined in Sec. 2.3.5. For insulators a conservative charge assignment is used as described in Sec. 2.3.5. By default, the input structure is considered a semiconductor. To specify the input structure is of insulator type, the option *--type insulator* can be used. The user can also modify the charge assignments for each defect by specifying either of the two flags, *--oxi_state* or *--oxi_range*. Alternatively, the option *--type manual* allows for the user to specify every charge state that is desired. The DFT input files associated with each of these charge states, q, are deposited into subfolders named *charge_q*. For example, seven charge states are generated for the gallium vacancy in GaAs.

Apart from the structure file, PyCDT automatically generates all other input files according to the settings used for the MP. The input settings can also be easily modified by supplying the parameters in a yaml or json file and using the keyword *--input_settings_file* ⟨*settings_file.yaml*⟩. For instance, the file *user_settings.yaml* that we provide in the *examples* folder changes the default functional from PBE to PBEsol and increases the energy cutoff to 620 eV. The structure of this file is described in further detail in the supplementary information. When such changes are made, the user has to keep in mind that the atomic chemical potentials obtained from the MP database in the final parsing step have to be replaced by user computed ones with the corresponding changes included during chemical potential calculations - a process which can be sped up substantially with PyCDT's phase diagram set up and parsing feature. Any DFT settings that are specific to either the bulk, or the dielectric, or the defect calculations can be thus realized, too, as demonstrated in the example file. The input settings whether chosen by default or by the user are expected to be tested for appropriate convergence criteria. In addition to the input files for DFT calculations, PyCDT saves a *transformation.json* in each calculation folder, except for *dielectric*, to facilitate post-processing.

2.4.2 Parsing Finished Calculations

The DFT calculations can be run either manually, with bash scripts, or with high throughput frameworks [115]. Once all the calculations have successfully completed, the generated output files are parsed to obtain all the data needed to compute defect formation energies, E^{f}. This part of PyCDT is executed by reading the *transformation.json* file that was output from the previous file generation step. To initiate parsing from the command line interface, the user issues:

```
▷pycdt parse_output  [  --directory   ⟨directory⟩  ]
                     [  --mpid        ⟨mpid⟩       ]
                     [  --mapi_key    ⟨mapi_key⟩   ]
```

Here, directory is the root folder of the calculations. If executed within the folder of the calculations the option can be omitted. Once the parsing is completed, PyCDT stores all the data required for next steps in a file called "defect_data.json". If any of the calculations were not successfully converged according to the code output files, PyCDT raises a warning, but continues parsing the rest of the calculations. The output file "defect_data.json" contains the parsed energies of the defect and bulk supercells as well as other information required in the next steps to calculate finite size charge corrections and defect formation energies. Some of the additional data such as the dielectric constant is obtained by parsing the output from the dielectric calculation. The band gap and atomic chemical potentials generated in this step are obtained from computed entries in the MP database. Note that these band gaps are only accurate at the level of GGA, which often underestimates the gap by about 50%. The output file "defect_data.json" is highly readable and users can edit the file to supplant parameters either parsed from the DFT calculations or obtained from the MP database. If the user prefers to have formation energies and transition levels closer to a higher level of theory (which can provide better band gaps than the GGA approximation), the band edge alignment procedures suggested in Section 2.3.4 can be used. Furthermore note that some structures in the MP database do not have fully computed band structures, which results in poorly converged band-gap characteristics.

2.4.3 Computation of Correction Term

Correcting the errors due to long-range Coulomb interactions in finite-size supercells results in improved defect formation energies. A feature of PyCDT is the possibility to compute such corrections with minimal work from the end user. The following command-line call computes individual correction values for all charged defects found in the present directory:

Here, correction method keywords can be either *freysoldt* for correction due to Freysoldt *et al.* [65, 84] or *kumagai* for the approach extended to anisotropic systems by Kumagai and Oba [66]. As shown in Section 2.5.1, these codes have been rigorously tested against the results from the codes of the original authors. The command line interface requires the

```
▷pycdt compute_corrections   [   --correction_method   ⟨correction method⟩   ]
                             [   --epsilon             ⟨epsilon tensor⟩      ]
                             [   --input_file_name     ⟨defect data file⟩    ]
                             [   --plot_results        ]
```

defect data file generated in the previous step, *defect_data.json*, for computing the corrections. This flag can be omitted if the file name is unchanged. The calculated corrections for each defect charge state are stored in a file called *corrections.json*. By rerunning the command with different correction keywords, one can quickly obtain the corrections computed with different frameworks. Shown in Figure 2.8 are the resulting potential alignment plots for each correction type on the Ga_{As}^{-2} defect in GaAs.

The sampling regions for obtaining the potential alignment correction defaults to 1 Å in the middle region of the planar average plots recommended by Freysoldt *et al.* [84], and to the region outside of the Wigner-Seitz radius for atomic site averaging method, following the approach described in Ref. [66]. The width of these default sampling regions can be changed by modifying the instantiation of the relevant PyCDT correction classes.

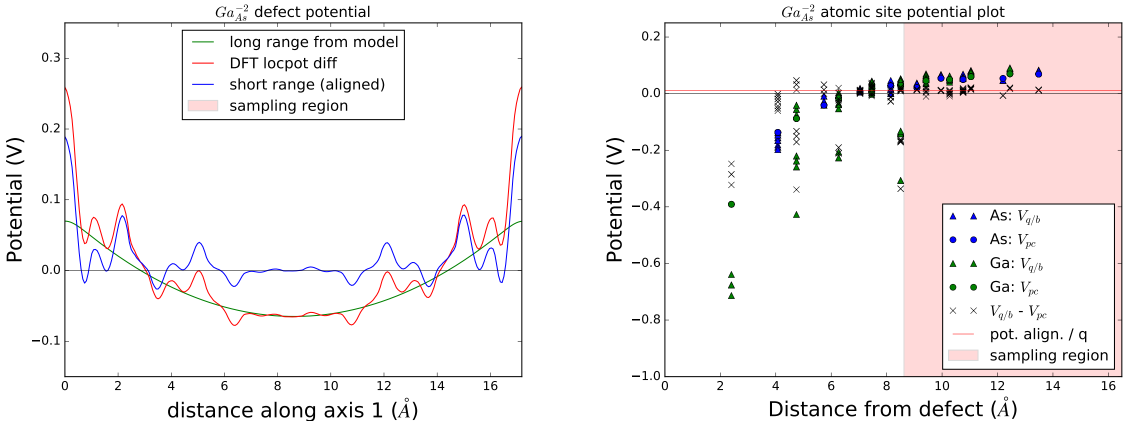

Figure 2.8: Two different methods for computing the potential alignment correction on GaAs calculation. At left is isotropic correction, developed by Freysoldt *et al.*, using the planar average method [65, 84], and at right is anisotropic correction by Kumagai and Oba, using the atomic site averaging method. [66].

2.4.4 Formation Energy Plots and Transition Levels

Once the defect energetics and the correction values are obtained and specified in the *defect_data.json* and *corrections.json* files, the transitition levels and formation energies of

```
▷pycdt compute_formation_energies   [   --input_file_name         ⟨defectsdata json file⟩   ]
                                    [   --corrections_file_name   ⟨corrections json file⟩   ]
                                    [   --bandgap                 ⟨band gap⟩                ]
                                    [   --plot_results            ]
```

each defect across the band gap can be determined by: By default, PyCDT uses the band gap stored in the MP database, which is computed with GGA-PBE and, hence, under-predicted when compared to the experimental band gap. As mentioned several times in this work, this approximation can be improved upon with the optional corrections included, such as the band edge realignment feature of PyCDT. A simpler approximation to improving the defect formation energies is to plot the defect formation energies across the experimental gap the user can specify the experimental band gap. This can be done from the command line with the keyword *–bandgap ⟨band gap⟩*. This has the effect of extending the gap by shifting the conduction band minimum, but keeping the position of the valence band maximum and the defect levels fixed, and it is often called the "extended gap" scheme. We note that the extended gap option is strictly for plotting purposes and, thus, does not alter the defect formation energies nor the transition levels. If the names of the files obtained in the previous two steps are not changed, the corresponding options can be omitted. If the *corrections.json* file is not found and an alternative corrections file is not specified, PyCDT assumes that electrostatic corrections are not desired and computes the defect formation energies without any corrections. As detailed in Section 2.3.3, the defect formation energies are influenced by the chemical environment, and their range is determined by the phase stability of the various compounds formed by the constituent host and defect elements. Hence, two plots are generated corresponding to the chemical availability of the constituent host elements in the compound. The files "Ga_rich_formation_energy.eps" and "As_rich_formation_energy.eps" are shown in Figure 2.10. These results are verified to be consistent with literature results in Section 2.5.2.

2.4.5 Example Usage for High-throughput point defect calculations

To demonstrate the capabilities of PyCDT in a high-throughput environment, we have computed the defect formation energetics of 15 additional zinc blende systems and 5 oxide systems. The results for these calculations are shown in Figure 2.11.

The calculations were performed using the core functionality of PyCDT which has been outlined in Sections 2.4.1- 2.4.4 and described at length in Appendix B. For running the DFT calculations, the Fireworks software [115] was used to set up atomic workflow tasks from a structure which had random local symmetry breaking performed (a task which is trivially performed with the Pymatgen software [76]). To expedite the handling of many

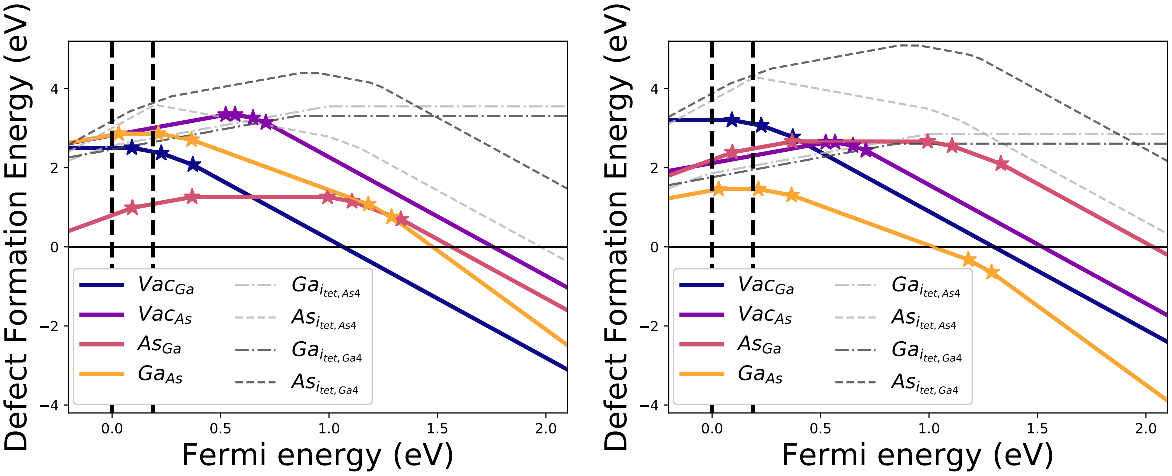

Figure 2.10: Defect formation-energy plots from PyCDT for GaAs. The left panel is obtained in the As-rich growth regime, whereas the right panel is obtained under Ga-rich conditions. Interstitial defects are colored according to their site within the lattice, with dashed lines given to As interstitials and dash-dot lines given to Ga interstitials. The thick vertical dashed black line indicates the GGA-PBE band gap of GaAs [64].

common DFT failures encountered (e.g. problems with electronic self-consistency etc.), the Custodian software [76] was implemented to correct for standard job failures. The core DefectsAnalyzer class, described further in Appendix B, was then implemented in a manner similar to the charge screening procedure defined in Appendix B, to ensure additional charge states were not stabilized within the gap. Parsing and accumulating all relevant quantities for formation energetic analysis into a database was simple to implement with the use of the DefectsAnalyzer class.

Out of a total 376 calculations that were run for this analysis, 56 jobs failed to finish on the first run - either due to walltime errors or additional electronic convergence issues. Fireworks database management coupled with PyCDT core analysis of the additional charge states allowed for quick identification of jobs with errors that required follow up calculations. This approach allowed for fast re-submissions which took on the order of minutes, rather than multiple hours/full days of analysis of failed defect jobs. This demonstrates the massive scalability of calculations which PyCDT can provide for a researcher who desires to intelligentlly implement defect calcualtions in a high-throughput environment.

2.5 Validation and Verification

2.5.1 Validation

To validate PyCDT's implementation of each correction method, we ran the correction methods on the defects generated and computed for the 15 zinc blende structures (binary and elemental), comparing the charge corrections generated by PyCDT with the open-source code developed by Freysoldt *et al.*, SXDEFECTALIGN, as well as with the command line code developed by Kumagai and Oba. Over a total of 224 (non-zero charge) defects calculated, the root mean square difference between PyCDT and the original author's codes were 16.5 meV and 19.4 meV for the correction by Freysoldt *et al.* and the correction by Kumagai and Oba, respectively. The differences in the corrections are almost entirely attributed to the resolution in the calculation of the potential correction.

2.5.2 Verification

To verify the results predicted from the example GaAs test set, we compared the defect formation energies in GaAs obtained from PyCDT with the data reported in literature. We note that all of the transition levels for the Vac_{Ga} and As_{Ga} defects are within the range of transition levels that we found for semi-local functional approximations in the literature. An exception is the As_{Ga}(-1/-2) transition, which appears very far into the GGA-PBE conduction band. This outlier is off by 0.273 eV relative to the reported results by Chroneos *et al* [89]. For all transition levels that we predicted, we find a root mean square deviation of 0.218 eV from the window of values found in the literature [73,89,116–121]. This is a modest variation that reflects the difficulty in predicting defect levels consistently—even within the same level of theory.

In a similar manner, we use References [73] and [89] to verify 63 additional transition levels in 5 systems within the high-throughput test set of Section 2.4.5 (AlP, AlAs, AlSb, GaP, GaSb). We find a root mean square absolute error of 0.29 eV from the transition levels reported in these two references, with a maximum error of 0.89 eV for the Aluminum vacancy (-2/-3) transition level in AlP. Again, this deviation is consistent with the variation of predicted transition levels from DFT and suggests a need for standardizing approaches to computing defect formation energetics.

2.6 Summary

We have introduced PyCDT, a Python toolkit which facilitates the setup and post-processing of point defect calculations of semiconductor and insulator materials with widely available DFT suites. This open source code allows for coupling automated defect calculations to the massive amount of data generated by the Materials Project database. Apart from the underlying theory, approaches, and algorithms, this paper presents a detailed guide for how to use PyCDT at every step of the computation of charged defect properties employing the well-studied example of GaAs. While the example results were obtained from VASP [68,69] calculations, we carefully developed PyCDT in an abstracted form that adopts the advantageous code agnosticism of pymatgen [76]. This makes the provided tools attractive to any user interested in running defect calculations, regardless of DFT code preference. However, we emphasize that, despite its convenience and our effort to construct sensible defaults, the computation of defect properties with PyCDT still requires user expertise for choosing appropriate settings in certain circumstances and for interpreting the results meaningfully in general (i.e., we discourage purely "black box" usage).

The PyCDT version presented here is 1.0.0. Future updates will, amongst others, include adaptations related to improved charge delocalization analysis, further defect corrections for issues like artificial band dispersion, as well as the possibility of generating defect complexes. On the application side, PyCDT could also be extended to compute configuration coordinate diagrams, so as to evaluate optical and luminescence transitions associated with the point defects in materials targeting optical applications.

We hope that our openly available tools will help to standardize computational research in the realm of charged defects. In particular, we hope that reproducibility issues commonly encountered in DFT calculations [122] can be more effectively identified and tackled.

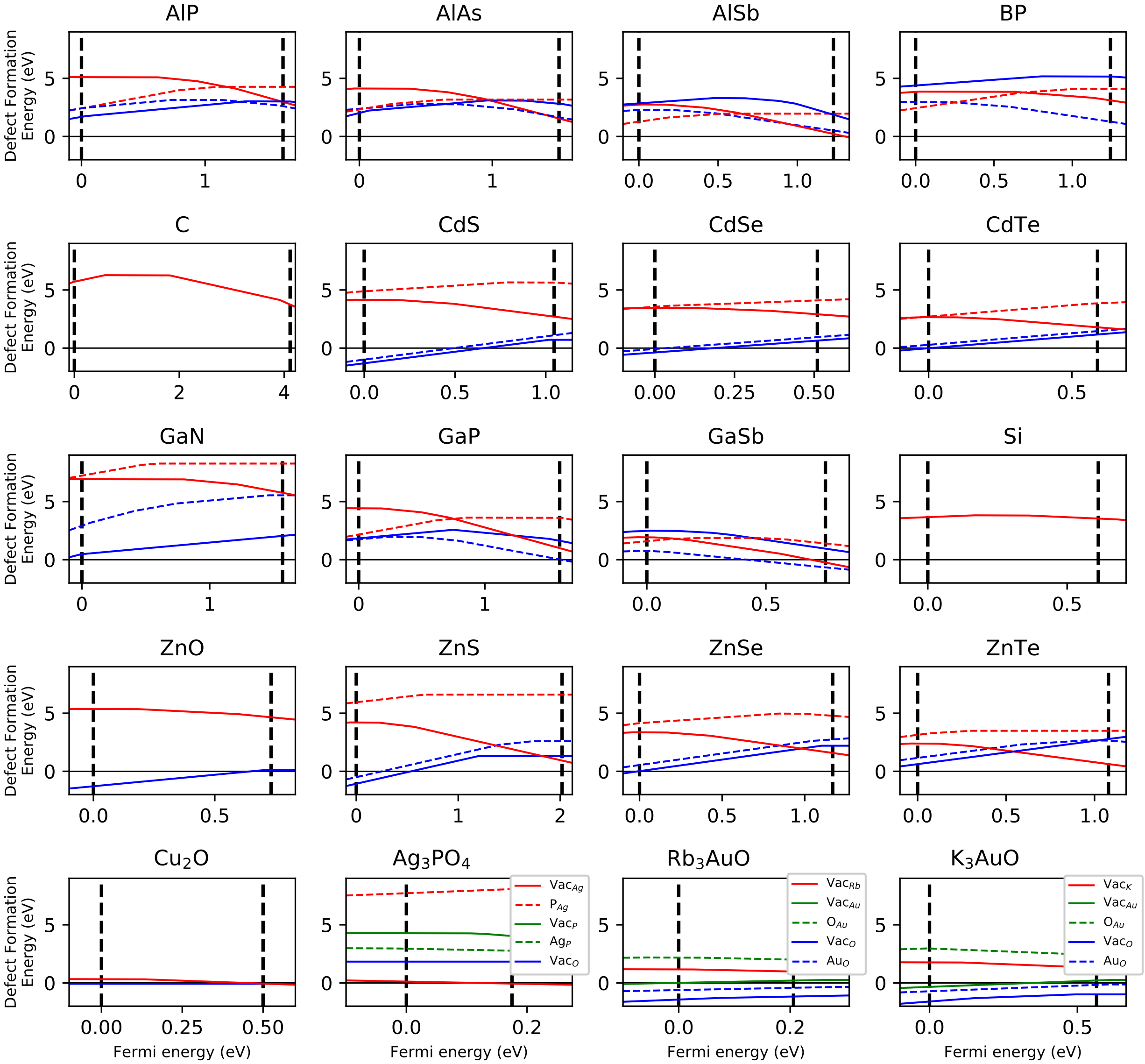

Figure 2.11: Defect formation energy plots for 15 zinc blende systems and 5 oxide systems. The spacegroups and materials project identification numbers for each of these structures is included in Table C.1 of the Appendix. Solid red lines indicate cation vacancies, while dashed red lines are cation antisites (Anion_on_Cation site defects). Solid blue lines are anion vacancies, while dashed blues lines are anion antisites (Cation_on_Anion site defects). For the four ternary oxide systems, green lines are also used to indicate defects on the secondary cation site. Legends are included as insets for ternary sytems. The cation-rich growth condition dictates all of the atomic chemical potentials as described in Section 2.3.3. Due to zero gap predictions at the GGA level of DFT, the experimental gap was used for GaSb.

CHAPTER 3

Example Applications of Defect Calculations for Energy Materials

3.1 Forward

The work presented in this chapter is an accumulation of un-published and published work making use of the PyCDT code for computing point defects. Section 3.3 presents unpublished work performed by D. Broberg in between Fall 2013 - Spring 2014. Section 3.4 presents work published by P. Canepa, G. S. Gautam, D. Broberg, S-H. Bo, and G. Ceder in Chem. Mater. Volume 29, Issue 22, pages 9657 - 9667 (2017), and is partially reproduced here with the permission of all co-authors. Section 3.5 presents unpublished work performed by D. Broberg in between Fall 2016 - Summer 2018.

3.2 Introduction

Point defects in energy materials impart critical macroscopic properties which can either benefit or hinder material performance. The impact of a defect can be direct, as is the case for deep traps in optoelectronic materials, or indirect, as is the collective aggregation of defect types leading to a particular Fermi-level pinning position [5,6,8,25]. While general defect-engineering approaches involve the modification of particular macroscopic properties, it is important to remember that point defects are unavoidable (can only be replaced by other defects as a result of configurational entropy) and are not universally characterizable by experiment. Consequently, first principles computation of point defects have served as a useful means for understanding defect formation, as well as understanding the thermodynamic requirements for defect engineering in energy materials [8].

This chapter underscores the importance of DFT point defect calculations by applying the automation capabilities described in Chapter 2 to three different energy application areas. In Section 3.3 we describe work done on Thermoelectric materials, including an investigation into theoretical requirements for a new, promising layered material - SnSe. In Section 3.4

we present work on Mg-spinel materials which show promise for solid-electrolyte battery applications. Then in Section 3.5 we consider two different materials for use in photovoltaic applications. Section 3.5.1 covers the tendency for Fermi level pinning across a spectrum of chemical and structural permutations within inorganic halide perovskite solar cell materials, while Section 3.5.2 demonstrates a small-scale benchmark of experimental measurements performed on thin-film CdTe against the results produced from DFT calculations.

3.3 Thermoelectrics

Thermoelectric materials have the ability to directly convert heat into electricity. To accomplish this, charge carriers are made to move by exploiting a temperature gradient with asymmetries in a material's electronic band structure [123]. The movement of charge carriers in this way is known as the Seebeck effect, and the primary metric for thermoelectric performance is the "figure of merit": $zT = S^2\sigma T/(\kappa_E + \kappa_L)$, where S is the Seebeck coefficient, σ is the electronic conductivity, T is the temperature, and κ_E (κ_L) is the electronic (lattice) thermal conductivity [123]. A typical figure of merit for a commercially available thermoelectric material lies in the range of 0.6 - 1.2 [123].

This class of devices offers a unique approach to waste heat recovery and energy efficiency improvements. For example, it has been proposed that modern thermoelectric devices could be placed on the tail pipe of an internal combustion engine car to power some of the electronic components of the car and improve the overall efficiency [124]. However, given the limited efficiency and maximum surface temperature requirements of thermoelectric devices like $BiTeO_3$, their application has been limited to small scale, low-power electronics. In addition, materials with higher figures of merit, like PbTe, remain too costly for large scale practical applications [124]. This has inspired the materials science community to search for new thermoelectric materials with high figures of merit.

One approach to improving the figure of merit is through "band engineering" wherein intrinsic characteristics of the band structure are used to screen for prospective new materials [125]. Approaches of this variety have been used within a number of computational high-throughput studies, searching for favorable material properties like high effective mass and Seebeck coefficient [32]. Using approaches like this, recent high-throughput theoretical studies have identified $TmAgTe_2$ and $YCuTe_2$, with their underlying structure classes, as new thermoelectric materials which subsequently produced promising zT values of 0.4 - 1 [40,126].

Another new and promising candidate for thermoelectric applications is the layered SnSe structure, which recently produced a record-setting figure of merit of 2.6 in a specific direction of the crystal lattice [127,128]. This has inspired many theoretical studies into the origin's of SnSe's favorable material properties for thermoelectric devices, including analyses of various aspects of the Boltzmann transport equation, as well as structural and electronic tendencies for SnSe's broader crystal class [129–131]. The SnSe structure, shown on the left side of

Figure 3.1, is a layered "rocking chair" orthorhombic phase with van der Waals bonding between layers stacked in the c-axis direction.

A major contribution to the low figure of merit in SnSe is the ultra-low thermal conductivity in the *a* and *b*-axis (in-plane) lattice directions [127]. This anisotropic signature appears further in the planar averaged electrostatic potential profile for the Sn_{Se}^{+3} defect calculation, as shown on the right side of Figure 3.1. The anisotropic directional requirement for a successful figure of merit limits the wide-spread applicability of using SnSe for thermoelectric materials in the near future, since single crystal manufacturing on a large scale can be costly. Regardless, by understanding the fundamental signatures that indicate favorable thermoelectric behavior in SnSe, theory can help to find additional materials with similar thermoelectric performance.

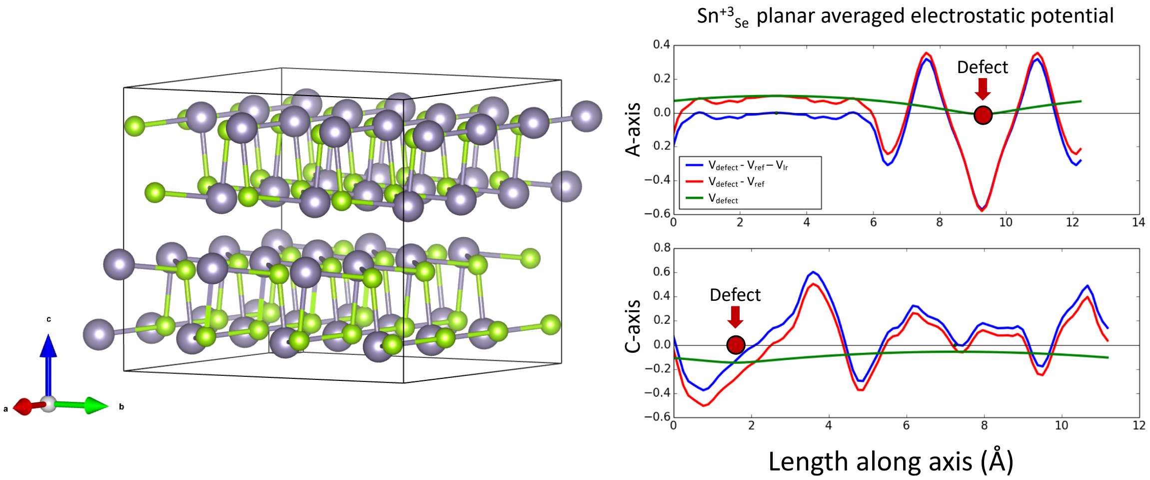

Figure 3.1: The anisotropic SnSe system. Shown at left: The SnSe structure, with gray Sn atoms, green Se atoms, and a layered c-axis direction. Shown at right: Planar averaged electrostatic potential for two different axes of the Sn_{Se}^{+3} defect calculation with lack of "plateau" far from defect cite in C-axis direction.

The layered nature of SnSe raises questions about adequate treatment of van der Waals forces within a calculation. Standard DFT fails in the implementation of accurate dispersion forces, as this requires adequate treatment of long range correlation effects [17]. To circumvent this, approximate corrections for the energetic contribution of van der Waals forces can be added to the Kohn-Sham DFT energy [132, 133]. Recent work by Björkman (2014) suggests that the recently produced VdW-CX van der Waals approach, created by Berland and Hyldgaard, works well for layered structures [134]. We consider the use of the VdW-CX functional on SnSe presently.

In Table 3.1, we show the relaxed lattice constants of SnSe, as compared to experiment, for several DFT energy functional implementations. All four functional implementations produced similar errors for the in-plane lattice constants with between 0.8-3% absolute relative error. All of the errors for LDA are negative, consistent with the well-known over-binding tendency of the LDA functional [17]. For the out of plane direction (c-axis), the VdW-CX functional approach minimizes error to 0.13%, suggesting excellent treatment of the out-of-plane forces for SnSe.

	a [Å] (% error).	b [Å] (% error).	c [Å] (% error)
Experiment (295 K)	4.153	4.445	11.501
LDA	4.120 (-0.79%)	4.315 (-2.92%)	11.308 (-1.69%)
GGA	4.219 (1.59%)	4.524 (1.78%)	11.790 (2.51%)
VdW-optB88	4.221 (1.64%)	4.496 (1.15%)	11.774 (2.37%)
VdW-CX	4.184 (0.87%)	4.344 (-2.27%)	11.516 (0.13%)

Table 3.1: Lattice constant comparison for different exchange and correlation functionals with SnSe. Experimental data is from Reference [135].

In Figure 3.2 we plot the formation energies of intrinsic defects in SnSe, performed with both the LDA and VdW-CX functional approaches, for Se-rich and Sn-rich growth conditions. All calculations were performed using the automation capabilities of the Python Charged Defect Toolkit (PyCDT) [136]. Due to the anisotropic charge localization tendencies shown on the right side of Figure 3.1, we make use of the anisotropic charge correction given by Kumagai *et al.* [66].

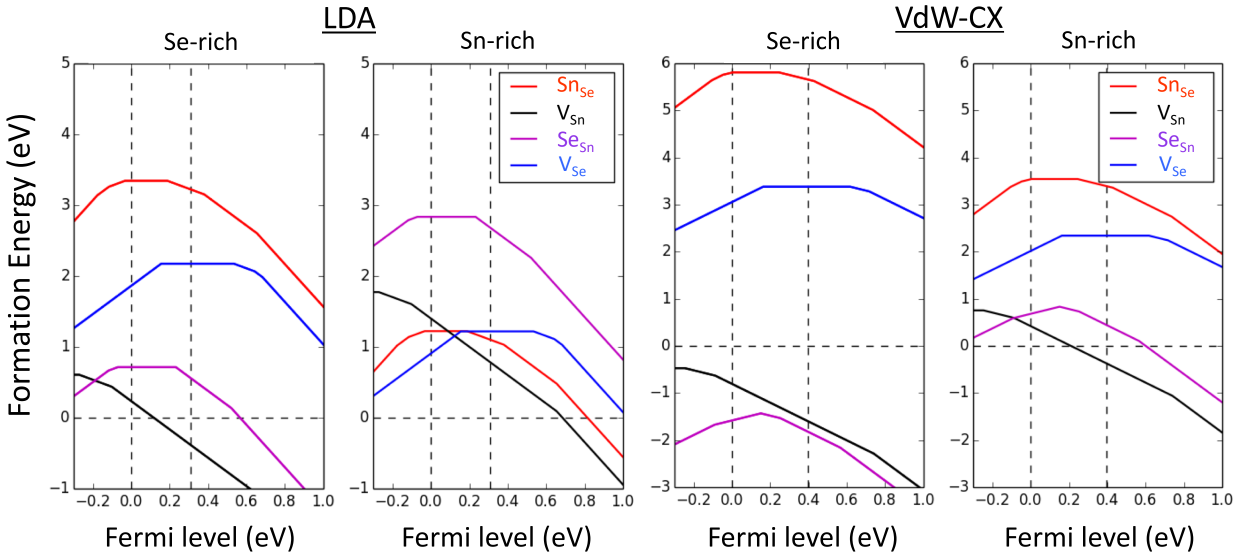

Figure 3.2: Defect formation energetics for the SnSe layered structure, computed with LDA and VdW-CX functionals, shown with Sn-rich and Se-rich growth conditions defining the chemical potentials. Band edge extrema for the given functional is shown with vertical dashed lines, with the VBM placed at zero.

We first consider the results of the LDA calculations, considering how they relate to the carrier concentrations produced for a practical thermoelectric figure of merit. In the Se-rich limit for LDA formation energies, negatively charged Sn vacancies push the Fermi level towards the valence band, creating p-type behavior with little competition from other defects. In the Sn-rich limit for LDA formation energies, Sn vacancies still dominate the upper half of the band gap, while Se vacancies become stabilized in the lower half. Antisite defects do not play a particularly important role in the free carriers of SnSe. Anion-vacancies act as "hole killers", as they act to ionically compensate the negatively charged cation vacancies. Since a larger carrier concentration improves the figure of merit, the LDA results of Figure 3.2 tell us that growing SnSe closer to Se-rich growth conditions would improve thermoelectric performance. The qualitative nature of these theoretical results have been confirmed by at least two other theoretical works published in the past two years [137, 138].

Shifting attention to the results of the VdW-CX functional, a large energetic stabilization of two defects (Sn vacancy and Se-on-Sn antisite) causes a strong deviation from the LDA results. The Se-rich limit produces negative formation energies across the entire gap and the Sn-rich limit has a very limited region of stability near the VBM. Negative formation energies indicate either an improper computational treatment of the atomic chemical potentials or an instability with regard to the formation of additional defects at a given Fermi energy. Given that the VdW-CX functional still predicts the structure to be stable within the Sn-Se phase diagram, the negative formation energies within the Se-rich results may suggest a destabilization of the structure with the removal of Sn-site defects computed by the VdW-CX functional.

To investigate this potential for structural destabilization further, in Figure 3.3 we consider cross sections of the charge density as computed with LDA (top) and VdW-CX (bottom). In particular, we draw attention to the lone-pair electron on each Sn atom, called out with blue boxes in each subfigure. The lone pair electron on the Sn atom has been documented to play a strong role in the stabilization of lower-symmetry phases within the Sn-chalcogenide structure class [139]. The lone pair electron on Sn atoms in Figure 3.3 is significantly more localized on the Sn-atom in the VdW-CX functional (bottom), relative to the LDA functional (top). A weakening of the steric Sn-Se repulsion leads to a weakened stabilization of the layered structure relative to other polymorphs of the SnSe structure class. This effect helps explain the destabilization with regard to the removal of Sn-site defects for the VdW-CX functional, as shown in Figure 3.3. The loss of additional Sn-atoms, which previously acted to stabilize the structure with lone pair steric interactions, leads to the triggering of long range relaxation that deviates from the original crystal symmetry. Such a result deviates from dilute limit behavior, and therefore the two formation energy diagrams shown at right in Figure 3.2 have computational artifacts that should be screened out. Avoiding long range relaxation of this variety serves as a useful lesson for future high-throughput studies.

Overall, the conclusions presented here for LDA are consistent with previously published work done with semi-local functionals on the defect physics of SnSe [137, 138]. We have also re-confirmed the importance of the lone-pair electron in stabilizing the layered polymorph

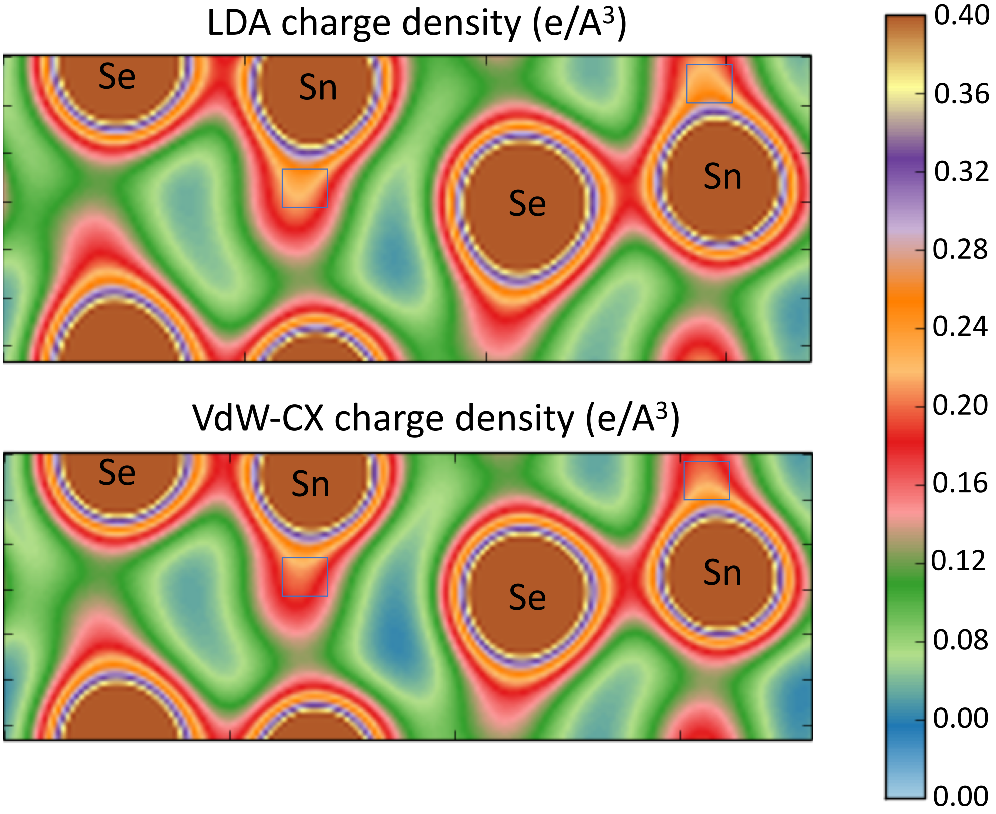

Figure 3.3: Charge density profile of SnSe for LDA (top) and VdW-CX (bottom) functionals, showing variation in the description of the lone-pair electron by the two functionals. Region of lone pair electron on Sn atom is called out with blue boxes.

of the SnSe structure class, as well as the importance of the choice of van der Waals forces with regard to bulk structural stability. While the influence of van der Waals forces on the defect physics of SnSe remains to be further investigated, the lessons learned about long range structural relaxation serve to motivate strict screening for structural destabilization in future high-throughput work.

3.4 Solid-state Batteries

Chalcogenide materials, based on sulfur, selenium and tellurium, are used in a range of technological applications, including thermoelectric materials [123, 140], semiconductors for light adsorbents and electronics [141–143], superconductors [144, 145], Li-ion battery materials [146, 147], quantum dots [148, 149], and more recently, topological insulators [150, 151]. The chalcogenide defect chemistry, either in terms of intrinsic point defects or extrinsic substitutional impurities, has often been deemed responsible for their respective figures of merit [152, 153].

Recently, ternary Mg-chalcogenide spinels were also identified as possible high mobility Mg-conductors [154]. This is relevant for the possible development of Mg transport coatings or solid state electrolytes for Mg batteries [154], which have the potential to outperform Li-ion batteries in terms of energy density [155]. Though significant Mg ionic conductivity is observed in $MgSc_2Se_4$, the electronic conductivity is $\sim$ 0.04% of the ionic conductivity [154], and substantially larger than in other state of the art alkali-(Li- and Na-)ion conductors [156]. Analogous to studies in semi-conductor applications [8], both intrinsic and extrinsic structural defects can cause large variations in electron (hole) conductivity in ionic conductors. Here we explore the defect chemistry of $MgSc_2Se_4$, $MgSc_2S_4$ and $MgIn_2S_4$ using first-principles calculations and aim to understand how structural defects modulate the electronic properties in the bulk spinels, identify the origin of the undesired electronic conductivity, and propose practical remedies. This section is an adaptation of the work published in Reference [157], modified to accommodate the content of this dissertation.

All defect calculations in this work were performed using the automation functionalities of PyCDT for setup, parsing, and the application of charge corrections [136]. In addition, core functionalities within PyCDT were used to self-consistently solve for the charge neutrality of the material, dictated by:

$$\sum_{X,q} qc[X^q] + n_h - n_e = 0 \tag{3.1}$$

n_h (n_e) is the hole (electron) concentration, obtained by integrating the density of states with respect to a given Fermi level, E_{Fermi}. $c[X^q]$ is the concentration of defect X^q, stemming from the Gibbs energy of defect formation, $G_f[X^q] \approx E_f[X^q]$, as $c[X^q] \approx \exp(-E_f[X^q]/k_BT)$. Since the formation energy also relies on the Fermi level position, a self consistent solution of Equation 3.1 yields a corresponding E^{eq}_{Fermi}, which sets the defect concentrations at thermodynamic equilibrium for a given temperature. Note that in all the materials considered in this work, we list a few defects as “dominant” owing to their low formation energies at E^{eq}_{Fermi}.

Materials that are normally synthesized at a high temperature ($\sim$ 1273 K, as in Ref. [154]) and rapidly cooled to room temperature, may have their high temperature intrinsic defect concentrations “frozen-in” (or quenched) at room temperature, while the free carrier concentration (n_h - n_e) changes with temperature, given the fixed defect concentration. A change in intrinsic defect concentration will require significant atomic diffusion, which is likely to be kinetically limited at low temperatures. Hence, for calculating defect concentrations and the Fermi level, we have considered two scenarios within the constraint of charge neutrality: (i) defect concentrations, equilibrium Fermi level (E^{eq}_{Fermi}) and free electron/hole concentrations ($\mathrm{c[e/h]}^{eq}$) are self-consistently calculated at 300 K corresponding to equilibrium conditions. (ii) defect concentrations are quenched from a higher synthesis temperature while the resulting Fermi level ($\mathrm{E}^{frozen}_{Fermi}$) and free carrier concentrations ($\mathrm{c[e/h]}^{frozen}$) are computed at 300 K. When quenched or frozen conditions are assumed, the defect concentrations are calculated self-consistently at higher quench temperatures (such as at 1273 K), and are not allowed to change when the Fermi level and the free-carrier concentrations are re-calculated at 300K. Since defect concentrations increase with increasing temperatures, the frozen approximation can quantify the possible deviations away from equilibrium in both defect and free carrier concentrations at 300 K.

3.4.1 MgA_2Z_4 structure and phase diagram

The spinel structure MgA_2Z_4 (with A = In or Sc and Z = S or Se), crystallizes with the anions in the face centered cubic (FCC) packing (space group: $Fd\bar{3}m$). In "normal" spinel structures, the higher valent cations (A = In^{3+} or Sc^{3+}), occupy octahedral (oct) sites 16d, as shown by the purple polyhedra in Figure 3.4c, and the Mg^{2+} occupy the tetrahedral (tet) 8a sites (orange polyhedra). Few spinels, such as $MgIn_2S_4$, can also exhibit "inversion", as experimentally observed by Gastaldi et al. [158], where a fraction of Mg^{2+} ions in the 8a exchange sites with the In^{3+} in 16d.

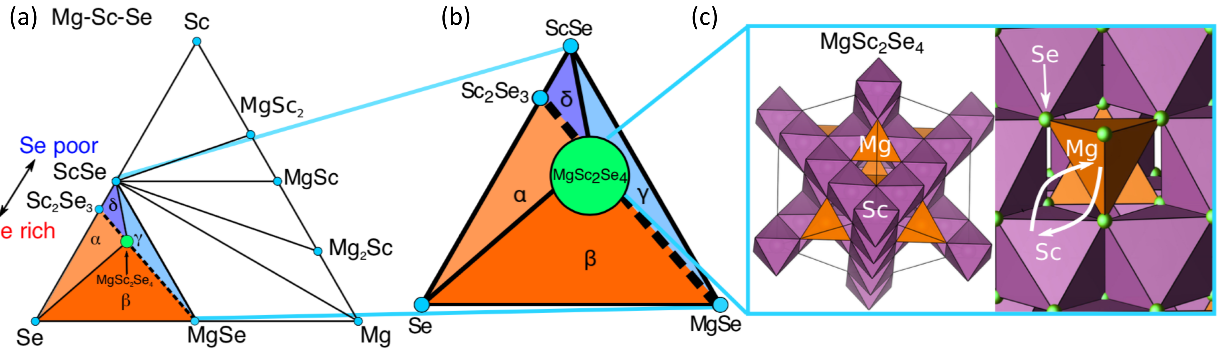

Figure 3.4: (a) Ternary Mg-Sc-Se phase-diagram at 0 K computed from DFT data combined with Materials Project, with (b) displaying a zoom-in of the concentration range of interest. (c) Crystal structure of a normal spinel, such as $MgSc_2Se_4$ identified in the phase diagrams of panels (a) and (b). The right fragment in (c) shows the scenario of spinel inversion (white arrows Mg ↔ Sc) in $MgSc_2Se_4$, leading to antisite Mg_{Sc} and Sc_{Mg} defects. Similar ternary phase diagrams for $MgIn_2S_4$ and $MgSc_2S_4$ are shown in Figure S4 of Reference [157].

The ternary 0 K phase-diagrams of Figures 3.4a and 3.4b depict four phases: Se, MgSe, ScSe and Sc_2Se_3 that can be in thermodynamic equilibrium with the ternary $MgSc_2Se_4$ spinel, at different atomic chemical potentials (μ_{Se} and μ_{Mg}). Equivalent phase diagrams have been constructed for the Mg-In-S and Mg-Sc-S systems and are presented in Figure S4a and S4b of Reference [157]. The four different facets of Figure 3.4a and 3.4b, namely α $MgSc_2Se_4$-Se-Sc_2Se_3 (light orange), β $MgSc_2Se_4$-Se-MgSe (dark orange), γ $MgSc_2Se_4$-MgSe-ScSe (light violet), and δ $MgSc_2Se_4$-ScSe-Sc_2Se_3 (dark violet), define the possible limiting chemical potential values for intrinsic point defect formation, such as vacancies (e.g., Vac_{Mg}) and anti-sites (e.g., Mg_{Sc}). Subsequently, the α and β facets can be classified as "Se rich" domains, owing to elemental Se forming one of the bounding vertices of the respective facets, while γ and δ are "Se poor". The dashed line in Figure 3.4a and 3.4b highlights the binary precursors, MgSe and Sc_2Se_3, which are used for the high-temperature synthesis ($\sim 1200^oC$) of $MgSc_2Se_4$ [144]. Off-stoichiometry of $MgSc_2Se_4$, will place the thermodynamic equilibrium during synthesis into one of the four facets α to δ, which in turn can influence the formation energetics and defect concentrations.

3.4.2 Native defect formation in $MgSc_2Se_4$

Figure 3.5 shows the formation energies of intrinsic defects in $MgSc_2Se_4$ obtained for chemical potentials defined by each of the four facets in the Mg-Sc-Se system. The y-axis of each panel in Figure 3.5 plots the defect energy against the E_{Fermi} (x-axis) in $MgSc_2Se_4$. The absolute value of the Fermi energy is referenced to the Valence Band Maximum (VBM) energy of the pristine $MgSc_2Se_4$ bulk. The zero of the x-axis is the VBM, with grey shaded regions being the valence ($E_{Fermi} < 0$) and the conduction bands ($E_{Fermi} > E_{gap} \sim 1.09$ eV), respectively. The band gap spans the white area in all panels of Figure 3.5. In general, the defect levels with low formation energies in the band gap can considerably alter the intrinsic electronic conductivity of semiconductors and insulators, thus forming the region of interest in this analysis.

Facets α and β (Figures 3.5a and 3.5b) are Se-rich, and show qualitatively similar defect energetics. For example, the defects with the lowest formation energies are the Sc_{Mg}, Mg_{Sc} and Vac_{Mg} in both α and β. Sc_2Se_3 has been previously detected as a prominent impurity in the synthesis of $MgSc_2Se_4$ [154], thus motivating the choice of facet α ($MgSc_2Se_4$-Se-Sc_2Se_3) to characterize the Se-rich domain. Similar conclusions are deduced by comparing the γ and δ facets (Figure 3.5c and 3.5d), with comparable formation energies for the low lying defects (e.g., Sc_{Mg}), and only the γ phase is considered further to analyze the Se-poor domain. Analogous behaviors are also observed for $MgSc_2S_4$ and $MgIn_2S_4$, showing similar trends for the S-rich and S-poor domains (See Figures S5 and S6 in the SI of Reference [157]).

Given the dominant defects (Sc^{+1}_{Mg}, Mg^{-1}_{Sc} and Vac^{+2}_{Mg}) of the Se-rich region, charge compensation causes E^{eq}_{Fermi} to be nominally pinned at midgap. Indeed, a self-consistent calculation of the E^{eq}_{Fermi} at 300 K (i.e., assuming defect concentrations equilibrate at 300 K) leads to a $E_{Fermi} = 0.46$ eV (see Figures 3.5a and S5a in the SI of Reference [157]), with defect concentrations of 7.9×10^{11} cm^{-3} for Sc^{+1}_{Mg}, 2.4×10^{11} cm^{-3} for Mg^{-1}_{Sc}, and 2.8×10^{11} cm^{-3} for Vac^{+2}_{Mg}. Typically, defect contents above 10^{15} cm^{-3} are detectable via experiments, such as electron paramagnetic resonance [8, 159, 160]. The "deep" Fermi level pinning for the α-facet of $MgSc_2Se_4$ at 300 K will lead to low electronic (or hole) conductivity since large thermal energies ($>> k_BT$) will be required to ionize free electrons (holes) from the E^{eq}_{Fermi} into the conduction (valence) band. Qualitatively similar conclusions about Fermi level pinning can be drawn from an analysis of the defects in the β facet (Figure 3.5b and Figure S7a of Reference [157]).

When defect concentrations are frozen-in at a higher temperature (~ 1273 K used for $MgSc_2Se_4$ synthesis [154]), the E^{frozen}_{Fermi} at 300 K drops below the VBM (~ 0.10 eV) indicating

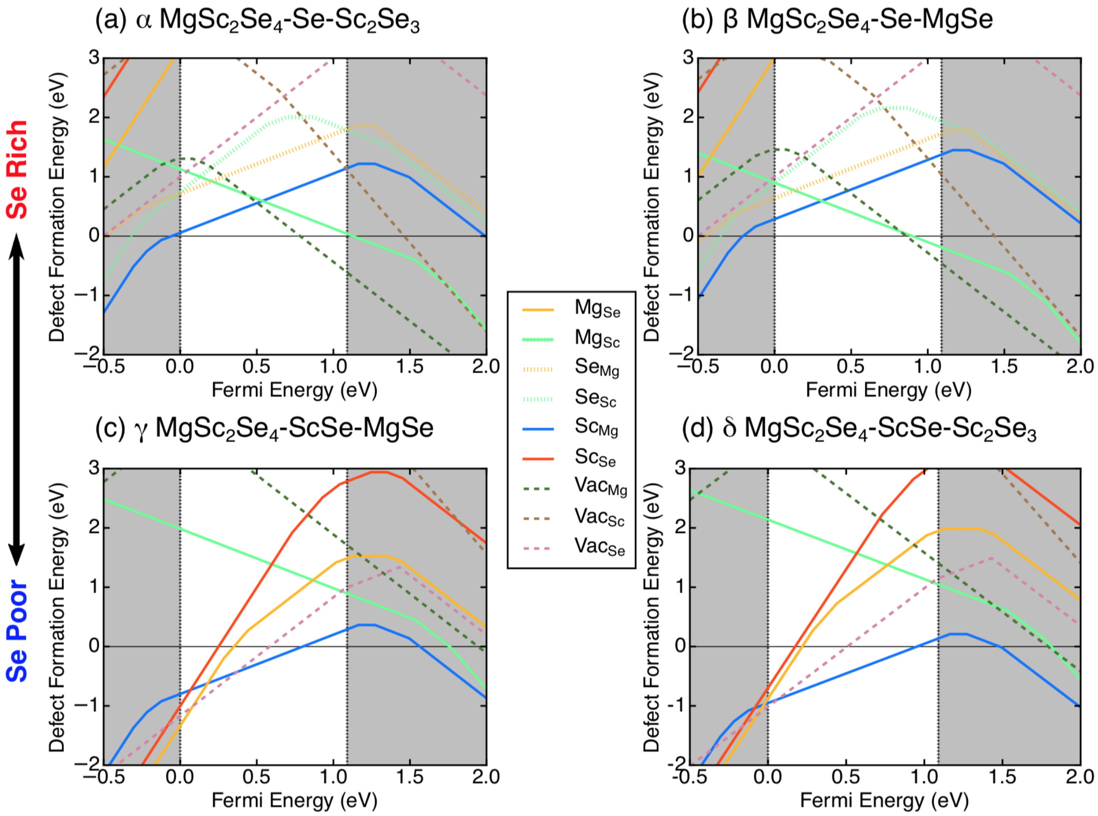

Figure 3.5: Defect formation energies for intrinsic point defects of $MgSc_2Se_4$ in four facets, α, β, γ, and δ, of the Mg-Sc-Se phase diagram. Regions α and β are Se-rich, whereas γ and δ Se-poor. The VBM is set to 0 eV and the white region spans the band-gap ($\sim$ 1.09 eV). Vac in the legend and dashed lines indicate vacancy defects while solid lines correspond to antisite defects.

that the material becomes a p-type conductor. Thus, significant hole conductivity can be expected under frozen defect conditions, with free hole concentration of $\sim 2.6 \times 10^{18}$ cm^{-3} ($\sim$ 0.0001 per lattice site), which is beyond un-doped semiconductor levels ($\sim 10^{10}$ cm^{-3} in Si) but below metallic levels ($\sim$ 1 charge carrier per lattice site). As the temperature at which the defect concentrations are quenched decreases, the E^{frozen}_{Fermi} recovers beyond the VBM and reaches $\sim$ 0.02 eV at 800 K (Figure S7a of Reference [157]), indicating the importance of slow cooling conditions to reduce hole conductivity during the synthesis of MgSc$_2$Se$_4$.

The Se-poor region (Figure 3.5c) is dominated by n-type defects, such as Sc^{+1}_{Mg} (dark blue), Vac^{-2}_{Se} (dashed red), and Mg^{-3}_{Se} (orange). This causes the self-consistent equilibrium Fermi level ($\sim$ 1.08 eV at 300 K) for the Se-poor region to be set by the Sc^{+1}_{Mg} defect. However, for temperatures above 300 K, the E^{eq}_{Fermi} exceeds the Conduction Band Minimum (CBM, $\sim$ 1.1 eV, Figure S7a of Reference [157]), suggesting the occurrence of spontaneous electronic conductivity when the spinel is synthesized under Se-poor conditions. Furthermore, when defect concentrations are frozen-in from $\sim$ 1273 K, E^{frozen}_{Fermi} is well above the CBM ($\sim$ 1.4

eV) at 300 K, suggesting that fast cooling during synthesis will likely increase the electronic conductivity. Similar conclusions can be extended by evaluating the defect energies in the δ facet (Figure 3.5d, and Figure S7a in the SI of Reference [157]), where the equilibrium Fermi level is beyond the CBM even at 300 K, suggesting that preventing intrinsic electronic conductivity in $MgSc_2Se_4$ in Se-poor conditions may be challenging.

For a similar discussion on the defect physics of $MgIn_2S_4$ and $MgSc_2S_4$, including a discussion about dopants, the importance of inversion in $MgIn_2S_4$ and chemical driving forces for antisite defect formation, see the full text of Reference [157]. We summarize all Fermi energies and free-carrier concentrations in Table 3.2 (defect concentrations are also tabulated in Table S1 of Reference [157]) for a representative anion-rich and anion-poor equilibrium in each system. Under all conditions, anti-sites ($Mg_{\{Sc/In\}}$ and $\{Sc/In\}_{Mg}$) and Mg-vacancies are the dominant defects, while anion vacancies only show up for $MgSc_2S_4$ under S-poor conditions.

Condition	Dominant Defects	E^{eq}_{Fermi}	$c[e/h]^{eq}$	E^{frozen}_{Fermi}	$c[e/h]^{frozen}$
		$MgSc_2Se_4$ (E_{gap} = 1.09 eV)			
Se-rich (α, h^+)	Sc^{+1}_{Mg}, Mg^{-1}_{Sc}, Vac^{-2}_{Mg}	0.46	8.42×10^{8}	-0.10	2.58×10^{18}
Se-poor (γ, e^-)	Sc^{+1}_{Mg}	1.08	7.96×10^{15}	1.39	2.77×10^{19}
		$MgIn_2S_4$ (E_{gap} = 1.77 eV)			
S-rich (α, h^+)	In^{+1}_{Mg}, Mg^{-1}_{In}, Vac^{-2}_{Mg}	0.88	6.46×10^{4}	0.10	1.17×10^{18}
S-poor (γ, e^-)	In^{+1}_{Mg}, Mg^{-1}_{In}, Vac^{-2}_{Mg}	1.53	4.10×10^{14}	1.80	1.12×10^{19}
		$MgSc_2S_4$ (E_{gap} = 1.55 eV)			
S-rich (α, h^+)	Sc^{+1}_{Mg}, Mg^{-1}_{Sc}, Vac^{-2}_{Mg}	0.40	2.01×10^{11}	-0.06	1.18×10^{19}
S-poor (γ, e^-)	Sc^{+1}_{Mg}, Mg^{-1}_{Sc}, Vac^{+2}_{S}	1.48	1.81×10^{15}	1.80	7.86×10^{19}

Table 3.2: Defect energetics in the MgA_2Z_4 spinels (A = Sc, In, Z = S, Se), for both anion-rich (α) and anion-poor (γ) conditions (facets). Self-consistent E^{eq}_{Fermi} at 300 K (in eV) and Fermi levels with quenched defect content (from 1273 K, E^{frozen}_{Fermi}), are indicated. $c[e/h]^{eq}$ and $c[e/h]^{frozen}$ (in cm^{-3} at 300 K) are the free charge-carrier concentration in the self-consistent equilibrium and frozen defect scenarios, with e^- and h^+ for electrons and holes. The charge of the dominant defect is indicated with respect to the charged state of the defect at E^{eq}_{Fermi}.

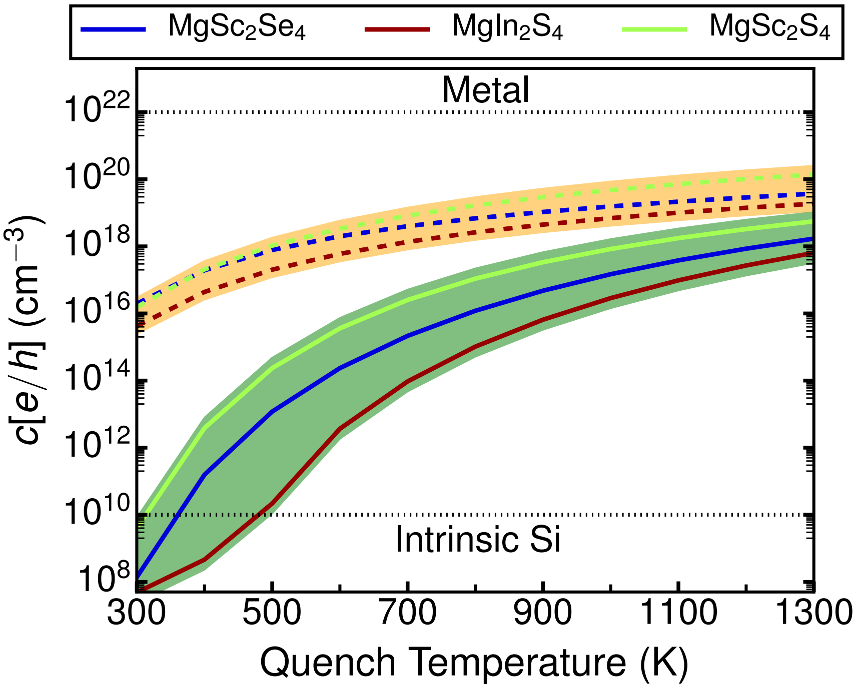

Figure 3.6: Free electron or hole concentrations $c[e/h]$ at 300 K as a function of temperature at which defect concentrations are quenched from. Solid and dashed lines indicate anion-rich (green-shaded) and anion-poor (orange-shaded) regions, respectively. The blue, red, and green line colors correspond to $\mathrm{MgSc_2Se_4}$, $\mathrm{MgIn_2S_4}$, and $\mathrm{MgSc_2S_4}$. The dotted black lines indicate the typical free carrier concentration in intrinsic Si (10^{10} cm^{-3}) and in metals (10^{22} cm^{-3}). The y-axis values at 300 K are the c[e/h]^{eq} for each spinel and values at 1300 K should indicate c[e/h]^{frozen} corresponding to quenched defect concentrations from typical synthesis temperatures [154]. For the case of anion-rich $\mathrm{MgIn_2S_4}$, the free carrier concentration is taken as the maximum of free electron and hole concentrations at each quench temperature.

3.4.3 Impact of cooling rates

The variation of $c[e/h]^{frozen}$ as a function of quench temperature —the temperature at which the defect concentrations are frozen - is plotted in Figure 3.6. For similar plots of $\mathrm{E}^{frozen}_{Fermi}$, see Figure S7 in the SI of Reference [157] Solid and dashed lines in Figure 3.6 correspond to anion-rich and anion-poor conditions, while the blue, red, and green colors indicate $\mathrm{MgSc_2Se_4}$, $\mathrm{MgIn_2S_4}$, and $\mathrm{MgSc_2S_4}$. The quench temperature, which is determined by the cooling rate, significantly impacts the hole/electron conductivity. For example, all three spinels are expected to show spontaneous h^+ conductivity at 300 K in the anion-rich domain (α facet, bold lines) when defect concentrations are quenched from 1300 K, contrary to the equilibrium scenario which would give negligible p-type conduction, as indicated by Figure 3.6 and Table 3.2. Furthermore, quenched defect conditions in the anion-poor domain (γ facet, dashed lines) dramatically increase the n-type conductivity in all spinels, resulting in c[e]^{frozen} that are $\sim$ 3 to 4 orders of magnitude higher than $c[e]^{eq}$ (Table 3.2, Figure 3.6). As a result, the synthesis of the chalcogenide spinels discussed in this work not only requires anion-rich conditions but also slow cooling post-synthesis (i.e., low quench temperatures, $\sim 400-500$ K, see Figure S7 in the SI of Reference [157]) to minimize the electronic conductivity.

3.4.4 Conclusions

Using first-principles calculations, we have analyzed the role of defect chemistry in influencing the electrical conductivities of three chalcogenide spinels, $MgSc_2Se_4$, $MgSc_2S_4$ and $MgIn_2S_4$, which are potential Mg-ion conductors. We find that intrinsic point defects, such as Mg-metal antisites (Sc_{Mg}^{+1} , Mg_{Sc}^{-1}) and Mg-vacancies (Vac_{Mg}^{-2}), dramatically affect the free carrier concentrations of the spinels under consideration. Additionally, controlling the anion-content during synthesis is an important factor in determining the defect energetics and the resultant electrical conductivity, with all three spinels exhibiting high n-type conductivity in anion-poor conditions and marginal p-type behavior in anion-rich conditions. Also, fast cooling leads to large concentrations of intrinsic defects being quenched within the structure, which can increase both the free hole (anion-rich) and free electron (anion-poor) concentrations in $MgSc_2Se_4$, $MgSc_2S_4$ and $MgIn_2S_4$. Hence, the lowest electronic conductivity is to be expected for samples synthesized under anion-excess, and slowly cooled to room temperature. Among the three structures considered, $MgIn_2S_4$ exhibits the lowest free carrier concentration across various conditions, largely due to inversion within the spinel. Our work indicates the importance of defects in the field of solid electrolytes, and the framework used here can be applied to other systems as well, which will eventually aid both in the calibration of existing candidates and accelerated materials discovery.

3.5 Solar Cells

Photovoltaic (solar) cells are able to absorb a photon of light to create an electron-hole pair which can then be swept out and used to power an electric load [161]. While many solar cell technologies exist, approximately 93 % of the global solar cell market is made up of silicon, the result of several decades of defect engineering [11,12]. While silicon is a cheap and abundant material as a result of the markets of scale created by the semi-conductor industry, it has an indirect band gap which requires the cells to be thick in order to have high absorption. Moreover, the fundamental thermodynamic limit to efficiencies, known as the Shockley-Queisser limit, causes marginal increases in efficiency to become more difficult and costly over time [162].

The remaining 7% of the global market which is not Silicon is primarily made up of thin film technologies, based on materials that typically have a direct band gap - thereby requiring less material to be present for an equivalent amount of solar absorption to silicon. Even less prevalent in the global market are tandem solar cells, which are not constrained by the single-junction Shockley-Quesser limit, as they make use of multiple material band gaps to split the solar spectrum [163]. The potential for a reduction in cost from reduced raw material or solution processable technologies [164], or the potential for higher module efficiencies in tandem solar-cells motivates the materials design challenge of finding new solar cell materials which have the potential to compete with silicon.

In this Section, we first present investigations into the defect physics of halide perovskite solar cells, a relatively new class of solar cells which have shown promising device efficiencies in the past decade. We then consider work done on CdTe, a well established thin-film solar cell material used commonly in space applications.

3.5.1 Halide Perovskites

Halide perovskite materials have garnered a considerable amount of attention in the optoelectronics space in the past decade [165, 166]. To illustrate one reason for the spike in interest, Figure 3.7 shows the maximum module efficiency for halide perovskites as compared to silicon solar cells, as a function of time. With just over a decade of engineering, maximum halide perovskite cell efficiencies have already surpassed that of multicrystalline silicon. Promising applications as LED nano-dots and as tandem cells with silicon have also contributed to a considerable interest in halide perovskite materials [163, 166].

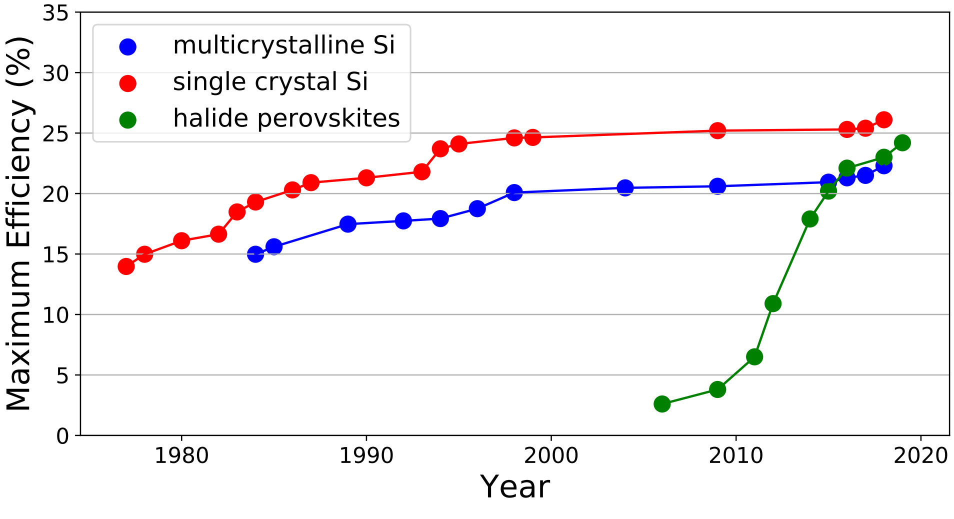

Figure 3.7: Timeline of silicon and halide perovskite record efficiencies. Data assembled from NREL's "Best Research-Cell Efficiency Chart" [167]

A conventional halide perovskite composition is made up of the ABX_3 formula unit, where A is either an organic molecule (such as methyl-ammonium = MA) or a large inorganic cation (e.g. Cs), the B-atom is a group IV element, and the X site is a halide anion. High efficiencies for the organic halide perovskite come from an ideal combination of strong photo-generation from the organic molecule, coupled with the high electron affinity and mobilities associated with the inorganic perovskite cage [168]. Moreover, material performance appears to not be limited by defects - so called “defect tolerance” - even though the precise nature of defects in $MAPbI_3$ has been debated [31, 38]. Despite these beneficial traits, a remaining concern for perovskites is their instability with respect to air, humidity, and UV light [169]. This has inspired a slew of theoretical efforts trying to survey the halide-perovskite composition space for additional favorable optical and electronic properties, with more favorable stability [37–39].

Given the importance of point defects for the high efficiencies of halide perovskite solar cells and LEDs, as well as the degree to which chemistry and structure are being surveyed for new halide perovskite materials, it is useful to consider the impact that chemistry and structure have on defect formation in halide perovskites. In the work that follows, we consider how small perturbations to composition and structure effect the Fermi level pinning across a variety of chemistry and structure polymorphs within Cs-based inorganic halide perovskites. All defect formation energies are computed with GGA-PBE functionals and the automation capabilities of the PyCDT package [136].

Figure 3.8 provides an overview of four $CsBX_3$ (B=Pb, Sn, Ge; X = Br, I) halide perovskite compositions considered presently. For all systems, the highest symmetry configuration corresponds to the cubic phase (blue), with perfect (un-distorted, unrotated) octahedra around the B-site cation. This high symmetry phase occurs at the highest temperature in each composition. For $CsPbBr_3$ and $CsSnI_3$, lowering temperature from the region of stability of the cubic phase corresponds to stabilization of the tetragonal phase (orange), which has undistorted octahedra that are rigidly rotated within the a-b plane. Further lowering of temperature in these two compositions results in the stabilization of the octahedral phase (green), which maintains the undistorted, rotated octahedra of the tetragonal phase, with additional rotations out of the a-b plane. For the $CsGeI_3$ composition, a reduction of temperature from the region of the cubic phase results in stabilization of the rhombohedral phase, which has slightly distorted octahedral cages around the B-site cation, modifying the Ge-I bond lengths. The orthorhombic-yellow phase of the $CsPbI_3$ composition is not considered in this work, as it is a severe departure from the corner sharing octahedrons of all the other phases.

We first consider the effect of composition changes on Fermi level pinning within cubic perovskites. Figure 3.9 is organized with B-site size decreasing from left to right, and X-site size decreasing from top to bottom. To simplify analysis significantly, we restrict our attention to trends in the Fermi level, as it is a tangible quantity that demonstrates the important macroscopic effects of intrinsic defect formation in a structure.

Considering the results of $CsPbI_3$ as a baseline, negatively charged cation vacancies force the Fermi level towards the VBM, while positively charged anion vacancies push the Fermi level towards the CBM. The net effect is to pin the Fermi level at 60% of the gap. Replacing the Pb atom with Sn atoms has a stabilizing effect on cation vacancies, which pushes the Fermi level significantly towards the VBM. This Fermi level behavior is consistent with the experimental observation of p-type behavior in $CsSnI_3$ [170]. The stabilization of cation

$CsPbBr_3$	$CsPbI_3$	$CsSnI_3$	$CsGeI_3$
Cubic (> 403K)	Cubic (>602K)	Cubic (> 426K)	Cubic (> 300 K)
Tetragonal (361 K to 403 K)	~~Orthorhombic-Yellow (<602K)~~	Tetragonal (351 K to 426 K)	Rhombohedral (< 300 K)
Orthorhombic (<361 K)		Orthorhombic (<351 K)	

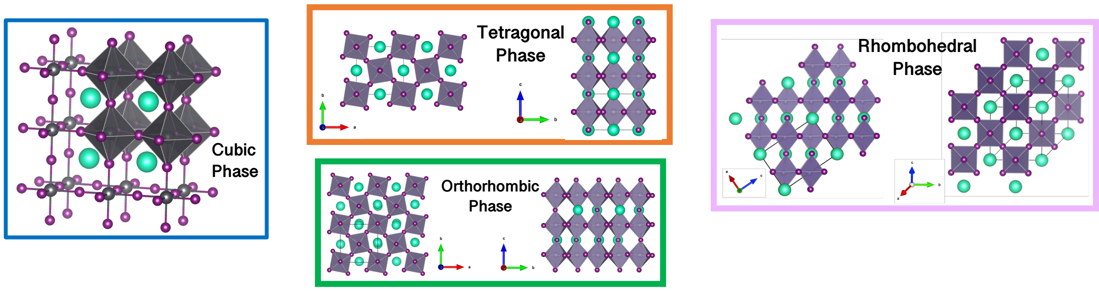

Figure 3.8: Overview of inorganic halide perovskite structures considered in this subsection. Color coding corresponds to variation in crystal structure and octahedral configuration.

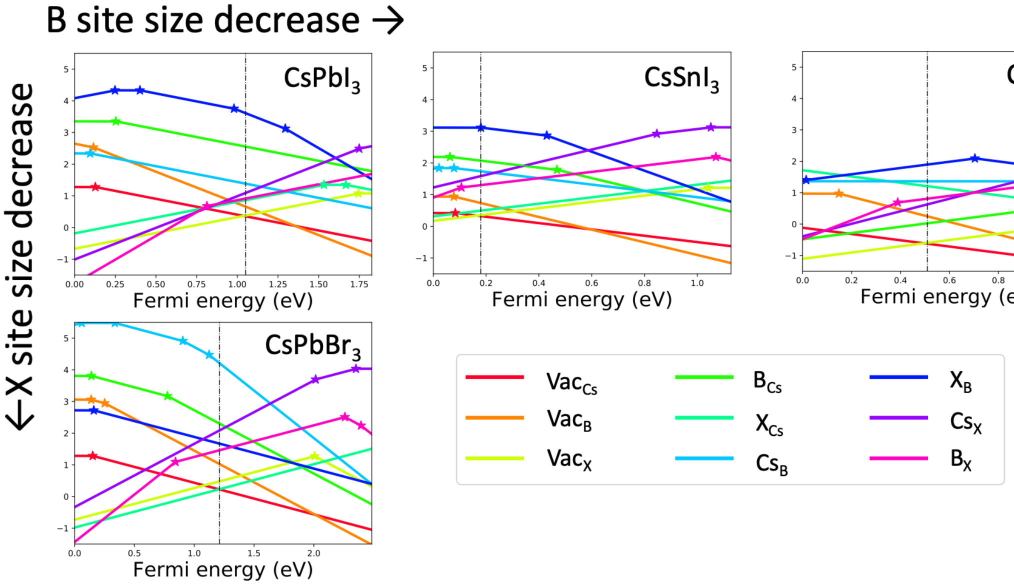

Figure 3.9: Isostructural defect formation energies for the $CsBX_3$-cubic chemistry, showing trends with changes in the B-site and X-site element size. Fermi levels are shown with dashed black lines. Chemical potentials are all defined by “B-rich” conditions (B-BX_2 of the GGA-PBE phase diagram).

vacancies could potentially be attributed to the lone-pair electron on Sn (discussed in Section 3.3 in the context of SnSe) which may act to destabilize the cubic polymorph of $CsSnI_3$, and lower formation energies for cation vacancies as a result of reduced coulomb repulsion.

This explanation of unique behavior in the Sn polymorph is further supported by previous work that showed lone pair effects in Sn-based cubic perovskites lead to anomalous deviations in electronic structure trends [171]. Upon changing the B-site cation from Sn to Ge, the halide vacancy stabilizes, causing the Fermi level to be pushed back towards the middle of the gap. The negative formation energies of the $CsGeI_3$ defect phase diagram are indicative of the stabilization of the rhombohedral phase for 0 K DFT calculations.

When considering changes in the halide (X-site) from I to Br, the relative stability of vacancies remains the same, with a slight stabilization of the halide-on-Cs antisite, but a nearly identical Fermi level pinning point relative to the VBM. However, the effect of replacing the halide site opens up the band gap, causing the Fermi level to be pinned in the middle of the gap, rather than in the upper half. This suggests that, for cubic isostructural trends, permutation of halides have less of a dominating effect on Fermi level pinning than movement of the gap itself.

Next we consider the effect of octahedral rotations on the Fermi level pinning behavior. Shown in Figure 3.10 are defect calculations performed for the $CsPbBr_3$ structural polymorphs. As described earlier, the cubic → tetragonal → orthorhombic series corresponds to increasing octahedral rotations. The cubic phase of $CsPbBr_3$ has a Fermi level that is pinned at mid-gap by negatively charged Cs vacancies and positively charged Pb_{Cs} antisites. Transitioning through the tetragonal and orthorhombic phases causes a lowering and subsequent increase of formation energies, respectively. The collective motion of defect formation energies, combined with a minimal change in the band gap, results in uniform mid-gap Fermi level for all phases considered, with nearly identical Fermi level values of 1.2 ± 0.1 eV above the VBM. This lack of change suggests that the rigid octahedral motions do not change the local bonding around each of the defects in $CsPbBr_3$, leading to qualitatively similar pinning behavior.

Lastly, we consider the effect of octahedral distortions on defect physics within the $CsGeI_3$ composition. Figure 3.11 shows defect formation energetics for the cubic and rhombohedral phases, with increasing distortions of octahedra going from left to right. In the cubic phase, Fermi level pinning occurs between cesium and iodide vacancies at approximately 0.5 eV (42% of the gap). The introduction of octahedral distortions in the rhombohedral phase has the effect of shifting the vacancy formation energies for cesium and iodide, while keeping the germanium vacancy formation energies relatively fixed. The net effect is to push the Fermi level down while opening up the gap, leading to slightly more p-type behavior in the distorted phase. Given the above analysis, the impact of distortions on bonding has a more direct effect on Fermi level pinning than the effect of octahedral distortions. This is consistent with the intuition that disruptions in bond angles would change the bonding character (i.e. relative hybridization amounts in the band edges), which subsequently changes the formation energy tendencies of point defects.

This preliminary analysis of the effect of structural and chemical permutations within the inorganic halide perovskites serves as a proof of concept for studies which can be done on a larger scale with the Python Charged Defect Toolkit (PyCDT) [136]. The work done here suggests that the effects of chemistry on Fermi level pinning can be predicted to first

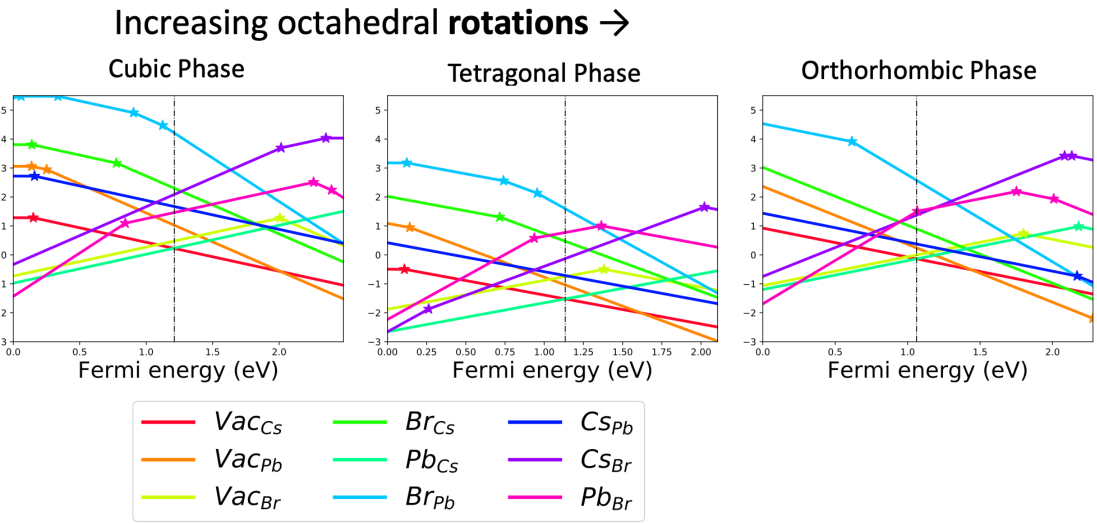

Figure 3.10: Defect formation energies for a single chemistry ($CsPbBr_3$) in three different phases which correspond to changes in octahedral rotations. Fermi levels are shown with dashed black lines. Chemical potentials are all defined by "B-rich" conditions (B-BX_2 of the GGA-PBE phase diagram).

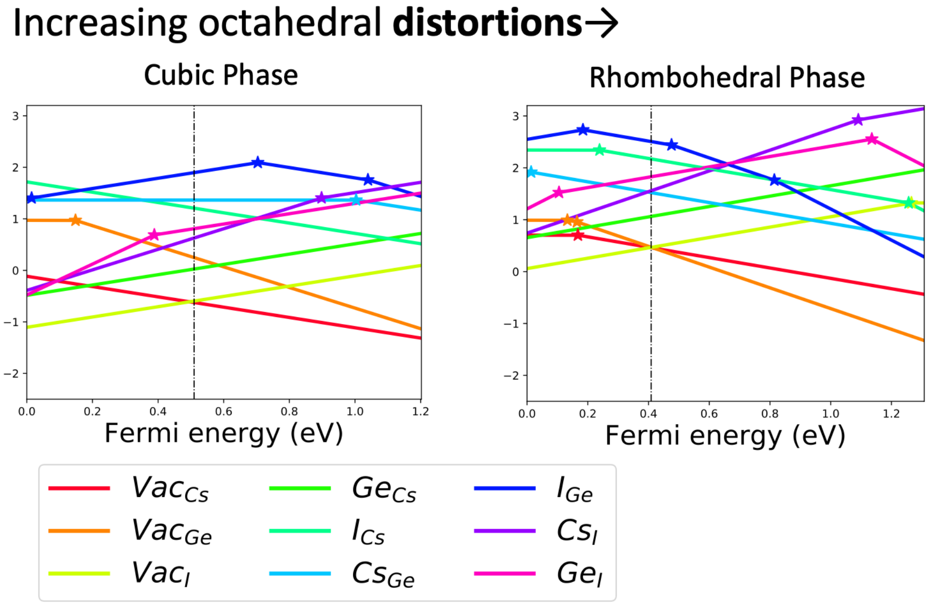

Figure 3.11: Defect formation energies for a single chemistry ($CsGeI_3$) in two different phases which correspond to change in octahedral distortions. Fermi levels are shown with dashed black lines. Chemical potentials are all defined by "B-rich" conditions (B-BX_2 of the GGA-PBE phase diagram).

order by the band gap, with occasional unpredictable defect stabilization as a result of unique electronic signatures, such as the lone pair effect discussed for $CsSnI_3$. In addition, the effect of structural rotations has less of an effect on the Fermi level pinning behavior than distortions of octahedral units. More work remains to be done to understand the physical origins of these trends, with more certainty coming from a larger dataset of defect calculations. Regardless, this work demonstrates the potential power of PyCDT and high-throughput screening procedures for point defect calculations with semi-local functionals in the halide perovskite space.

3.5.2 Impact of point defects on thin film CdTe

As mentioned earlier, thin film solar cells makes up the vast majority of the current non-silicon solar market. Within this subset of global sales, CdTe makes up the majority of the market share [12]. Market forces, expensive module encapsulation requirements, and stiff competition with the silicon solar cell market have limited the wide scale application of CdTe [12]. While the defect tolerance of CdTe has led to useful performance as an n-type material, the lack of adequate doping in the absorber layer is acknowledged as a major barrier for technological improvement [172]. The continued interest in the defect physics of CdTe provides motivation for methodological benchmarking with DFT defect computation.

Here we consider a comparison between computed defect formation energies from DFT against experimental results for electron concentrations in CdTe, given as a function of cadmium partial pressure [173]. Intrinsic antisite and vacancy calculations were performed with GGA-PBE functionals and the automation capabilities of the PyCDT toolkit [136]. We first describe the methodology considered for chemical potentials, band gap corrections, and the procedure for calculating a “frozen-in” electron concentration.

To adequately describe the chemical potentials, the Cd partial pressure must be taken into account. This is done using the following definitions for the chemical potentials:

$$\mu_{Cd}(P,T) = \mu^o_{Cd} + k_B T ln(\frac{P}{P^o})$$
$$\mu_{Te}(P,T) = \mu^o_{CdTe} - \mu_{Cd}(P,T)$$

Where μ^o_{Cd} is the reference chemical potential for cadmium, corresponding to the Cd partial pressure in the standard state ($P = P^o$). μ^o_{CdTe} is the reference energy for the bulk CdTe phase, taken to be the DFT energy per formula unit of the bulk supercell. For our analysis, we consider two different values for μ^o_{Cd}: (i) using μ_{Cd} from Cd-rich conditions of a GGA-PBE phase diagram for CdTe, and (ii) fit μ^o_{Cd} to minimize the error in experimental carrier concentrations. The resulting formation energies resulting from approach (i) are shown in Figure 3.12.

As discussed in other parts of this thesis (Sections 1.3 and 4.3.2), band gap errors with DFT have a drastic impact on defect formation energetics. To correct for these, we consider a modified band edge shifting routine based on the experimental gap, which produces different

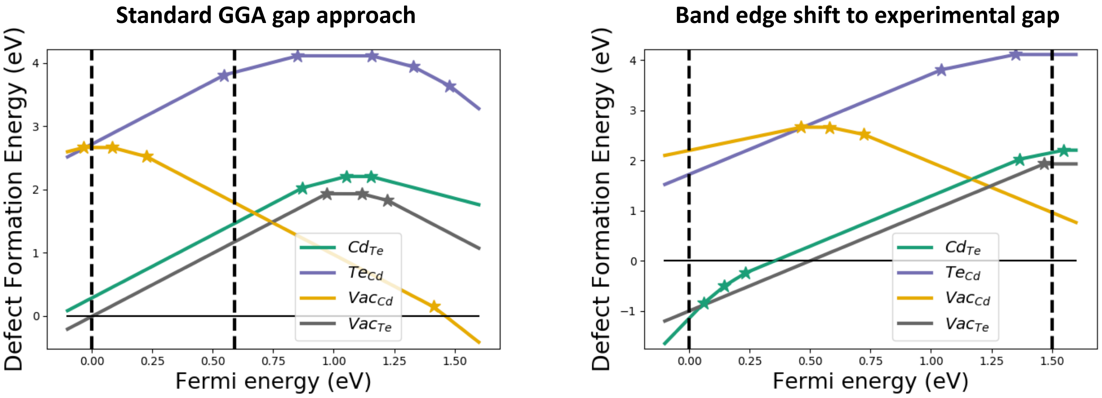

Figure 3.12: Formation energies for CdTe without (left) and with (right) band edge shifting corrections, as described in the text. Chemical potentials are derived from Cd-rich conditions in the GGA-PBE computed phase diagram of CdTe. All band edges are shown with black dashed lines.

shifts for the CBM and VBM in the formation energy. As discussed in the next chapter of this thesis, Fermi level renormalization, where the absolute position of the VBM from a semi-local functional calculation is shifted to the absolute position of the VBM from a hybrid functional calculation, results in better results for formation energies than a standard scissor operator which solely opens up the CBM to fit experiment.

To define separate band edge shifts for the CBM and VBM, we use the average electrostatic potential as a reference for shifting the band edges from GGA-PBE to HSE06 [174]. The percentage of total shift required for this CBM (VBM) shift is then multiplied by the total shift required to fit the experimental band gap, resulting in a modified CBM (VBM) shift. The relative band edge shifts $\delta E^{\text{Exp.}-GGA}_{CBM}$ ($\delta E^{\text{Exp.}-GGA}_{VBM}$) is summarized as:

$$\delta E^{\text{Exp.}-GGA}_{VBM} = \eta_{VBM}\Delta E^{\text{Exp.}-GGA}_{Gap} \qquad \delta E^{\text{Exp.}-GGA}_{CBM} = \eta_{CBM}\Delta E^{\text{Exp.}-GGA}_{Gap}$$

$$\text{where: } \eta_{VBM} = \frac{\delta E^{HSE-GGA}_{VBM}}{\Delta E^{HSE-GGA}_{GAP}} \qquad \text{where: } \eta_{CBM} = \frac{\delta E^{HSE-GGA}_{CBM}}{\Delta E^{HSE-GGA}_{GAP}}$$

Where $\delta E^{X}_{\{VBM,CBM\}}$ and ΔE^{X}_{Gap} are the band edge shifts and band gap differences for functional difference X (X=(HSE-GGA) or (Exp. - GGA)). With this procedure, one avoids having to perform computationally intensive hybrid functional defect calculations but gains a better band gap description for the formation energetics. The resulting band edge shifted formation energies are plotted on the right side of Figure 3.12 for chemical potential approach (i).

The experimental results from Reference [173] rely on measurements performed at room temperature but synthesized at an elevated temperature (700 and 900 K). Given the quick cooling rate of the experimental setup, the point defect concentrations are effectively fixed at their equilibrium value at high temperature while the free carriers are then equilibrated with these defect concentrations at room temperature. To model this, we repeat the “frozen-in” defect approach described in Section 3.4, by first calculating charge neutrality at an elevated temperature, which sets the frozen-in defect concentrations. With the defect concentrations held fixed, a second charge neutrality calculation is performed at room temperature. This low-temperature Fermi level, with the bulk DOS, is used to compute the electron concentration to compare with experiment.

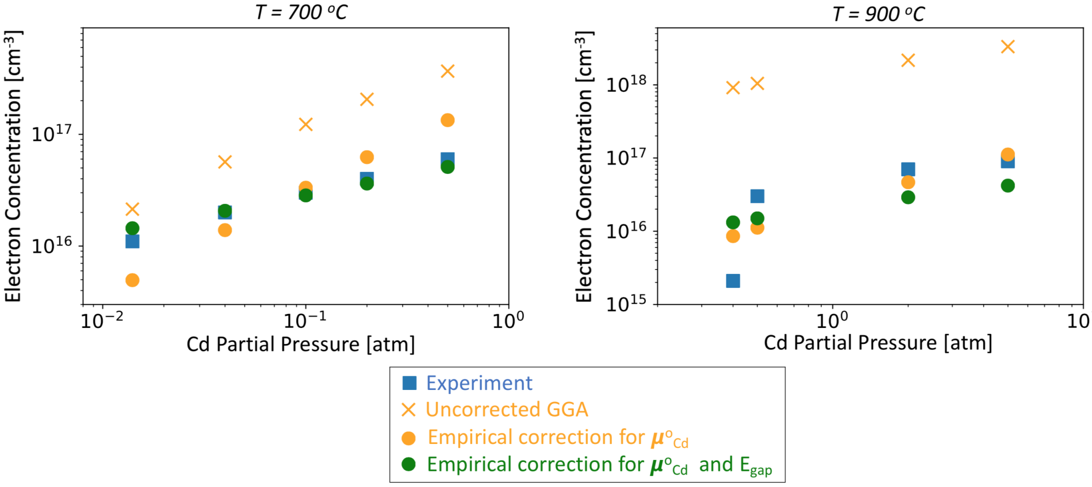

Figure 3.13: Comparison of electron concentration as a function of partial pressure for CdTe, derived from “frozen-in” point defects at 700 ^{o}C (left) and 900 ^{o}C (right). Corrections used are described in text. Experimental results (shown in blue) are from Reference [173].

The resulting computed electron concentrations at 700 and 900 K are plotted in Figure 3.13 with the experimental results (blue boxes) given by Reference [173]. Three different correction sets are given: (a) *Uncorrected GGA* uses the chemical potential convention given by a GGA-PBE phase diagram (chemical potential method (i)) and the GGA band gap, (b) *Empirical correction for* μ^o_{Cd} uses a reference chemical potential that is fit to minimize error (chemical potential method (ii)) and the GGA band gap, and (c) *Empirical correction for* μ^o_{Cd} *and* E_{gap} uses the fitted reference chemical potential (chemical potential method (ii)) and the experimental band gap shifting routine described earlier.

At both temperatures, the uncorrected GGA result (yellow X’s) gives an order of magnitude higher carrier concentration than the experimental results, with an RMS log error at 700 ^oC (900 ^{o}C) of 3.85 (4.31). Upon applying an empirical fitting correction to μ^o_{Cd} (yellow circles), a rigid shift in carrier concentrations occurs, reducing the RMS log error to 0.57 and 0.89 at 700 ^{o}C and 900 ^{o}C, respectively. As one would expect, solely shifting the carrier concentrations does not effect the slope in partial pressure dependence. However, upon the application of the band gap opening (green circles), the partial pressure dependence tilts to resemble the trend of experimental data, with RMS log errors of 0.15 (1.14) for 700 ^{o}C (900 ^{o}C).

The remarkable fit of the *Empirical correction for* μ^o_{Cd} *and* E_{gap} data (green circles) at 700 ^{o}C provides strong evidence for the origin of electron conductivity (at this temperature) arising from the intrinsic defects of CdTe - specifically, Fermi level pinning by the two opposing vacancies near the CBM. In the case of the 900 ^{o}C data (right side of Figure 3.13), a clear deviation from the partial pressure trend of the experimental data occurs below 10^0 atm. This suggests that additional physics is required to describe the partial pressure dependence. A potential avenue for correcting this is through the inclusion of interstitial defects - which Chen *et al.* (1998) suggested play a role in the n-type carrier concentrations at elevated temperatures [175].

Overall, the work performed here shows both the power and limitation of comparing first-principles point defect calculations against experiment. Qualitatively, trends and general slopes of carrier concentration with partial pressure are fairly well described with a band gap adjustment and without any empirical fitting corrections, assuming that a sufficient number of defects are computed. Quantitatively, numerical adjustments of the chemical potential to match experimental conditions are essential for reducing error. The exponential nature of the formation energy in the determination of defect concentrations means that small errors are exponentially propagated. Here we have fit the reference chemical potential for cadmium, resulting in a rigid shift of computed electron concentrations with an impressive RMS log error of 0.15 at 700 ^{o}C, after applying a band gap correction.

While fitting to minimize error relative to experiment is not an ideal procedure for high-throughput computation, it is possible to consider alternative chemical potential adjustments. For example, the chemical potential correction suggested in the work of Freysoldt et al (2016) only relies on fitting to bulk formation enthalpies, rather than carrier concentrations [176]. Such a correction may be more amenable to high-throughput as larger datasets of measured formation enthalpies begin to be accumulated within open source databases like the Materials Project.

3.6 Summary

In this chapter we have considered the application of the PyCDT toolkit to several specific materials with applications in thermoelectrics, batteries, and solar cells. This work serves to demonstrate the vast variety of applications which remain to be investigated with automated point defect calculation methods. Most of our analysis so far has focused on formation energies and the carrier concentrations determined by the position of the Fermi level, which is dictated by charge neutrality. However there are additional quantities of interest to the defect community; namely, defect transition levels and dopability limits. While this chapter gives a sense for the qualitative and quantitative limits of defect calculations with semi-local DFT, there remains to be seen a larger dataset for comparing the performance of such calculations. In the next chapter, we consider this question further, with the intention of informing and motivating further high-throughput studies of point defect calculations.

CHAPTER 4

Benchmarking Quantities for High-throughput

4.1 Forward

The work presented in this chapter is un-published work by D. Broberg and M. Asta. It makes use of hybrid defect calculations published in previous work by several other authors [50, 177–185]. The data from previous references is used and reproduced here with permission by the co-authors.

4.2 Introduction

High-throughput first-principles calculations using Density Functional Theory (DFT), are finding wide use for screening over candidate materials for a variety of potential applications [32, 39, 186]. This approach offers the possibility to expedite the materials discovery process and its application has been demonstrated in a vary of contexts including studies on solid-electrolyte batteries, transparent conducting oxides, and next-generation solar cells [35, 38, 157]. In many such applications a focus has been optoelectronic properties, and, despite the importance of intrinsic and extrinsic point defects in this context, the majority of previous high-throughput studies have focused on bulk property calculations like thermodynamic stability and electronic structure alone. Point defects dictate the carrier type and carrier concentration of semiconductor materials yet they are often not considered in high-throughput screening studies [8, 25, 26]. In part, this situation can be related to the time-consuming nature of point-defect calculations using first-principles methods based on density functional theory (DFT), and the relatively complex workflows that they can entail. In the past few years progress has been made to automate the setup and analysis of such calculations, and these efforts have thus addressed some of the hurdles towards conducting point-defect calculations in a high-throughput manner [18, 32, 61, 136, 187].

Modern studies of point defect computation make use of efficient DFT codes and periodic boundary conditions to calculate the dilute-limit formation energy [8]. This approach makes use of thermodynamics to determine macroscopic properties such as defect “trap” levels or the Fermi level arising from a given set of growth conditions. To capture the dilute-limit assumption that is implicit in most thermodynamic treatments of point defects, large "supercells" are used to remove the energetic contribution of periodic-image-interactions, leading to an increased computational requirement from every defect calculation performed. Moreover, the computationally efficient and commonly used semi-local exchange approximations, like the generalized gradient approximation (GGA) [21], suffer from a well-known underestimation of the band gap, an error which compounds for charged defects whose levels often lie close to the band edges.

To circumvent the issue of band gap underestimation, hybrid-functional approaches, which mix exact exchange with semi-local correlation at the expense of added computational cost, have become a "gold standard" for point defect computation with DFT [23, 30, 188]. While great strides have been made in improving the computational efficiency of hybrid functional methods, such calculations remain significantly more computationally expensive than those based on semi-local DFT. An alternative approach for high-throughput defect calculations is to make use of semi-local functionals with the application of *a-posteriori* corrections to remove the energetic contributions from band gap errors [8, 25, 26]. Such an approach remains an attractive prospect for developing large databases for initial screening studies in an efficient manner, while allowing for more in-depth quantitative follow-up calculations at a higher level of theory for interesting candidate compounds.

While many thorough reviews on point defect computational methodology have been written over the years, comparative studies of semi-local functional performance relative to hybrid have been confined to tens of calculations at a time [27,30]. To explore the application of high-throughput defect studies with semi-local functionals, this work benchmarks several defect quantities derived from semi-local defect calculations, performed in an automated fashion, against a dataset of 245 hybrid-functional point defect calculations published by several authors at lower levels of throughput [50, 177–185]. Section 4.3 provides an overview of the quantities and corrections to be considered in this work, as well as the automation procedure used. Section 4.4 details both a quantitative and qualitative comparison for structural and electronic relaxation of defect supercells (4.4.1), calculated thermodynamic transition levels (4.4.2), Fermi levels (4.4.3), formation energies (4.4.4), and dopability limits (4.4.5). Sections 4.5 and 4.6 conclude with comments on the viability of high-throughput approaches for calculating point-defect properties based on semi-local DFT approaches, emphasizing the potential for such calculations to aid qualitative screening of defect properties in semiconductors and insulators.

4.3 Methodology

4.3.1 Properties of point defects from DFT

As mentioned in Section 4.2, the dilute-limit formation energy for a single charged defect is commonly calculated using the supercell approach, wherein a single defect is placed inside of a supercell of the perfect lattice and internally relaxed with DFT [8,136]. The dilute limit formation energy is given by:

$$E^{\mathrm{f}}(X^q, \epsilon_{\mathrm{F}}) = E_{\mathrm{tot}}(X^q) - E_{\mathrm{tot}}(\mathrm{bulk}) - \sum_i n_i \mu_i + q\epsilon_{\mathrm{F}} + E_{\mathrm{corr}} \tag{4.1}$$

The first two terms on the right hand side of equation 4.1 are the DFT total energies for the charged defect supercell and bulk supercell, respectively. The third term is a summation over atomic chemical potential values (μ_i), or the energy cost of adding ($n_i = +1$) or removing ($n_i = -1$) atoms from the bulk, undefective supercell. Limiting values of the atomic chemical potentials can be calculated using the facets of a DFT phase diagram, corresponding to different growth or annealing conditions [14]. The fourth term is the defect charge (q) multiplied by the Fermi level (ϵ_{F}), which serves as the electron chemical potential reservoir. The final term is a set of corrections for removing periodic image interactions and band gap errors, to be elaborated on in Section 4.3.2.

The formation energy is traditionally plotted for a particular choice of atomic chemical potentials as a function of the Fermi level, with the “zero” value representing the valence band maximum (VBM). A qualitative example is displayed in Figure 4.1.

While the formation energy is essential for determining the concentration of a given defect in a specific charge state, it is seldom the quantity directly measured in experiment. Instead, one often considers the result of an ensemble of charged defects forming together. For a single defect type forming in multiple charge states, it is possible to consider defect transition levels which correspond to the energetic level at which a defect captures (or emits) a free carrier. These are highlighted as purple boxes in Figure 4.1 and are given by the equation:

$$\epsilon(q/q') = \frac{E^{\mathrm{f}}(X^q, \epsilon_{\mathrm{F}} = E_{VBM}) - E^{\mathrm{f}}(X^{q'}, \epsilon_{\mathrm{F}} = E_{VBM})}{q' - q} \tag{4.2}$$

where the formation energies (Equation 4.1) of the two defects are evaluated at the VBM, producing the Fermi level position of the transition level, $\epsilon(q/q')$, relative to the VBM. Since the same chemical composition exists for both defects in Equation 4.2, the quantity $\epsilon(q/q')$ has a value that is independent of the value of the chemical potentials, and hence is not affected by any ambiguities that may exist in their values for a specific application. If both defect energies are determined from their relaxed ground state, then Equation 4.2 yields the thermodynamic transition level. Many reviews have been written on the difference between optical and thermodynamic transition levels, including the work by Lyons *et al.* [30], where it was identified that semi-local functionals produce incorrect optical transition levels in GaN as a result of improper localization of charge on a defect.

Another class of quantities which can be considered are those that are derived directly from the collective consideration of all point defects within a system. This includes what can be referred to as the “dopability limit” which is the Fermi level that first produces defects with negative formation energy, indicating an instability in the structure with regard to producing defects at that Fermi level [32,189]. These quantities are shown as orange circles in

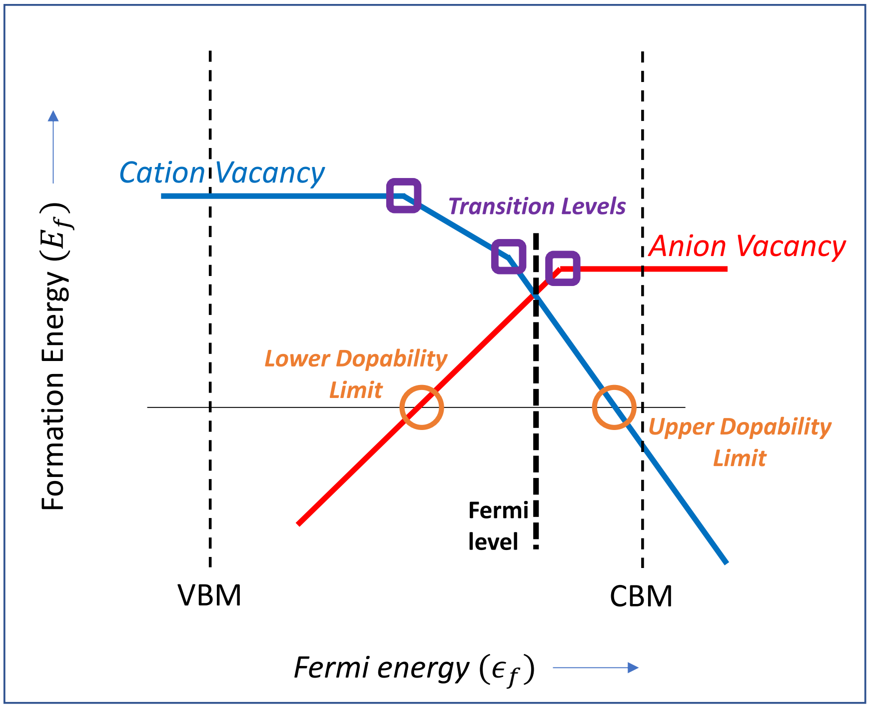

Figure 4.1: Schematic representation of formation energy diagram for defects, with a representative cation vacancy (blue) and anion vacancy (red). Band edges are shown as light dashed lines, while the Fermi level (dictated by charge neutrality) is displayed as a thick, dashed line. The upper and lower dopability limits are shown as orange circles, where the defect formation energies become negative. Transition levels are called out with purple boxes.

Figure 4.1. Pushing the Fermi level beyond the dopability limit violates the thermodynamic condition of structural stability, and is a fair signature of the dopability (whether a system can be doped with a certain carrier type with additional extrinsic doping) of a material. This can be particularly useful when screening for systems with a particular carrier type (p-type vs. n-type).

A further set of quantities that can be derived from consideration of the collective set of point defects are the carrier concentrations and Fermi level. These quantities are derived from the condition of charge neutrality:

$$\sum_{\{\mathrm{X,q}\}} q[X^q] + p - n = 0 \tag{4.3}$$

where the summation is over all defects, X^q, with concentration $[X^q]$. The charges from the point defects are counter balanced by the free hole (p) and electron (n) concentrations, determined from Fermi-Dirac statistics and the bulk DOS. For a fixed temperature and set of chemical potentials, Equation 4.3 can be solved self-consistently to determine the Fermi level, shown as a bold dashed line within Figure 4.1.

Beyond explicit quantification of the Fermi level and formation energies at that value, the qualitative description of defect structure, as well as the relative ordering of the formation energies of defects for a given set of chemical potentials may be useful for certain applications, such as oxygen-ion conductors where high concentrations of oxygen vacancies may be desirable. The exponential dependence of the defect carrier concentration on the formation energy makes this quantity central for such applications. Moreover, corrections which can reduce the intrinsic errors that result from self-interaction and band gap underestimation can drastically reduce the errors that result for quantitative values of many of the quantities described in this section.

4.3.2 Corrections

Several corrections have been proposed for improving the accuracy of point defect calculations in semiconductors [8, 25, 26, 136]. They can broadly be categorized into corrections related to supercell periodic image interactions and corrections related to band gap errors.

Supercell Periodic Image Interactions

The periodic boundary conditions employed in many DFT calculations lead to spurious interactions with neighboring image defects. The energy contribution from this interaction leads to a deviation from the dilute limit formation energy that needs to be corrected. These finite-size effets have been discussed at length in many reviews [8, 25, 26, 53, 60, 136].

For defects in semiconductors and insulators, charge can accumulate on the defect and long range coulomb interactions with neighboring image charges become a leading energy contribution to the finite-size effects. Moreover, a charged supercell causes an infinite bulk system to have a diverging electrostatic energy. To account for this second effect, a homogenous background charge is introduced to neutralize the supercell. This requires the use of a potential alignment method to remove the effect of the homogeneous background charge on the defect formation energetics. To account for both of these effects, Freysoldt *et al.* [65, 84] proposed a correction which can be seen as an extension of previous approaches based on calculations of the Madelung energy of an array of point charges in a neutralizing background charge [190], and involves a planar averaged electrostatic potential alignment method. Another extension of this method for systems with anisotropic dielectric constants was suggested by Kumagai *et al.* [66], and involves an atomic site averaged electrostatic potential. The potential alignment method procedures used in both of these corrections also can help to assess the localization the charge for a given defect.

Another effect arising from the finite-size of the calculation supercell is dispersion in the single particle state. This effect has been explored for occupied single particle states within the gap and a solution that has been proposed for addressing this effect is intelligent k-point sampling to “average” out the dispersion [25, 90]. In practice, the use of a sufficiently large supercell tends to make the energetic impact of dispersion from bandgap states negligible. However, in the case of occupied defect states near the band edges, as is the case for hydrogenic defects or perturbed host states, the supercell size required to sufficiently remove this effect drastically increases the computational cost required.

Near-band-edge defect states are dispersive in the same manner as the host bands. Lany and Zunger (2008) provide a useful explanation of this effect by invoking a perturbed host state explanation [26]. To correct this effect, a first-order bandfilling correction can be applied which removes artificial delocalization. Since a true defect level is dispersionless, any energetic occupation can be "moved" to the band edge as a first order correction to the effect of charge delocalization at the band edges. The bandfilling correction can be written for electrons as:

$$\Delta E^{e^-}_{\mathrm{MB}} = -\sum_{\mathrm{n,k}\in\mathrm{CB}} w_{\mathrm{k}}\eta_{\mathrm{n,k}}(e_{\mathrm{n,k}} - E_{\mathrm{CBM}}) \tag{4.4}$$

and for holes as:

$$\Delta E^{h^+}_{\mathrm{MB}} = -\sum_{\mathrm{n,k}\in\mathrm{VB}} w_{\mathrm{k}}(1-\eta_{\mathrm{n,k}})(E_{\mathrm{VBM}} - e_{\mathrm{n,k}}) \tag{4.5}$$

The summation is over bands in the Conduction Band (CB) or Valence Band (VB) with band index, n, and kpoint index, k. The variable w_k is the kpoint weight, $\eta_{n,k}$ is the occupation of the band index, and $e_{n,k}$ is the eigenvalue energy of the band index. The net effect is to "move the electron (hole) up (down)" to the band edge extrema.

Band gap corrections

As mentioned earlier, semi-local exchange approximations, like GGA, suffer from band gap underestimation. This causes severe problems for defects which have a defect level in the gap and may have delocalized resonant host band states as a result of gap underestimation. A natural way to correct for this is to extend the gap to fit a value derived from a higher level of theory or from experiment. The simplest way to do this is to extend the CBM outwards, in a manner which we will call a "Basic Scissor Operator." A schematic of this approach is shown on the left side of Figure 4.2.

The Basic Scissor operator band edge shift (BS_bes) does not renormalize the Fermi level in Equation 4.1, since the VBM is held fixed. An alternative approach is to renormalize the electron chemical potential by moving the band edges according to a common reference energy in GGA and Hybrid calculations. This has been demonstrated to work well for deep transition levels and for the averaged electrostatic potential (ESP) of a supercell [174, 191]. For the purposes of high-throughput calculations, the averaged ESP approach is fairly straightforward to implement. This averaged ESP referenced band edge shift (bes) approach is shown on the right side of Figure 4.2.

In addition to electron chemical potential renormalization, it has been suggested that adjusting occupied single particle states appearing within the gap may help to improve the accuracy of calculated defect formation energetics [26]. A simple way to achieve this is to

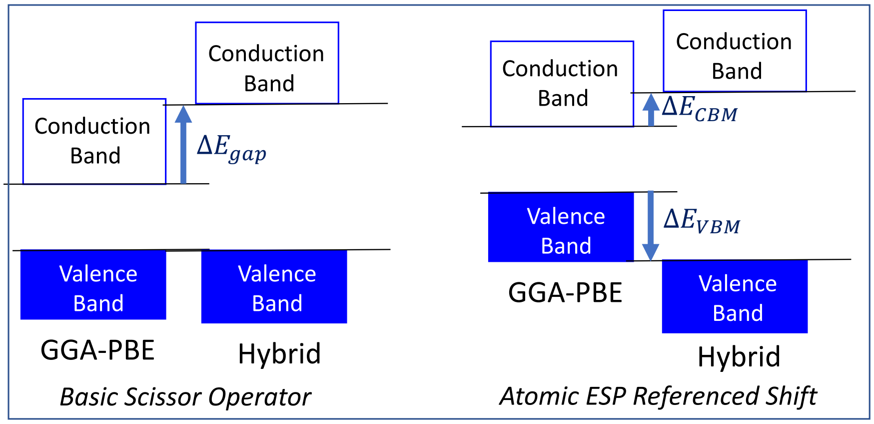

Figure 4.2: : Illustration of band edge shift approaches used for this paper. The Basic Scissor Operator (left) opens up the conduction band to the hybrid gap size, while the average electrostatic potential (ESP) referenced shift (right) moves the individual bands to the hybrid level using the average electrostatic potential as a reference.

fully shift any "free" electrons – occupied Kohn-Sham eigenvalues above the CBM which are corrected via the bandfilling correction – with the conduction band shift. For occupied states within the gap (further from the band edges) the direction for shifting can sometimes be ambiguous. Moreover, the deep-level alignment work done by Alkasukas *et al.* (2008) suggests that fully localized "deep" states should remain unshifted [191]. Within semi-local functional approaches, it is common to find occupied gap states which do not have localized wavefunction character. For such cases, a possible correction is to project the single particle wavefunction onto valence and conduction wavefunctions to produce a percentage of VB and CB character which can be used to shift the defect band [26]. To this end, Bystrom *et al.* [192] have recently developed an open source python code for setting up and projecting single particle wavefunctions onto host band states within the projector-augmented-wave (PAW) formalism.

In this work, we demonstrate the use of two different defect level shifting (dls) approaches which both include the use of the atomic ESP averaged band edge shift (bes) for Fermi level renormalization, as well as the charge correction and band filling corrections, where appropriate. The first level shifting correction (dls1) is a shift of the host band occupied states with the band edges. As discussed earlier for the bandfilling correction, host band states can become occupied within a defect calculation, and these can be corrected to first order by moving them to the band edges. Once the band gap opens up, these band edge states should presumably shift 100% with the band edges as well. (i.e. if n is the number of free electrons occupying conduction band states then the level shifting correction corresponds to $n\Delta E_{CBM}$). The second correction (dls2) is to apply the host band projection shift method to any occupied defect levels found within the gap, in addition to the free carrier shift (dls1) to account for delocalized states which should be shifted with the host bands. A summary of all the corrections considered within this work is given in Table 4.1.

Name	Acronym	Description
Charge Correction and Band Filling Correction	no_bes	Charge correction and bandfilling corrections applied to any delocalized band edge states
Basic Scissor Band Edge Shift	BS_bes	Band edge shifting via a basic scissor operator that extends the CBM to fit the hybrid band gap
Band Edge Shift	bes	Band edge shifts for the two band edges via a common reference point (average electrostatic potential)
Deep Level Shift Method 1	dls1	Same band edge shift as bes, with shifting of "free carriers" with their respective band edge extrema
Deep Level Shift Method 2	dls2	Same corrections as dls1, but with the addition of single particle level shifts based on projections onto host band states

Table 4.1: Overview of correction schemes used for this work. Note that all approaches include charge corrections and band filling corrections (no_bes). Where sufficient data was available, the planar-averaged Freysoldt correction was used as the default charge correction. In other cases, the atomic-site averaged method was used for the charge correction.

4.3.3 Defect workflow automation

As mentioned in the Introduction section, recently tools have been developed which aid in the automation of defect calculations [61, 136, 187]. This includes the Python Charged Defect Toolkit (PyCDT) produced by Broberg *et al.* (2018) [136]. Despite the work done to improve the setup and analysis stages of performing defect calculations, there is yet to be a demonstration of a fully automated workflow that is widely distributed and used by the community. To this end, we have merged the essential functionalities of PyCDT into the pymatgen [76], atomate [193] and emmet [194] code bases to produce a fully automated defect workflow which is compatible with the Materials Project infrastructure [36]. Details on the workflow and database design are outlined in Appendix D.

All DFT calculations considered in this study were performed using the Vienna Ab-initio Simulation Package (VASP) [195, 196], and the projector augmented wave (PAW) method [197] with a plane wave basis set. For the automated semi-local defect calculations, we make use of the Perdew-Burke-Ernzerhof implementation of the generalized gradient approximation (GGA-PBE) [21], with a plane wave cut off of 520 eV, and a gamma-centered k-point density of 100 kpoints/ Å^3, which is twice the density of standard (converged) relaxation approaches used with the Materials Project infrastructure [36]. Spin-polarized relaxation of atoms, with a fixed supercell volume, is allowed to occur until an energy tolerance of 0.001 eV is reached for ionic convergence, and an electronic self-consistency tolerance of 0.0001 eV. For the computational details of all hybrid calculations, see the text of previously published work from which the benchmark data is gathered [50, 177–185].

4.3.4 Approach for benchmark comparison

For this work, we benchmark defect properties calculated by GGA with the correction schemes described above against a set of 245 "gold standard" defect calculations carried out with careful implementation of hybrid functionals in several previously published works [50, 177–185]. The chemistry and types of defects explored in the benchmark set is displayed in Figure 4.3.

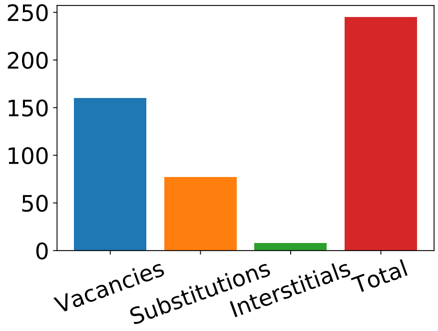

(a) Total number of defects, broken down by defect type.

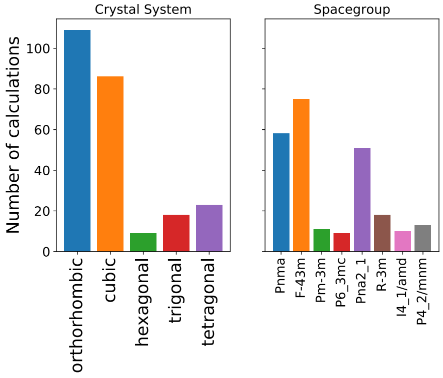

(b) Defects broken down by crystal system and spacegroup symbol for the host crystalline compound.

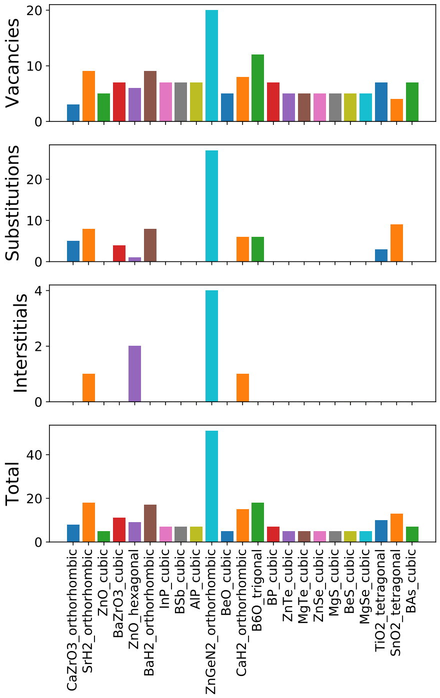

(c) Total number of defects, by type, for each chemistry and structure type.

Figure 4.3: Overview of defects considered in this work.

For the remainder of this paper, we present and analyze the differences between hybrid and GGA-PBE-based results (referred to in what follows as "errors" associated with the

GGA-based approaches) arising between (i) differences in structural relaxation and electronic delocalization in the defect supercell calculation (Section 4.4.1), (ii) transition levels (Section 4.4.2), (iii) Fermi levels (Section 4.4.3), (iv) formation energies (Section 4.4.4), and (v) dopability limits (Section 4.4.5).

For the errors analyzed in (iii) – (v) a choice for the chemical potentials was required. These quantities should, in principle, be calculated from the phase diagram produced by the same level of theory of the calculations (i.e. including the same PAW potentials and exchange correlations as the defect calculations). However, the previously published hybrid functional data involves a large array of different PAW potential implementations, as well as differences in the practical definitions for chemical potentials. As an example of the latter, in some calculations experimental values are used to fix some of the chemical potentials. To ensure a consistent comparison with our fully automated defect calculations, we chose to use chemical potentials produced by the GGA-PBE calculated phase diagram available within the Materials Project across all calculations. Alternative methods for determining chemical potentials under the condition of perfectly stoichiometric conditions, as detailed in Reference [75], were also considered. The results from this approach did not change the primary conclusions reached in this work, so we do not discuss results from this alternative approach further.

For all quantities apart from the structural and electronic differences (Section 4.4.1), we analyze the errors resulting from the different correction combinations outlined in Table 4.1. These corrections were detailed at length in Section 4.3.2. For all of the systems considered, we use identical sets of defect + charge calculations for both hybrid and GGA. Moreover, several systems had quantities which were impossible to calculate within the bounds of thermodynamics (i.e. Fermi levels can not be calculated if formation energies are negative across the entire gap), and these subcases are mentioned where relevant.

To compute hybrid formation energies and corrections, raw data for every hybrid calculation was inserted into the defect database described in Appendix D. After successful integration into the database, the workflow infrastructure was used to compute charge corrections and band filling corrections. The Freysoldt correction was prioritized in cases where the planar average electrostatic potential was available, and the Kumagai anisotropic extension of Freysoldt's correction was used in all other cases. These corrections should be identical in the case of isotropic dielectric constants, as is the case for all of the compounds considered in this study.

The primary motivation of this work is to benchmark the performance of automated, semi-local point defect calculations. Associated with this goal are several difficulties in the analysis of thermodynamic quantities, as a result of different hybrid computational approaches used in the literature and benchmarked in this study. For example, band edge shifting corrections of PBE-GGA results required a hybrid band structure calculation in a primitive unit cell for alignment of the band edge extrema with respect to the averaged electrostatic potential [174]. For automation purposes, a single hybrid functional approach was chosen - namely, the implementation by Heyd, Scuseria, and Ernzerhof (HSE06) [23], which has shown to balance computational efficiency with significant improvements in thermochemical results relative to semi-local [24]. As a result of the different (non-HSE06) hybrid implementations that exist within the benchmark set, some differences exist between the computed band gaps of the previously published data and the hybrid gaps generated by the automated defect workflow. Details on computed band gaps, as well as the hybrid version which was used in each bulk system in previously published data is given in Appendix E.

While the automation workflow has the ability to rerun defect calculations in larger supercells, this study chose to only run supercell sizes which contained no more than 300 atoms. In addition, no local perturbations around the defect site were introduced at the beginning of the DFT relaxation. Symmetry was also left on during the relaxation process to improve computational requirements. As noted later in this work, these limitations make it difficult to distinguish errors which are artifacts of the calculation setup (local structural initialization or supercell size), from errors which are due to the intrinsic limitations of the GGA-PBE functional approach. Improvements in automated, semi-local GGA-PBE through the introduction of local perturbations or increases in supercell sizes will be investigated in future work. In the discussion that follows, we make a point of calling attention to errors which may be improved with such approaches.

4.4 Results and Discussion

4.4.1 Structural and Electronic Relaxation

The degree of structural relaxation or electronic delocalization greatly influences the energetics of a DFT point defect calculation. Large amounts of structural or electronic delocalization indicate a larger supercell may be required to improve the physical description of the defect, but small amounts of delocalization may always exist - as is the case for a hydrogenic defect level. In this sub-section, we analyze several quantities which lend themselves to analysis of structural and electronic delocalization for the purposes of a high-throughput workflow.

One way to define structural relaxation is by integrating the (non-defect site) atomic displacements as a distance from the defect. If the total modulus of the distance moved by atom index i during the DFT relaxation is given by τ_i, then the total integrated motion is defined here as $\sum_i \tau_i = T$. If we define a “localization” radius, w, then we can retrieve the total integrated relaxation within the localization radius through the use of a Heaviside function:

$$T_w = \sum_i \Theta(w - r_i)\tau_i \tag{4.6}$$

where r_i is the distance between the defect and atom index i before the relaxation. Similarly, the percentage of total motion within the localization radius is given by:

$$f_T = 100\% \times \frac{1}{T}\sum_i \Theta(w - r_i)\tau_i \tag{4.7}$$

Equations 4.6 and 4.7 can be used to investigate the magnitude of "long-ranged" structural relaxation, which may lead to spurious elastic interactions that give rise to interactions between periodic images that are not accounted for in the correction schemes described in the previous section. Figures 4.4a and 4.4b display violin plot distributions of the *difference* in these two quantities as computed with GGA and hybrid, for every defect. The localization radius was chosen as the Wigner-Seitz radius of the supercell (the maximum radius of a sphere contained within a Wigner-Seitz cell of the supercell lattice).

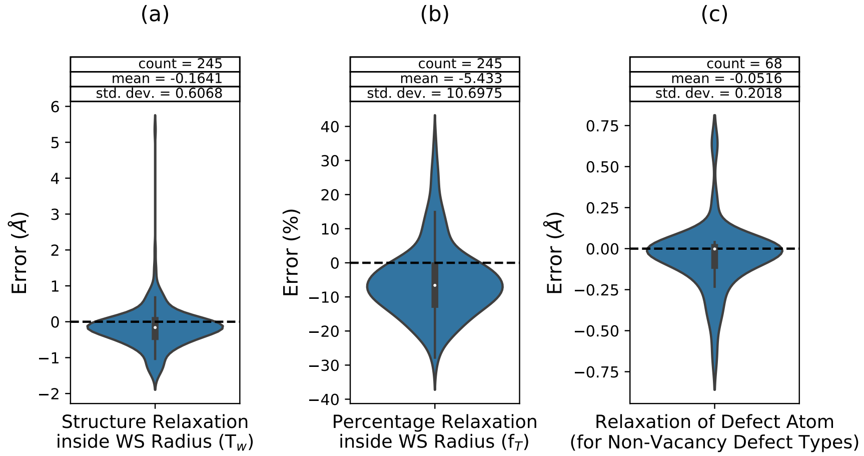

Figure 4.4: Differences in structural relaxation properties (GGA − hybrid) displayed as violin plots. See text for description of each property.

As listed in the inset tables of Figures 4.4a and 4.4b, average differences in the structural relaxation amounts within Wigner-Seitz radii are less than zero (hybrid has a larger value than GGA, on average). In addition, 75% of the errors shown in Figure 4.4b are less than zero. This is consistent with the expectation that hybrid functionals tend to have more local structural relaxation than semi-local functional approaches [30]. Despite this apparent trend, several differences were positive (GGA larger than hybrid). For example, four defects have relaxation differences greater than 2 Å in Figure 4.4a. We believe this is due to symmetry locking around the defect, causing excessive movement in nearest neighbor atoms to preserve symmetry during relaxation. Relaxation of this nature could be removed with improved local perturbation routines during the high-throughput workflow, a topic for future work.

Another useful structural relaxation metric to consider is the total movement of the defect site itself - that is, the total modulus of the distance moved by the defect index D during the DFT relaxation: τ_D. DX centers like Si in AlGaAs require a large amount of relaxation of the Silicon atom, which have previously caused issues for theoretical modeling [25, 198]. Figure 4.4c, shows the differences in defect site relaxation (τ_D) for all non-vacancy defect sites between GGA and hybrid. The distribution lies relatively symmetric around zero, with a slight skewing towards more negative errors (larger relaxations in hybrid). All relaxation differences with positive values greater than 0.25 Å are interstitial defects which relaxed further in the semi-local calculation, potentially due to the inaccurate accommodation of coordinating atoms around the defect within the high-throughput setup routine. All of the relaxation differences with negative values less than -0.25 Å involve substitutional defects with a size mismatch that would need to be accommodated for by nearest neighbor atoms. As discussed in Section 4.3.3, we have not yet distinguished whether such errors result from the automation procedure, or whether the error is a more fundamental one within the semi-local DFT implementation. The ability to use local coordination adjustments to reach global energy minima is a subject for future work.

Electronic delocalization during a defect calculation is another important quantity to monitor in charged defect calculations. As outlined in the description of bandfilling corrections in Section 4.3.2, it is possible for Kohn-Sham eigenvalues to become occupied (unoccupied) in the conduction band (valence band) as a result of artificial dispersion of the defect level or band gap errors from the semi-local functional approach [26]. These new occupations can be considered as "free electrons" ("free holes") which should actually be localized on the defect state in the limit of an infinite supercell size and a perfect band gap description. While the true free carrier amounts in the crystal are ultimately dictated by the position of the Fermi level, which is calculated from charge neutrality (as described in Section 4.3), the free carrier amount discussed presently is a computational artifact that helps determine the amount of charge that is adequately localized on the defect state.

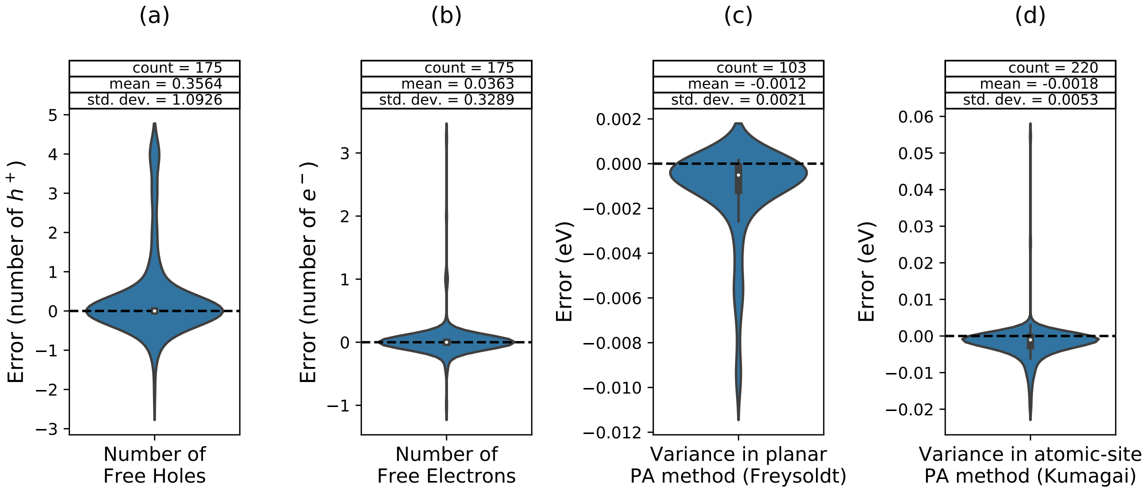

Figure 4.5: Differences in structural and electronic-related properties (GGA – hybrid) displayed as violin plots. See text for description of each structural and electronic property.

Figures 4.5a and 4.5b show violin plot distributions of the difference in the number of free carrier amounts found in the GGA and hybrid calculations. The large window of errors for free carrier differences is related to their extreme dependence on the value of the potential alignment (PA). The VBM of a charged defect calculation must be shifted to account for the PA, causing small errors in PA to cause unoccupied defect states near the VBM to be considered as free holes and occupied defect states near the CBM to be considered free electrons.

A larger standard deviation of 1.1 exists for holes, as compared to a standard deviation of 0.3 for electrons. Additionally, the number of free hole differences greater than 1 is 23, while the number of free electron differences greater than 1 is only 2. The tendency for excessive hole formation can be explained by inadequate charge accommodation after initializing the defect calculation from a perfect bulk structure. Since the defect calculation is not relaxed from an occupied defect configuration, any removed electrons must initially come from the VBM and, if a correct defect structural configuration is never achieved, these unoccupied states will remain inside of the VBM. This is yet another error that may arise from the workflow implementation rather than a general error of GGA, and it is possible that improvements would occur with more intelligent initialization of the local coordination environment. Future work should be done to investigate whether the calculation of more positive charge states from the occupied defect structure configuration improves the number of free carriers at the end of the calculation.

Freysoldt et al. proposed the planar averaged PA and the use of a resulting “plateau” within the sampling region far from the defect as a visual cue for defect localization [65,84]. As an extension of the Freysoldt method to anisotropic dielectric constants, Kumagai et al. used an atomic site averaging PA method to do a similar version of localization analysis far from the defect [66]. Figure 2.8 in Section 2.4.3 provides an example of how planar averaged plotting is displayed in practice. It is worth noting that, even for a localized defect, some deviation from the “plateau” behavior often occurs in practice as a result of negligible amounts of charge delocalization or the minor movement of atomic core states far from the defect. As a metric for quantifying the total deviation from full localization of the short range potential, we consider the statistical variance of the short range potential in the sampling region, as computed by the planar PA and atomic-site PA methods. Differences for this quantity between GGA and hybrid are shown in Figures 4.5c and 4.5d, respectively. Both PA method differences have a mean value which is slightly negative, providing further evidence that the hybrid calculations are localizing defect charge more effectively than GGA calculations. Large deviations in the computed variance are considered further in the compatibility approach discussed in Section 4.4.4.

4.4.2 Thermodynamic Transition Levels

Figure 4.6 shows the differences in calculated thermodynamic transition levels (Equation 4.2) between the GGA and hybrid calculations, with and without scaling according to the band gap size. For the unscaled results, average values are mostly negative (only slightly positive for the bes correction), indicating that GGA tends to underestimate transition levels relative to hybrid. For the gap-scaled results, the no_bes performs similarly to the best case band edge shifting routines. A summary of errors and standard deviations are provided in Table 4.2.

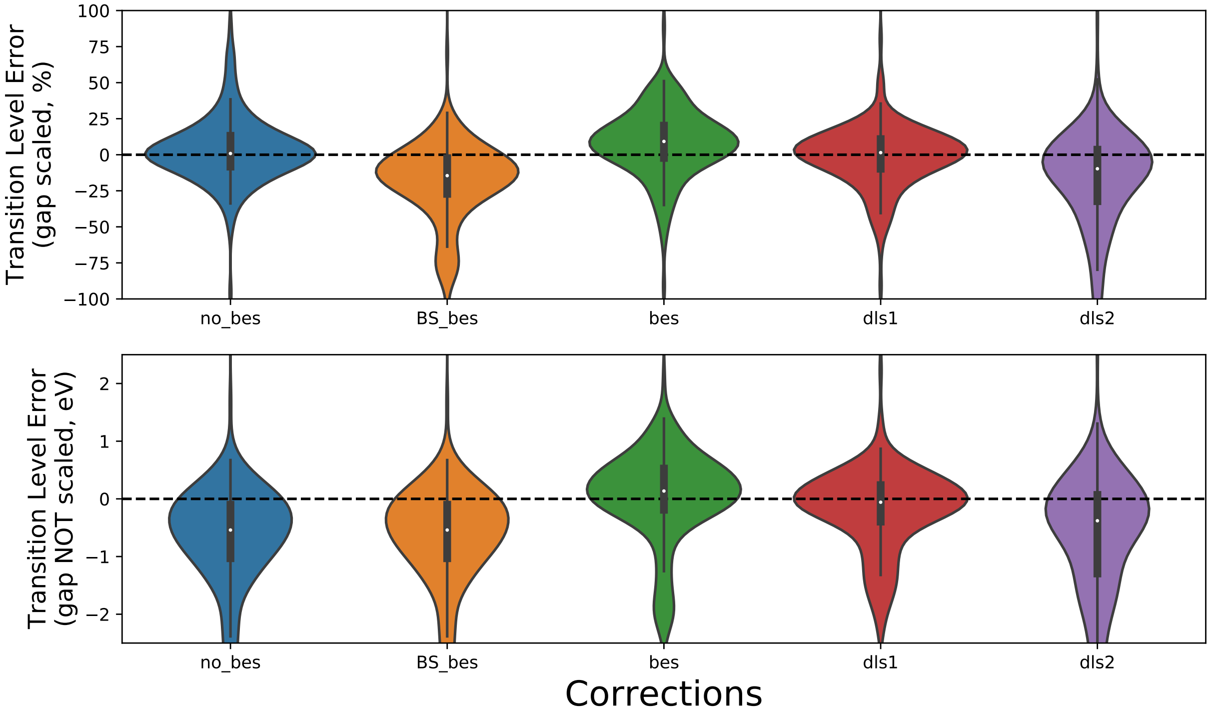

Figure 4.6: Thermodynamic transition level errors (GGA – hybrid) displayed with and without gap scaling.

Transition Level Error (gap scaled, %)					
Value	no_bes	BS_bes	bes	dls1	dls2
Mean Error	3.8	-17.4	8.7	-0.6	-17.7
Absolute Mean Error	15.7	23.5	19.2	15.4	27.3
Var. in Error	6.0	8.1	6.5	5.7	16.4
Var. in Absolute Error	3.6	5.6	3.6	3.3	12.0

Transition Level Error (gap NOT scaled, eV)					
Value	no_bes	BS_bes	bes	dls1	dls2
Mean Error	-0.7	-0.7	0.1	-0.2	-0.7
Absolute Mean Error	0.8	0.8	0.6	0.5	0.9
Var. in Error	0.9	0.9	0.7	0.5	1.5
Var. in Absolute Error	0.7	0.7	0.3	0.3	1.1

Table 4.2: Errors for Figure 4.6

With gap scaling, the dls1 minimizes error better than all other correction schemes, with an absolute mean difference of 15.4% (absolute mean variance of 3.3%) relative to the hybrid calculations. While no band edge shifting (no_bes) does not perform as well as dls1, it still outperforms all other corrections considered. The BS_bes correction results in a skewing towards more negative errors (underestimation of GGA relative to hybrid), as a result of opening up the CBM without moving the VBM. The bes correction skews towards positive differences and increases the mean and absolute mean errors to 8.7% and 19.2%, respectively. This indicates an improved comparison with the application of free carrier shifts when performing band edge shifts, as in the dls1 correction. The host band shift (dls2) correction increases the variance (16.4%) and average absolute error (27.3%), such that it performs the worst out of all correction sets considered.

Without gap scaling, the no_bes, BS_bes, and dls2 corrections have the largest absolute errors, with absolute mean errors of 0.8 eV, 0.8 eV, and 0.9 eV, respectively. Moreover, the largest variance (1.5 eV) occurs, once again, with the dls2 correction. The dls2 correction's large variance suggests an inconsistent performance of universally applying the host band projection correction, a subject for future discussion and consideration. The bes and dls1 corrections once again improve performance relative to other corrections, with absolute average errors of 0.6 eV and 0.5 eV respectively. Their distributions are also positioned fairly uniformly around zero error, indicating no statistically significant under or over-estimation of transition levels relative to the hybrid benchmark case. For these two corrections, the largest errors primarily derive from hybrid transition levels lying outside of the gap: out of 132 transition levels lying inside the gap as hybrid calculations, 76% have absolute errors less than 0.5 eV, as compared to 19% within this window of error for the 54 outside-of-gap transition levels.

While quantitative assessments are useful for comparing directly with experiment, it is rare to make use of quantitative transition level values produced by semi-local functionals. Instead, the qualitative position of transition levels being deep or shallow can be used to label defects as problematic or not for optoelectronic applications. To assess the ability of high-throughput semi-local approaches for screening in this qualitative manner, we display the confusion matrix for predicting shallow and deep levels for the each of the five corrections in Figure 4.7. Any transition level in the window of 25% - 75% of the gap is considered a "deep" level and anything outside of that window is considered a "shallow" level.

For estimating shallow vs. deep transition levels, the no_bes and dls1 corrections perform better than all other corrections, with an 83% and 82% success rate, respectively. All other corrections achieve a reduced success rate of 70±5% as a result of reducing the number of correctly predicted shallow levels (predicting too many deep levels). However, both level shifting schemes (dls1 and dls2) improve in the number of false negative deep levels as compared to the bes correction, suggesting that level shifting helps improve the description of deep levels when band edge shifting is implemented.

The dominant failure of the no_bes correction was the prediction of false shallow levels. This failure is consistent with the fact that hybrid calculations often achieve larger local relaxation than semi-local calculations, resulting in deeper transition levels. The missing

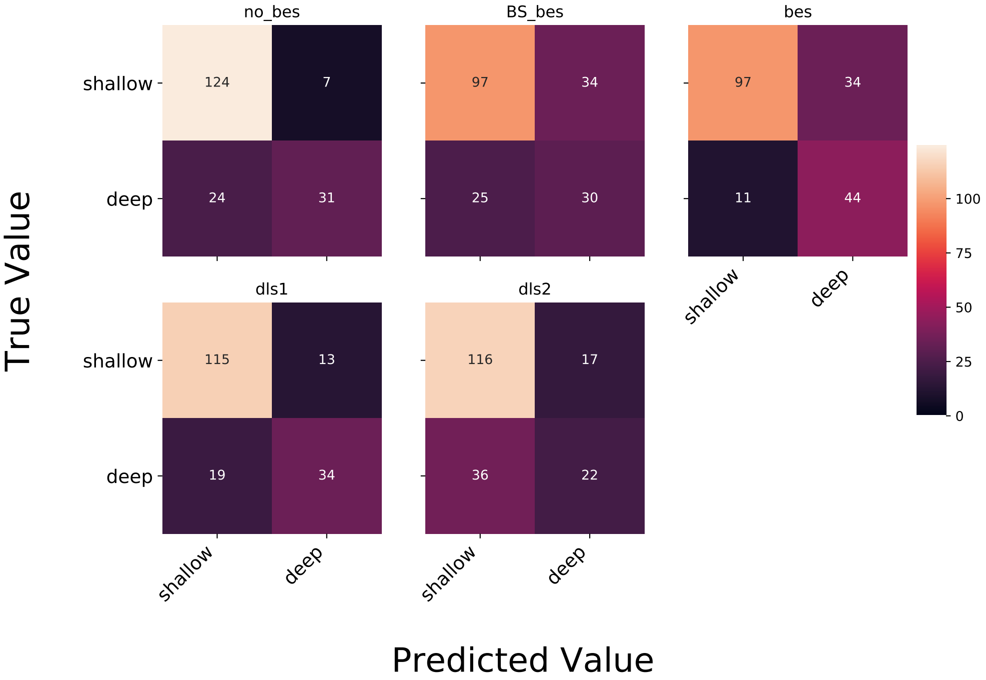

Figure 4.7: Confusion matrix for determining deep vs. shallow levels for each correction scheme. “deep” is defined as a transition levels in the window of 25% - 75% of the band gap.

energetic contribution of extra relaxation for these deep defects is not a universal first-principles correction that can be applied to semi-local functional calculations. However, for purposes of high-throughput it is possible to imagine the application of empirical shifts for cases with large site mismatch or electronic delocalization. Quantifying this amount further is a subject for future work.

Overall, any results relating to the non-gap-scaled transition level should rely on adequate Fermi level renormalization (intelligent movement of the VBM energy in Equation 4.1). Whereas, when considering transition levels as a percentage of the band gap or for considering the qualitative nature of deep vs. shallow, the best performing correction for this test set is achieved with the dls1 correction scheme.

4.4.3 Fermi Levels

The Fermi levels for the dataset were computed using the charge neutrality condition described in Section 4.3.1. The resulting errors between GGA and hybrid are shown as a scatter plot in Figure 4.8. Given a set of chemical potential values, only one Fermi level can exist for a bulk system. We choose to omit systems which have only one defect in consideration, given that a single defect is often insufficient to adequately compute the Fermi level. All formation energies and Fermi level plots are shown in Appendix F. For the case of SnO_2 we were forced to remove two defects when determining the Fermi level (the Sb_{Sn} and

F_O antisites) as a result of having negative formation energies across the entire band gap. In addition, for the dls2 correction, the ZnO system had negative formation energies across the entire gap, so there is no value for this system in the dls2 category. This results in a total of 10 systems considered across the various corrections in Figure 4.8 (9 systems for the dls2 correction).

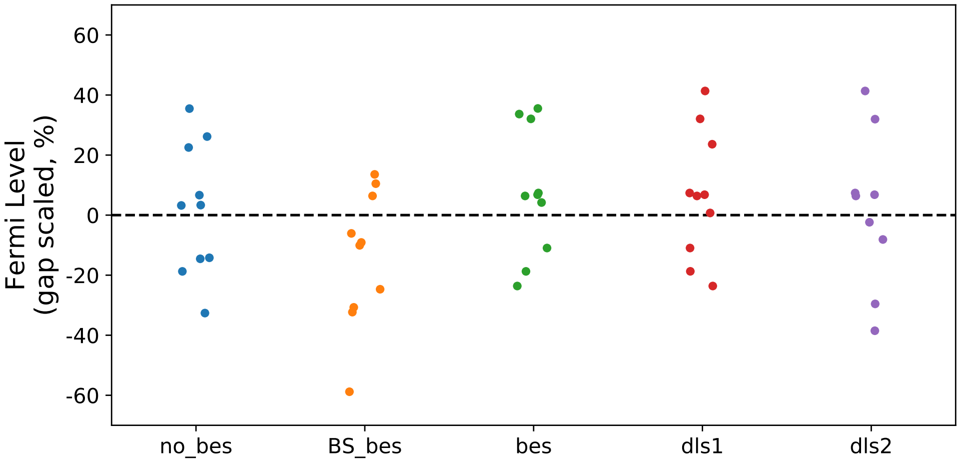

Figure 4.8: Fermi level errors (GGA − hybrid) evaluated using the charge neutrality condition described in Section 4.3.1.

The spread in errors for the 10 systems in every correction is fairly homogeneous. The exception to this trend is the BS_bes correction scheme, which skews errors in a negative fashion (underestimating with respect to the hybrid results), including the ZnO system which becomes a large outlier with -58.8% error as a result of the n-type Fermi level becoming p-type with the CBM moving upwards.

When using the Fermi level in a high-throughput study, it is useful to consider the determination of dominant carrier type. To assess the test set's performance in predicting the dominant carrier type, Figure 4.9 provides a confusion matrix for p-type, intrinsic (low carrier concentration), and n-type behavior. We define p-type values as Fermi levels less than $\frac{1}{3}$ of the gap, intrinsic Fermi levels are in the window of $(\frac{1}{3},\frac{2}{3})$ of the gap, and n-type Fermi levels are greater than $\frac{2}{3}$ of the gap.

The bes and dls1 corrections both achieve a success rate of 70%, improving over the no_bes correction's success rate of 60%. Given the buffer window of intrinsic carrier type, a prediction of n-type when the true value is p-type (or vice versa) would be considered a catastrophic failure in prediction. The only correction which produces a catastrophic failure of this nature is the BS_bes correction type, in the case of the ZnO system mentioned earlier. For all corrections except BS_bes, p-type prediction at the semi-local level is always correct, with the only failures occurring with intrinsic or n-type classification. Overall, the strong classification of the dls1 correction for p-type vs. n-type provides motivation for the use of this correction within future high-throughput studies.

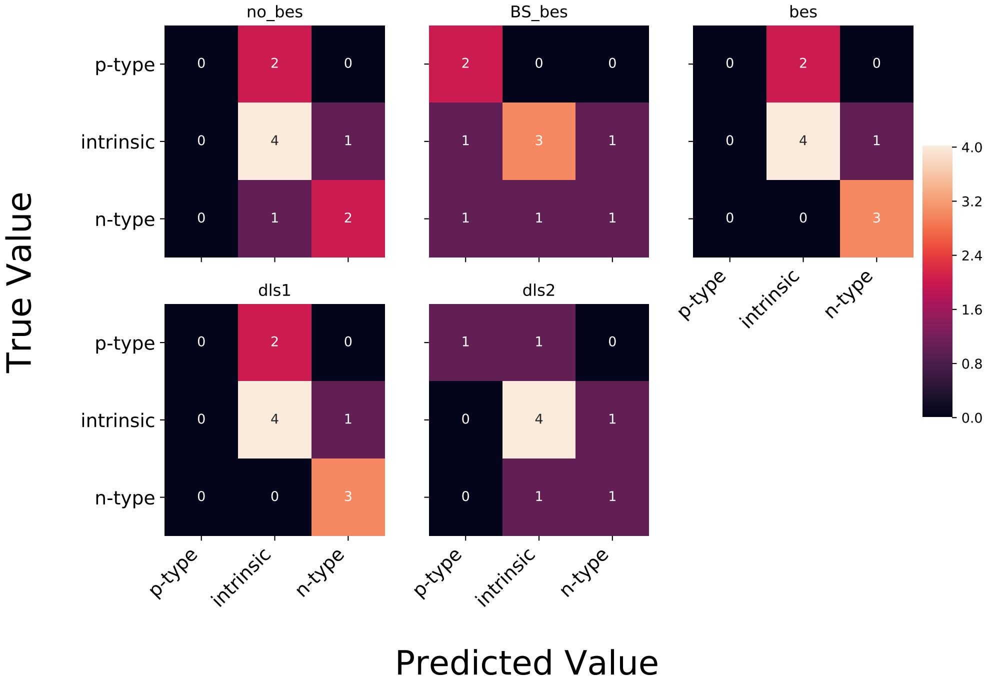

Figure 4.9: Fermi level confusion matrix, where p-type, intrinsic and n-type Fermi levels are defined in the text.

4.4.4 Formation Energies

The defect formation energy is the fundamental quantity used in Equation 4.1. Errors in this quantity are exponentially compounded when computing defect concentrations. In Figure 4.10, we display the differences in formation energies, with two choices of the Fermi level: one where it is set to the VBM and the other where it is determined by charge neutrality as determined by Equation 4.3. The error distributions for all of corrections look characteristically similar, with average absolute errors of 2.2±.2 eV, for both choices of the Fermi levels, for almost every correction. The exception is the dls1 correction, which has errors of 1.6 eV and 1.7 eV for Fermi levels at the VBM and from charge neutrality, respectively. There is no significant change between the error statistics for formation energy analysis at the VBM or the Fermi level. Overall, average hybrid formation energies tend to be lower than GGA values by about 1.5 eV. Given that errors in formation energies exponentially compound in the computation of defect concentrations, these results suggest that direct computation of defect concentrations from high-throughput should be used cautiously. The use of chemical potential corrections to improve the quantitative description of defect formation energetics is a promising direction for future work [176].

To reduce the primary outliers in formation energies within the dataset, we consider the use of the structural and electronic metrics, analyzed within Section 4.4.1, as cutoff criteria for calculations that should be flagged as problematic in the automated GGA calculations,

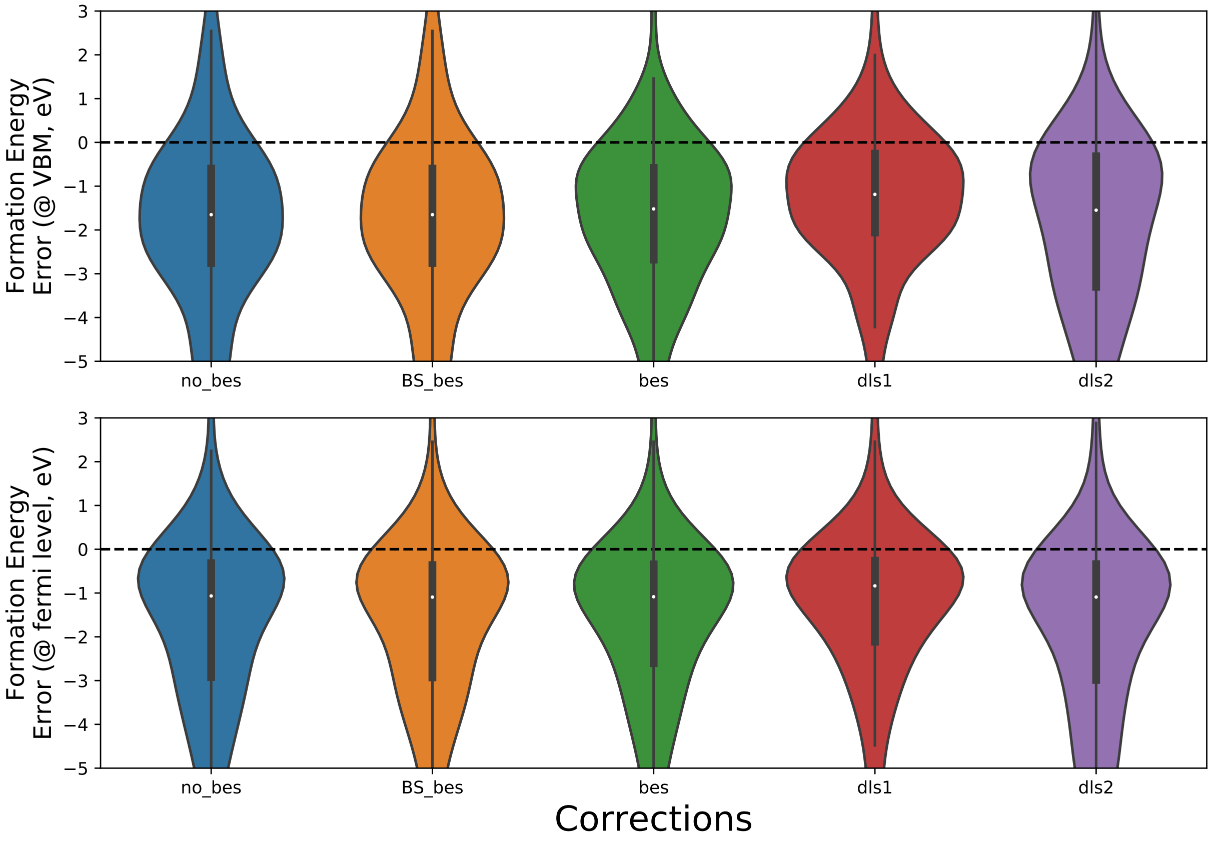

Figure 4.10: Formation energy errors (GGA – hybrid) for (A) Fermi level equal to the VBM, and (B) evaluated at the Fermi level determined by charge neutrality.

due to improper localization of the defect. Based on the metadata in our dataset, we defined a "compatible" defect calculation to have:

1. less than 2.1 free holes or electrons
2. less than 0.0001 variance in the Freysoldt sampling region for potential alignment
3. less than 0.005 variance in the Kumagai sampling region for potential alignment
4. If total relaxation amount within Wigner-Seitz radius is greater than 2 Å, then the percentage of total movement inside the Wigner-Seitz radius must be larger than 50%

Given this list of compatibility criteria, we re-plot the error relative to hybrid calculations for the compatible and not-compatible formation energies at the VBM as a scatter plot in Figure 4.11. All major outliers for the bes and dls1 corrections have been removed with the compatibility classification, with all errors now lying in the range of (-6.1 eV, +1.9 eV). In addition, the absolute mean error is improved from 1.6 eV to 1.35 eV. The skewing towards negative formation energies may be related to further relaxation of the defect structure within the hybrid calculations. Future work should consider additional compatibility criteria for screening and reducing the error in formation energies calculated.

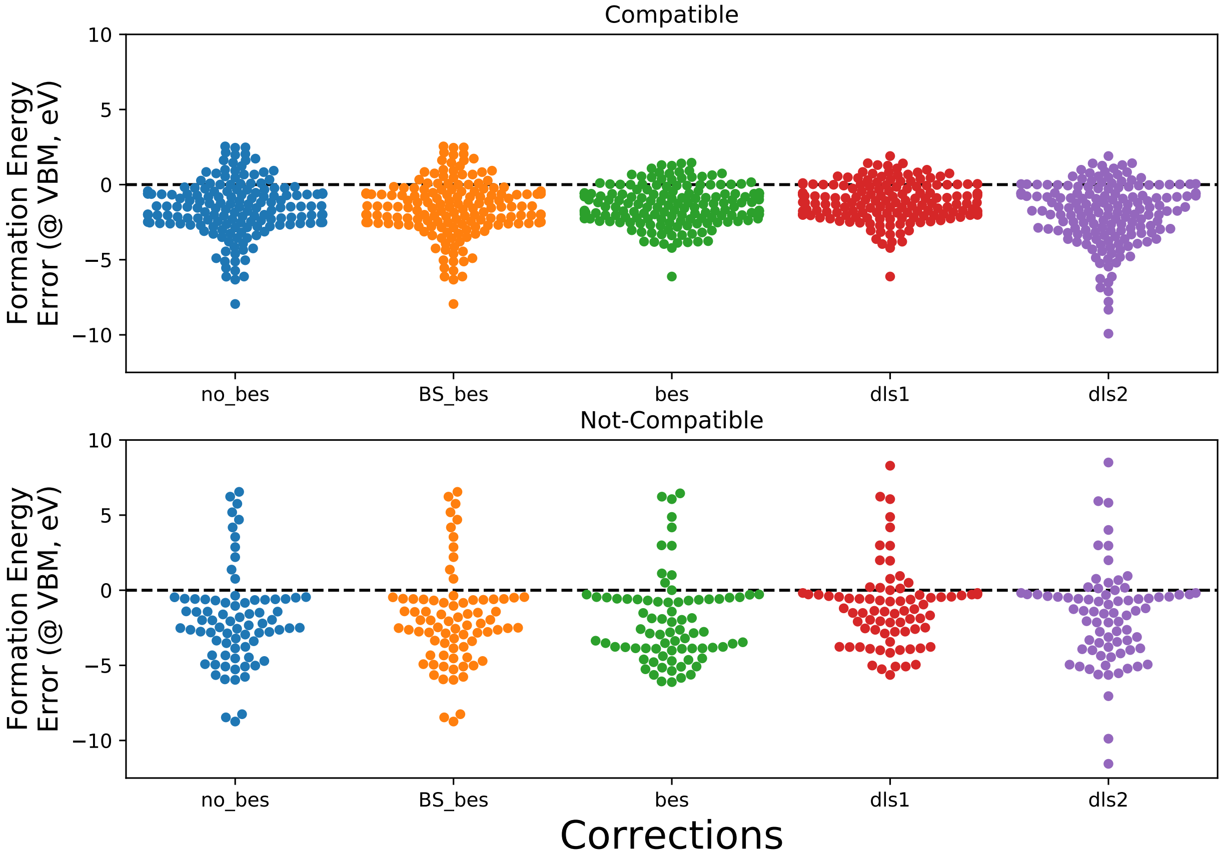

Figure 4.11: Formation energy errors (GGA – hybrid) for Fermi level equal to the VBM, broken up into compatible (top) vs. not-compatible (bottom), as discussed in the text.

When considering qualitative conclusions to be derived from formation energies, we can consider the correct ordering of stable defects and charge states from the VBM to the CBM, as computed with hybrid and GGA. For example, the convex hull of stable charged defect states (the set of lowest formation energies for all values of the Fermi energy across the gap) gives a good indication of the prominent defects of interest. For all systems considered in this study, the most stable defects at the hybrid level are within 0.1 eV of the convex hull at the semi-local level, when using the bes or dls1 correction sets. The only exceptions to this was found in the O_B substitution in B_6O, where insufficient local relaxation occurred in the GGA calculation. The general success for categorizing defects on the convex hull suggests semi-local calculations are still powerful tools for high-throughput, as such a categorization reduces the number of defects required for future calculations at higher levels of theory.

4.4.5 Dopability Limits

As mentioned in Section 4.3.1, dopability limits (the Fermi level value at which formation energies become negative) can provide an indication of the dopability of a material. The upper dopability limit would prevent the Fermi level from getting closer to the CBM (an electron killer), while the lower dopability limit would prevent the Fermi level from getting closer to the VBM (a hole killer). Errors in the gap-scaled dopability limits for 13 upper and 12 lower dopability limits are displayed in Figure 4.12. The dopability cannot be accessed for cases with negative formation energies across the entire band gap, forcing dopabilities from the ZnO system to be omitted for the dls2 correction. In addition, SnO_2, which had large errors of 225.5% and -459.2% for the upper and lower-limit dopabilities with the no_bes correction, are left outside of the y-axis limits for the no_bes correction for the sake of clarity. These large errors are a result of the previously mentioned intentional omission of negative formation energy defects, causing the GGA dopability to be determined by defects with high formation energy values.

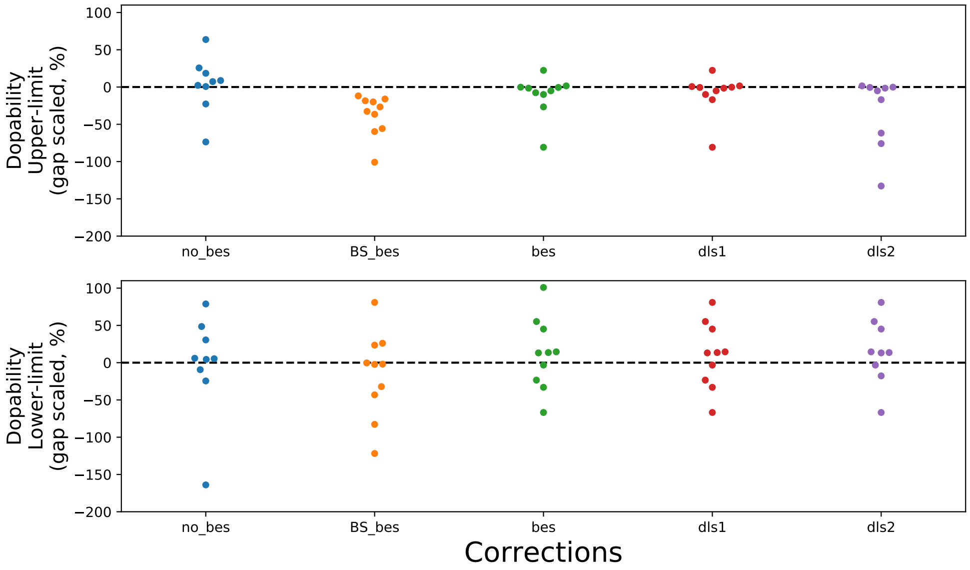

Figure 4.12: Errors in 10 upper and lower dopability limits (GGA-hybrid), as determined by the Fermi level where defect formation energies first become negative. Errors are given as a percentage of the total gap. Not shown for the no_bes correction is the SnO_2 dopability with errors of 225.5% and -459.2% for the upper and lower-limit dopabilities, respectively. The ZnO system is also not included for the dls2 correction due to formation energies being negative across the entire gap.

Overall, the bes and dls1 corrections improve the upper-limit dopability error relative to no_bes, increasing the number of systems within 10% of the correct answer from 4 to 7. The number of systems within 10% error in the lower-limit dopability was not reduced for the band edge shifting cases, but the number of outliers was reduced, with a reduced max/min window of (+ 80%,-67%) error in the dls1 correction.

The position of the hybrid dopability limit being inside or outside of the gap was a major indicator of the performance of the GGA dopability limit, with hybrid dopability values outside of the gap indicating a larger error in GGA values. A summary of average errors, broken down according to whether the dopability value is inside or outside of the gap at the hybrid level, is provided in Table 4.3. Similar to the overall trend in dopabilities, the average errors are significantly reduced for the bes and dls1 corrections in the Upper-limit, while the change is less drastic for the Lower-limit dopability errors.

Value	Count	no_bes	BS_bes	bes	dls1	dls2
Upper-limit (Hybrid Outside Gap)	7	62.6	47.5	21.8	19.4	48.8
Upper-limit (Hybrid Inside Gap)	3	3.4	15.4	1.2	1.2	1.2
Lower-limit (Hybrid Outside Gap)	3	189.5	76.2	74.3	67.6	67.6
Lower-limit (Hybrid Inside Gap)	7	37.4	26.6	20.9	20.9	17.9

Table 4.3: Average errors (eV) for upper and lower limit dopabilities, broken up according the position of the hybrid dopability value being inside or outside of the gap.

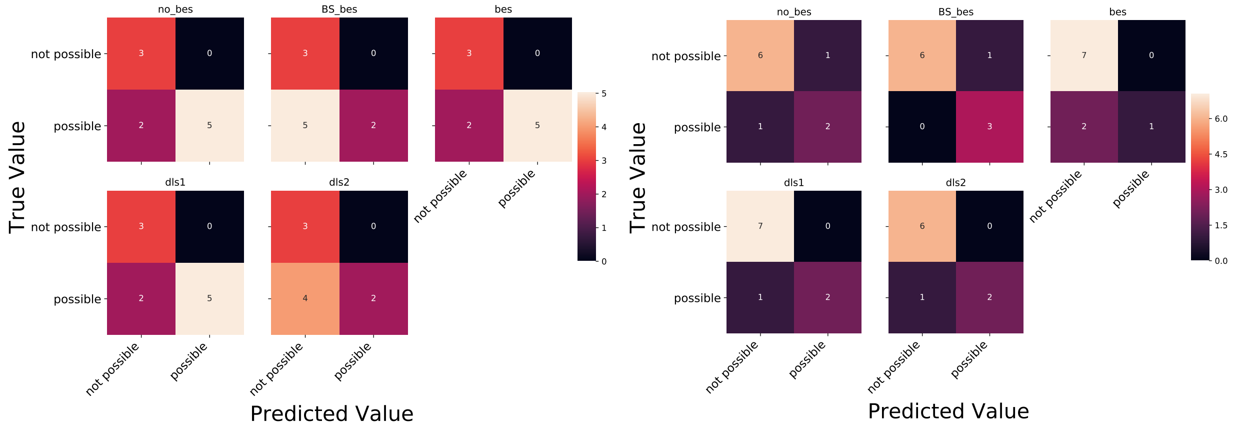

(a) Upper dopability limit (electron killer) **(b)** Lower dopability limit (hole killer)

Figure 4.13: Confusion matrix for potential doping as determined by the dopability limit. Possible p-type doping is determined from a lower dopability limit of less than 0.1 of the band gap, while possible n-type doping is determined by an upper dopability limit greater than 0.9 of the band gap.

As done in previous sections, it is worthwhile to consider the limits of qualitatively screening for dopability limits in a high-throughput manner. The purpose of dopability consideration in a high-throughput study would likely be to screen for materials which can or cannot be doped with a certain carrier type. The lower dopability limit produces hole killers which limit the possibility of p-type doping, while the upper dopability limit produces electron killers which limit the possibility for n-type doping. Using the metric that any dopability limit within 10% of the bandgap away from the band edges is a free carrier-killer, Figure 4.13 displays confusion matrices for deciding whether it is possible to dope a system n-type or p-type for the upper and lower limit dopabilities, respectively.

For the upper dopability limit, the no_bes, bes, and dls1 corrections all perform identically well with an 80% success rate. The BS_bes and dls2 corrections perform worse, with a 50% and 56% success rate, respectively. For the lower dopability limit, the BS_bes, dls1, and dls2 corrections have a 90% success rate as a result of correctly predicting the TiO_2 structure as potentially p-type dopable. The no_bes and bes corrections both achieve a lowered 80% success rate. It is interesting to note that for all band edge shifting corrections, apart from the BS_bes correction, there are no false positive predictions for possible dopability. The lack of false positives and the minimal number of false negatives provides a strong motivation for high-throughput screening studies looking for bulk materials with the potential for doping.

4.5 Insights for High-throughput Computation of Point Defects

High-throughput computation for materials discovery is a relatively nascent field which endeavors to speed up time-consuming growth and characterization experiments in efforts to discover new materials with targeted combinations of properties for a given envisioned technological application. In the context of point defect calculations in semiconductors and insulators, valuable information about the electronic carrier type and dopability of a material can be gleaned from theoretical work. Currently, no large scale high-throughput point defect studies have been performed due to the computational cost of hybrid functional approaches which are the most trusted approach for such calculations due to their reduction of band gap and self-interaction errors.

In Section 4.4 and Table 4.4, we summarize the results of calculations assessing the accuracy of computationally-efficient semi-local DFT calculations of point-defect properties, including a variety of a-posteriori corrections, compared to benchmark hybrid-functional results. Given these results, semi-local defect calculations with band edge shifting routines (bes or dls1), performed in a fully automated, high-throughput format show promise for initial screening. In particular, the results of this study suggest these methods are successful in their ability to *qualitatively* describe whether a defect is characterized by deep vs. shallow transition levels, the dominant carrier type (namely p or n), and dopability limits. With this in mind, it is possible to imagine an efficient screening procedure whereby semi-local functionals with *a-posteriori* corrections can be used to assess defects and charge states of interest within a chemical composition, and then can be followed up with more computationally intensive hybrid approaches at a higher level of accuracy. This approach will benefit from continued efforts aimed at the development of more computationally efficient implementations of hybrid functionals.

Value	Best *Quantifier*	Best *Qualifier*
Thermodynamic Transition Levels	**dls1** (0.5 ± 0.3 eV avg. absolute error)	**no_bes** (83% success rate in deep/shallow classification)
Fermi Levels	**dls1** (17% avg. absolute error with gap scaling)	**dls1** (70% success rate in p-type/intrinsic/n-type classification)
Formation Energies	**dls1 with compatibility criteria** (1.35 avg. absolute error)	**dls1** Nearly perfect defect ordering across gap
Dopability Limits	**dls1** (21 % average error with gap scaling, better with hybrid values inside of gap)	**dls1** (90% success rate in n-type/p-type doping potential, no false positives)

Table 4.4: Summary of optimal performance for quantification and qualification of defect properties analyzed in this work.

4.6 Summary

This work sought to catalog the performance of defect calculations based on semi-local DFT approaches (with *a-posteriori* corrections for band-gap errors) run in a fully automated, high-throughput framework. The accuracy of the approaches based on semi-local DFT functionals was assessed by comparing against a benchmark set of 245 hybrid calculations performed by several authors in previously published work. A set of five different correction sets for the semi-local DFT results were reviewed and considered, with a comparison of the errors of five different classes of quantities produced from the defect calculations: structural and electronic relaxation, thermodynamic transition levels, Fermi levels, formation energies, and dopability limits. With the initial established benchmark results reviewed in Table 4.4, we believe *qualitative* high-throughput screening for all the quantities outlined in this work are ripe for exploration by semi-local DFT with *a-posteriori* corrections.

Future work remains to be done on relating the *quantitative* performance of these corrections. For example, the proposed host band projection scheme shows promise as an energetic correction for delocalized defect states. Given the size of the test set, it is possible that additional classification or screening schemes for reducing error and identifying “delocalization” can be derived. Overall, we hope this study proves to be a useful first step in future large-scale studies looking to improve the potential for high-throughput DFT screening procedures to be performed on point defect properties.

CHAPTER 5

Conclusions and future work

5.1 Conclusions

Point defects influence electronic and ionic transport properties and whether an energy material will perform well in a given application. Point defect engineering is the intentional choice of growing a material in an environment which promotes beneficial defects or extrinsic dopants for the application of interest. In order to address the challenges of deep de-carbonization which are necessary to combat climate change, new materials are desired which offer higher conversion efficiencies, higher storage densities and reduced costs. In this context, Density functional theory (DFT) based methods can facilitate the process of materials discovery and design, and for such studies there is a need to account for defect properties. While point defect calculations with DFT can be hindered by finite size effects and band gap errors, qualitatively useful information for doping limits and limiting defect properties can still be gleaned from such calculations for new energy materials. This dissertation has provided tools and motivation for future work on automating point defect calculations for high-throughput materials design challenges.

Chapter 2 covered some of the essential methodology required for first principles calculations of point defects in semiconductors and insulators, and introduced the Python Charged Defect Toolkit (PyCDT) for aiding the setup, parsing, and analysis stages of performing point defect calculations in an automated fashion. We have made the software open source and have used the related publication as a user manual, with the hope that it helps improve upon the reproducibility of defect calculations in the future.

Chapter 3 outlined three different example use cases of the PyCDT codebase, for materials of interest for solar cell, thermoelectric and energy storage applications. For thermoelectrics, we have previously used PyCDT to understand doping limits in a promising new class of materials: $TmAgTe_2$ [40]. This previous study inspired work on the theoretical requirements for performing defect calculations on SnSe, leading to a new understanding of the importance of van der Waals functionals in describing the lone pair effect on Sn. For battery materials, we made use of PyCDT to understand the doping behavior of three magnesium spinel structures which have shown promise as solid-state electrolytes. We found that controlling the anion content, as well as the cooling rate, had a significant impact on the free carrier concentrations. For solar materials, we surveyed trends in Fermi level pinning of inorganic halide perovskites for a variety of chemical and structural distortions. We found that distortions of octahedral cages, which distort the local coordination, had a more pronounced effect on Fermi level pinning behavior, than the effect of rotations. In addition, for CdTe thin film solar applications we performed a small scale benchmark study against experimentally measured carrier concentrations, showing that empirical chemical potential corrections were necessary for computing the correct order of magnitude of carriers, while band gap corrections were necessary for understanding the correct partial pressure dependence of the carrier concentrations. Overall, the work done in this chapter demonstrates the power of having automated point defect analysis for expedited searches across a variety of metrics for efficient and resilient energy materials.

Chapter 4 demonstrated a systematic benchmark of automated GGA point defect calculations against “gold standard” hybrid calculations that were previously performed at a lower level of throughput. We compare first principles results at multiple levels of complexity; ranging from structural and electronic relaxation amounts of the DFT supercell, to the more complex thermodynamic transition levels and formation energies. We differentiated the *qualitative* vs. *quantitative* successes in a way which is consistent with the goals of a high-throughput materials design approach. We found that quantitative values for the Fermi level and dopability limit, when scaled by the bandgap, were significantly more trustworthy than the quantitative values for transition levels and formation energies. Qualitatively we found greater than 80% success rates for classifying a number of metrics which would be useful for high-throughput studies of energy materials. This provides strong motivation for performing future high-throughput studies with semi-local DFT used for qualitative screening of promising new energy materials.

5.2 Future Work

The work presented in this dissertation presents many opportunities for future work with automated point defect calculations. Generally speaking, a large amount of work remains to be explored with the connectivity of existing workflows within the Materials Project framework. Existing workflows can be coupled nicely with the work presented here for point defects. For example, workflows for point defects can be connected with the work done for epitaxial strain produced by Angsten *et al.* [199]. Automating the search for defects as a function of epitaxial strain in this way could prove to be a new design variable for defect engineering in functional materials prepared as epitaxial films.

The increasing computational efficiency of hybrid functional approaches are also promising for improved quantitative analysis of defects. Balancing quantitative and computational requirements in future work will likely require the use of semi-local functionals for initial screening, with follow up screening performed at the hybrid functional level. Automation capabilities for this type of work would be extremely useful to the high-throughput materials design community, and efforts to this end will be made within the atomate code base in the future.

Additional directions for methodological development exist within *canonical* ensemble definitions for defect thermodynamics. This method allows for the self consistent definition of chemical potentials with Fermi level, temperature, and stoichiometry - which could allow for more direct connections with experimental observations. While canonical ensemble approaches for defect physics have been published before [75], the final constraint required for equilibrium is commonly taken as a zeroth order low temperature expansion of the grand canonical potential. Work remains to be done to benchmark whether an extended methodology, which includes higher order terms of the grand canonical potential, could be beneficial for point defect analysis.

Finally, a number of improvements remain to be investigated for point defect workflow automation in the atomate code base. For example, avoiding defect relaxation into local minima - especially when global minima can be reached with perturbations of local coordination - would help improve automation results. Performing further analysis of large relaxation defects could allow for the identification of structural signatures which require further symmetry breaking.

Inconsistent relaxation in a DFT calculation has led to inconsistent results on defect physics in the literature, even for the same structure, with the same pseudopotential [26]. The best way to differentiate defect results is to precisely document every step of the DFT relaxation process. High-throughput infrastructure lends itself to such a process, as careful documentation and reproducibility is required for any intelligent data generation procedure. Some in the field of defect computation have been (rightly) skeptical of proceeding with point defect computation in a high-throughput format. However, it is entirely possible that the high standards set for documenting high-throughput workflows is precisely the requirement for fixing reproducibility issues that have plagued the point defect computational community for decades. In this way, intelligent engineering of automation processes for point defect calculations with DFT has the potential to remedy many problems for the entire field of point defect computation.

References

[1] C. B. Field, V. R. Barros, M. D. Mastrandrea, K. J. Mach, M.-K. Abdrabo, N. Adger, Y. A. Anokhin, O. A. Anisimov, D. J. Arent, J. Barnett, *et al.*, "Summary for policymakers," in *Climate change 2014: impacts, adaptation, and vulnerability. Part A: global and sectoral aspects. Contribution of Working Group II to the Fifth Assessment Report of the Intergovernmental Panel on Climate Change*, pp. 1–32, Cambridge University Press, 2014.

[2] O. Edenhofer, *Climate change 2014: mitigation of climate change*, vol. 3. Cambridge University Press, 2015.

[3] U. Secretariat, "Report of the conference of the parties on its twenty-first session, held in paris from 30 november to 13 december 2015," in *Addendum. Part Two: Action taken by the Conference of the Parties at its twenty-first session*, 2015.

[4] Y.-M. Chiang, W. D. Kingery, and D. P. Birnie, *Physical Ceramics: Principles for Ceramic Science and Engineering.* J. Wiley, 1997.

[5] W. F. Smith and J. Hashemi, *Foundations of Materials Science and Engineering.* Mcgraw-Hill Publishing, 2006.

[6] F. A. Kröger, *The Chemistry of Imperfect Crystals*, vol. 2. North-Holland Pub. Co., 1974.

[7] A. Zunger, "Practical doping principles," *Applied Physics Letters*, vol. 83, no. 1, 2003.

[8] C. Freysoldt, B. Grabowski, T. Hickel, J. Neugebauer, G. Kresse, A. Janotti, and C. G. Van de Walle, "First-principles calculations for point defects in solids," *Rev. Mod. Phys.*, vol. 86, pp. 253–305, Mar 2014.

[9] P. Von Dollen, S. Pimputkar, and J. S. Speck, "Let there be light—with gallium nitride: The 2014 nobel prize in physics," *Angewandte Chemie International Edition*, vol. 53, no. 51, pp. 13978–13980, 2014.

[10] M. Cardona and Y. Y. Peter, *Fundamentals of semiconductors.* Springer, 2005.

[11] M. Green, "Silicon solar cells: evolution, high-efficiency design and efficiency enhancements," *Semicond Sci Tech*, vol. 8, no. 1, p. 1, 1993.

[12] M. A. Green, "Commercial progress and challenges for photovoltaics," *Nat Energy*, vol. 1, no. 1, 2016.

[13] A. Zakutayev, C. M. Caskey, A. N. Fioretti, D. S. Ginley, J. Vidal, V. Stevanovic, E. Tea, and S. Lany, "Defect Tolerant Semiconductors for Solar Energy Conversion," *The Journal of Physical Chemistry Letters*, vol. 5, no. 7, pp. 1117–1125, 2014. PMID: 26274458.

[14] S. B. Zhang and J. E. Northrup, "Chemical potential dependence of defect formation energies in GaAs: Application to Ga self-diffusion," *Phys. Rev. Lett.*, vol. 67, pp. 2339–2342, Oct 1991.

[15] T. Sinno, E. Dornberger, W. Von Ammon, R. Brown, and F. Dupret, "Defect engineering of czochralski single-crystal silicon," *Materials Science and Engineering: R: Reports*, vol. 28, no. 5-6, pp. 149–198, 2000.

[16] D. A. Drabold and S. K. Estreicher, *Theory of defects in semiconductors*. Springer, 2007.

[17] D. Sholl and J. A. Steckel, *Density functional theory: a practical introduction*. John Wiley & Sons, 2011.

[18] S. Curtarolo, G. L. Hart, M. Nardelli, N. Mingo, S. Sanvito, and O. Levy, "The high-throughput highway to computational materials design," vol. 12, no. 3, p. 191, 2013.

[19] P. Hohenberg and W. Kohn, "Inhomogeneous electron gas," vol. 136, no. 3B, p. B864B871, 1964.

[20] W. Kohn and L. Sham, "Self-Consistent equations including exchange and correlation effects," *Phys Rev*, vol. 140, no. 4A, pp. A1133–A1138, 1965.

[21] J. P. Perdew, K. Burke, and M. Ernzerhof, "Generalized gradient approximation made simple," *Physical review letters*, vol. 77, no. 18, p. 3865, 1996.

[22] M. Ernzerhof and G. Scuseria, "Assessment of the Perdew–Burke–Ernzerhof exchange-correlation functional," *J Chem Phys*, vol. 110, no. 11, pp. 5029–5036, 1999.

[23] J. Heyd, G. Scuseria, and M. Ernzerhof, "Hybrid functionals based on a screened coulomb potential," *J Chem Phys*, vol. 118, no. 18, pp. 8207–8215, 2003.

[24] A. Krukau, O. Vydrov, A. Izmaylov, and G. Scuseria, "Influence of the exchange screening parameter on the performance of screened hybrid functionals," *J Chem Phys*, vol. 125, no. 22, p. 224106, 2006.

[25] C. G. Van de Walle and J. Neugebauer, “First-principles calculations for defects and impurities: Applications to III-nitrides,” *Journal of Applied Physics*, vol. 95, no. 8, pp. 3851–3879, 2004.

[26] S. Lany and A. Zunger, “Assessment of correction methods for the band-gap problem and for finite-size effects in supercell defect calculations: Case studies for ZnO and GaAs,” *Physical Review B*, vol. 78, no. 23, p. 235104, 2008.

[27] M. Sluydts, M. Pieters, J. Vanhellemont, V. Speybroeck, and S. Cottenier, “High-Throughput screening of extrinsic point defect properties in Si and Ge: Database and applications,” *Chem Mater*, 2016.

[28] G. Petretto and F. Bruneval, “Systematic defect donor levels in III-V and II-VI semiconductors revealed by hybrid functional density-functional theory,” *Phys. Rev. B*, vol. 92, p. 224111, December 21 2015.

[29] H. Peng, D. O. Scanlon, V. Stevanovic, J. Vidal, G. W. Watson, and S. Lany, “Convergence of density and hybrid functional defect calculations for compound semiconductors,” *Physical Review B*, vol. 88, no. 11, p. 115201, 2013.

[30] J. L. Lyons and C. G. de Walle, “Computationally predicted energies and properties of defects in GaN,” *Npj Comput Mater*, vol. 3, no. 1, p. 12, 2017.

[31] M. Du, “Density functional calculations of native defects in $CH_3NH_3PbI_3$: Effects of Spin–Orbit coupling and Self-Interaction error,” vol. 6, no. 8, pp. 1461–1466, 2015.

[32] G. Hautier, “Finding the needle in the haystack: Materials discovery and design through computational ab initio high-throughput screening,” *Comp Mater Sci*, vol. 163, no. Nat. Mater. 12 2013, pp. 108–116, 2019.

[33] K. Alberi, M. Nardelli, A. Zakutayev, L. Mitas, S. Curtarolo, A. Jain, M. Fornari, N. Marzari, I. Takeuchi, M. L. Green, M. Kanatzidis, M. F. Toney, S. Butenko, B. Meredig, S. Lany, U. Kattner, A. Davydov, E. S. Toberer, V. Stevanovic, A. Walsh, N. Park, A. Alán, D. P. Tabor, J. Nelson, J. Murphy, A. Setlur, J. Gregoire, H. Li, R. Xiao, A. Ludwig, L. W. Martin, A. M. Rappe, S. Wei, and J. Perkins, “The 2019 materials by design roadmap,” vol. 52, no. 1, p. 013001, 2018.

[34] S. Chakraborty, W. Xie, N. Mathews, M. Sherburne, R. Ahuja, M. Asta, and S. G. Mhaisalkar, “Rational design - a High-Throughput computational screening and experimental validation methodology for lead-free and emergent hybrid perovskites,” *Acs Energy Lett*, 2017.

[35] W. Rachel, D. Broberg, A. Faghaninia, A. Jain, S. Dwaraknath, and K. Persson, “Assessing High-Throughput descriptors for prediction of transparent conductors,” *Chem Mater*, 2018.

[36] A. Jain, S. P. Ong, G. Hautier, W. Chen, W. D. Richards, S. Dacek, S. Cholia, D. Gunter, D. Skinner, G. Ceder, and K. a. Persson, “The Materials Project: A materials genome approach to accelerating materials innovation,” *APL Materials*, vol. 1, no. 1, p. 011002, 2013.

[37] L. Lang, J. Yang, H. Liu, H. Xiang, and X. Gong, “First-principles study on the electronic and optical properties of cubic ABX_3 halide perovskites,” vol. 378, no. 3, pp. 290–293, 2014.

[38] R. E. Brandt, V. Stevanović, D. S. Ginley, and T. Buonassisi, “Identifying defect-tolerant semiconductors with high minority-carrier lifetimes: beyond hybrid lead halide perovskites,” *MRS Commun*, vol. 5, no. 2, pp. 265–275, 2015.

[39] S. Körbel, M. A. Marques, and S. Botti, “Stability and electronic properties of new inorganic perovskites from high-throughput ab initio calculations,” *J Mater Chem C*, vol. 4, no. 15, pp. 3157–3167, 2016.

[40] H. Zhu, G. Hautier, U. Aydemir, Z. M. Gibbs, G. Li, S. Bajaj, J.-H. Pohls, D. Broberg, W. Chen, A. Jain, M. A. White, M. Asta, G. J. Snyder, K. Persson, and G. Ceder, “Computational and experimental investigation of $TmAgTe_2$ and XYZ_2 compounds, a new group of thermoelectric materials identified by first-principles high-throughput screening,” *J. Mater. Chem. C*, vol. 3, pp. 10554–10565, 2015.

[41] W. D. Callister, Jr., *Materials Science and Engineering: an Introduction.* New York, NY, USA: John Wiley & Sons, Inc., 7 ed., 2007.

[42] H. Queisser, J. Spaeth, and H. Overhof, *Point Defects in Semiconductors and Insulators: Determination of Atomic and Electronic Structure from Paramagnetic Hyperfine Interactions.* Springer Series in Materials Science, Springer Berlin Heidelberg, 2013.

[43] M. McCluskey and E. Haller, *Dopants and Defects in Semiconductors.* CRC Press, 2012.

[44] P. Rodnyi, *Physical Processes in Inorganic Scintillators.* Laser & Optical Science & Technology, Taylor & Francis, 1997.

[45] E. G. Seebauer and M. C. Kratzer, “Charged point defects in semiconductors,” *Mater. Sci. Eng., R*, vol. 55, pp. 57–149, December 15 2006.

[46] P. Dorenbos, “Scintillation mechanisms in Ce^{3+} doped halide scintillators,” *physica status solidi (a)*, vol. 202, no. 2, pp. 195–200, 2005.

[47] A. Chaudhry, R. Boutchko, S. Chourou, G. Zhang, N. Grønbech-Jensen, and A. Canning, “First-principles study of luminescence in Eu^{2+}-doped inorganic scintillators,” *Phys. Rev. B*, vol. 89, p. 155105, Apr 2014.

[48] S. Lany and A. Zunger, "Dopability, Intrinsic Conductivity, and Nonstoichiometry of Transparent Conducting Oxides," *Phys. Rev. Lett.*, vol. 98, p. 045501, Jan 2007.

[49] D. O. Scanlon and G. W. Watson, "Conductivity Limits in $CuAlO_2$ from Screened-Hybrid Density Functional Theory," *The Journal of Physical Chemistry Letters*, vol. 1, no. 21, pp. 3195–3199, 2010.

[50] J. B. Varley, V. Lordi, A. Miglio, and G. Hautier, "Electronic structure and defect properties of B_6O from hybrid functional and many-body perturbation theory calculations: A possible ambipolar transparent conductor," *Phys. Rev. B*, vol. 90, p. 045205, Jul 2014.

[51] A. Walsh, D. O. Scanlon, S. Chen, X. G. Gong, and S.-H. Wei, "Self-regulation mechanism for charged point defects in hybrid halide perovskites," *Angewandte Chemie*, vol. 127, no. 6, pp. 1811–1814, 2015.

[52] G. S. Pomrehn, A. Zevalkink, W. G. Zeier, A. van de Walle, and G. J. Snyder, "Defect-Controlled Electronic Properties in AZn_2Sb_2 Zintl Phases," *Angewandte Chemie International Edition*, vol. 53, no. 13, pp. 3422–3426, 2014.

[53] S. Lany and A. Zunger, "Accurate prediction of defect properties in density functional supercell calculations," *Modelling and Simulation in Materials Science and Engineering*, vol. 17, no. 8, p. 084002, 2009.

[54] M. Giantomassi, M. Stankovski, R. Shaltaf, M. Grüning, F. Bruneval, P. Rinke, and G.-M. Rignanese, "Electronic properties of interfaces and defects from many-body perturbation theory: Recent developments and applications," *physica status solidi (b)*, vol. 248, no. 2, pp. 275–289, 2011.

[55] J. E. Northrup, M. S. Hybertsen, and S. G. Louie, "Theory of quasiparticle energies in alkali metals," *Phys. Rev. Lett.*, vol. 59, pp. 819–822, Aug 1987.

[56] J.-L. Li, G.-M. Rignanese, E. K. Chang, X. Blase, and S. G. Louie, "GW study of the metal-insulator transition of bcc hydrogen," *Phys. Rev. B*, vol. 66, p. 035102, Jul 2002.

[57] A. I. Liechtenstein, V. I. Anisimov, and J. Zaanen, "Density-functional theory and strong interactions: Orbital ordering in mott-hubbard insulators," *Phys. Rev. B*, vol. 52, pp. R5467–R5470, Aug 1995.

[58] E. Finazzi, C. Di Valentin, G. Pacchioni, and A. Selloni, "Excess electron states in reduced bulk anatase TiO_2: comparison of standard GGA, GGA+U, and hybrid DFT calculations.," *The Journal of Chemical Physics*, vol. 129, no. 15, pp. 154113–154113, 2008.

[59] J.-C. Wu, J. Zheng, P. Wu, and R. Xu, "Study of native defects and transition-metal (Mn, Fe, Co, and Ni) doping in a zinc-blende CdS photocatalyst by DFT and hybrid DFT calculations," *J. Phys. Chem. C*, vol. 115, pp. 5675–5682, April 7 2011.

[60] C. W. M. Castleton, A. Höglund, and S. Mirbt, "Density functional theory calculations of defect energies using supercells," *Modelling and Simulation in Materials Science and Engineering*, vol. 17, no. 8, p. 084003, 2009.

[61] A. Goyal, P. Gorai, H. Peng, S. Lany, and V. Stevanović, "A computational framework for automation of point defect calculations," *Computational Materials Science*, vol. 130, pp. 1–9, 2017.

[62] E. Péan, J. Vidal, S. Jobic, and C. Latouche, "Presentation of the PyDEF post-treatment python software to compute publishable charts for defect energy formation," *Chemical Physics Letters*, 2017.

[63] K. Yim, J. Lee, D. Lee, M. Lee, E. Cho, H. Lee, H. Nahm, and S. Han, "Property database for single-element doping in ZnO obtained by automated first-principles calculations.," *Scientific Reports*, vol. 7, pp. 40907–40907, 2017.

[64] A. Jain, S. P. Ong, G. Hautier, W. Chen, W. D. Richards, S. Dacek, S. Cholia, D. Gunter, D. Skinner, G. Ceder, *et al.*, "Commentary: The materials project: A materials genome approach to accelerating materials innovation," *APL Materials*, vol. 1, no. 1, p. 011002, 2013.

[65] C. Freysoldt, J. Neugebauer, and C. G. Van de Walle, "Fully *Ab Initio* Finite-Size Corrections for Charged-Defect Supercell Calculations," *Phys. Rev. Lett.*, vol. 102, p. 016402, Jan 2009.

[66] Y. Kumagai and F. Oba, "Electrostatics-based finite-size corrections for first-principles point defect calculations," *Phys. Rev. B*, vol. 89, p. 195205, May 2014.

[67] N. E. R. Zimmermann, A. Jain, and M. Haranczyk, "Structure motif assessment based on order parameters for automatic motif identification, interstitial finding, and diffusion path characterization." in preparation, 2017.

[68] G. Kresse and J. Hafner, "Ab initio molecular dynamics for liquid metals," *Physical Review B*, vol. 47, no. 1, p. 558, 1993.

[69] G. Kresse and J. Hafner, "Ab initio molecular-dynamics simulation of the liquid-metal–amorphous-semiconductor transition in germanium," *Physical Review B*, vol. 49, no. 20, p. 14251, 1994.

[70] W. D. Richards, L. J. Miara, Y. Wang, J. C. Kim, and G. Ceder, "Interface stability in solid-state batteries," *Chemistry of Materials*, vol. 28, no. 1, pp. 266–273, 2015.

[71] J. Sun, R. C. Remsing, Y. Zhang, Z. Sun, A. Ruzsinszky, H. Peng, Z. Yang, A. Paul, U. Waghmare, X. Wu, *et al.*, "Accurate first-principles structures and energies of diversely bonded systems from an efficient density functional," *Nature Chemistry*, vol. 8, no. 9, pp. 831–836, 2016.

[72] B. G. Janesko, T. M. Henderson, and G. E. Scuseria, "Screened hybrid density functionals for solid-state chemistry and physics," *Phys. Chem. Chem. Phys.*, vol. 11, pp. 443–454, 2009.

[73] H. A. Tahini, A. Chroneos, S. T. Murphy, U. Schwingenschlögl, and R. W. Grimes, "Vacancies and defect levels in III-V semiconductors," *J. Appl. Phys.*, vol. 114, no. 6, 2013.

[74] M. G. Medvedev, I. S. Bushmarinov, J. Sun, J. P. Perdew, and K. A. Lyssenko, "Density functional theory is straying from the path toward the exact functional," *Science*, vol. 355, no. 6320, pp. 49–52, 2017.

[75] J. W. Doak, K. J. Michel, and C. Wolverton, "Determining dilute-limit solvus boundaries in multi-component systems using defect energetics: Na in PbTe and PbS," *Journal of Materials Chemistry C*, vol. 3, no. 40, pp. 10630–10649, 2015.

[76] S. P. Ong, W. D. Richards, A. Jain, G. Hautier, M. Kocher, S. Cholia, D. Gunter, V. L. Chevrier, K. A. Persson, and G. Ceder, "Python materials genomics (pymatgen): A robust, open-source python library for materials analysis," *Computational Materials Science*, vol. 68, pp. 314–319, 2013.

[77] A. Jain, G. Hautier, S. P. Ong, C. J. Moore, C. C. Fischer, K. A. Persson, and G. Ceder, "Formation enthalpies by mixing GGA and GGA + U calculations," *Phys. Rev. B*, vol. 84, p. 045115, Jul 2011.

[78] B. Medasani, M. L. Sushko, K. M. Rosso, D. K. Schreiber, and S. M. Bruemmer, "Vacancies and vacancy-mediated self diffusion in Cr_2O_3: A first-principles study," *The Journal of Physical Chemistry C*, vol. 121, no. 3, pp. 1817–1831, 2017.

[79] H. A. Tahini, X. Tan, U. Schwingenschlögl, and S. C. Smith, "Formation and migration of oxygen vacancies in $SrCoO_3$ and their effect on oxygen evolution reactions," *ACS Catalysis*, vol. 6, no. 8, pp. 5565–5570, 2016.

[80] P. Ágoston, K. Albe, R. M. Nieminen, and M. J. Puska, "Intrinsic n-type behavior in transparent conducting oxides: A comparative hybrid-functional study of In_2O_3, SnO_2, and ZnO," *Physical review letters*, vol. 103, no. 24, p. 245501, 2009.

[81] G. Hautier, S. P. Ong, A. Jain, C. J. Moore, and G. Ceder, "Accuracy of density functional theory in predicting formation energies of ternary oxides from binary oxides and its implication on phase stability," *Phys. Rev. B*, vol. 85, p. 155208, Apr 2012.

[82] W. Sun, S. T. Dacek, S. P. Ong, G. Hautier, A. Jain, W. D. Richards, A. C. Gamst, K. A. Persson, and G. Ceder, “The thermodynamic scale of inorganic crystalline metastability,” *Science Advances*, vol. 2, no. 11, 2016.

[83] S. E. Taylor and F. Bruneval, “Understanding and correcting the spurious interactions in charged supercells,” *Physical Review B*, vol. 84, no. 7, p. 075155, 2011.

[84] C. Freysoldt, J. Neugebauer, and C. G. Van de Walle, “Electrostatic interactions between charged defects in supercells,” *physica status solidi (b)*, vol. 248, no. 5, pp. 1067–1076, 2011.

[85] G. Makov and M. C. Payne, “Periodic boundary conditions in *ab initio* calculations,” *Phys. Rev. B*, vol. 51, pp. 4014–4022, Feb 1995.

[86] H.-P. Komsa, T. T. Rantala, and A. Pasquarello, “Finite-size supercell correction schemes for charged defect calculations,” *Phys. Rev. B*, vol. 86, p. 045112, Jul 2012.

[87] S. Boeck, C. Freysoldt, A. Dick, L. Ismer, and J. Neugebauer, “The object-oriented DFT program library S/PHI/nX,” *Computer Physics Communications*, vol. 182, no. 3, pp. 543 – 554, 2011.

[88] P. Deák, B. Aradi, M. Kaviani, T. Frauenheim, and A. Gali, “Formation of NV centers in diamond: a theoretical study based on calculated transitions and migration of nitrogen and vacancy related defects,” *Phys. Rev. B*, vol. 89, p. 075203, February 4 2014.

[89] A. Chroneos, H. A. Tahini, U. Schwingenschlögl, and R. W. Grimes, “Antisites in III-V semiconductors: Density functional theory calculations,” *J. Appl. Phys.*, vol. 116, July 14 2014.

[90] F. Corsetti and A. A. Mostofi, “System-size convergence of point defect properties: the case of the silicon vacancy,” *Phys. Rev. B*, vol. 84, p. 035209, July 29 2011.

[91] P. Li, S. Deng, L. Zhang, G. Liu, and J. Yu, “Native point defects in ZnS: first-principles studies based on LDA, LDA + U and an extrapolation scheme,” *Chem. Phys. Lett.*, vol. 531, pp. 75–79, April 2 2012.

[92] L. S. dos Santos, W. G. Schmidt, and E. Rauls, “Group-VII point defects in ZnSe,” *Phys. Rev. B*, vol. 84, p. 115201, September 2 2011.

[93] J. Neugebauer and C. G. Van de Walle, “Atomic geometry and electronic structure of native defects in GaN,” *Phys. Rev. B*, vol. 50, pp. 8067–8070, September 15 1994.

[94] M. O’Keeffe and N. E. Brese, “Atom sizes and bond lengths in molecules and crystals,” *J. Am. Chem. Soc.*, vol. 113, pp. 3226–3229, April 24 1991.

[95] A. Gibson, R. Haydock, and J. P. LaFemina, "Stability of vacancy defects in MgO: The role of charge neutrality," *Phys. Rev. B*, vol. 50, pp. 2582–2592, Jul 1994.

[96] B. Peters, "Competing nucleation pathways in a mixture of oppositely charged colloids: out-of-equilibrium nucleation revisited," *J. Chem. Phys.*, vol. 131, p. 244103, DEC 28 2009.

[97] N. E. R. Zimmermann, B. Vorselaars, D. Quigley, and B. Peters, "Nucleation of NaCl from aqueous solution: critical sizes, ion-attachment kinetics, and rates," *J. Am. Chem. Soc.*, vol. 137, pp. 13352–13361, October 21 2015.

[98] S. Decoster, B. De Vries, U. Wahl, J. G. Correia, and A. Vantomme, "Experimental evidence of tetrahedral interstitial and bond-centered Er in Ge," *Appl. Phys. Lett.*, vol. 93, p. 141907, October 6 2008.

[99] S. Decoster, S. Cottenier, B. De Vries, H. Emmerich, U. Wahl, J. G. Correia, and A. Vantomme, "Transition metal impurities on the bond-centered site in germanium," *Phys. Rev. Lett.*, vol. 102, p. 065502, February 13 2009.

[100] S. Decoster, B. De Vries, U. Wahl, J. G. Correia, and A. Vantomme, "Lattice location study of implanted In in Ge," *J. Appl. Phys.*, vol. 105, p. 083522, April 15 2009.

[101] S. Decoster, S. Cottenier, U. Wahl, J. G. Correia, and A. Vantomme, "Lattice location study of ion implanted Sn and Sn-related defects in Ge," *Phys. Rev. B*, vol. 81, p. 155204, April 15 2010.

[102] S. Decoster, S. Cottenier, U. Wahl, J. G. Correia, L. M. C. Pereira, C. Lacasta, M. R. Da Silva, and A. Vantomme, "Diluted manganese on the bond-centered site in germanium," *Appl. Phys. Lett.*, vol. 97, p. 151914, October 11 2010.

[103] L. M. C. Pereira, U. Wahl, S. Decoster, J. G. Correia, M. R. da Silva, A. Vantomme, and J. P. Araújo, "Direct identification of interstitial Mn in heavily p-type doped GaAs and evidence of its high thermal stability," *Appl. Phys. Lett.*, vol. 98, p. 201905, May 16 2011.

[104] L. M. C. Pereira, U. Wahl, S. Decoster, J. G. Correia, L. M. Amorim, M. R. da Silva, J. P. Araujo, and A. Vantomme, "Stability and diffusion of interstitial and substitutional Mn in GaAs of different doping types," *Phys. Rev. B*, vol. 86, p. 125206, September 24 2012.

[105] S. Decoster, U. Wahl, S. Cottenier, J. G. Correia, T. Mendonça, L. M. Amorim, L. M. C. Pereira, and A. Vantomme, "Lattice position and thermal stability of diluted As in Ge," *J. Appl. Phys.*, vol. 111, p. 053528, March 1 2012.

[106] L. M. Amorim, U. Wahl, L. M. C. Pereira, S. Decoster, D. J. Silva, M. R. da Silva, A. Gottberg, J. G. Correia, K. Temst, and A. Vantomme, "Precise lattice location of substitutional and interstitial Mg in AlN," *Appl. Phys. Lett.*, vol. 103, p. 262102, December 23 2013.

[107] D. J. Silva, U. Wahl, J. G. Correia, L. M. C. Pereira, L. M. Amorim, M. R. da Silva, E. Bosne, and J. P. Araújo, "Lattice location and thermal stability of implanted nickel in silicon studied by on-line emission channeling," *J. Appl. Phys.*, vol. 115, p. 023504, January 14 2014.

[108] H. Hofsäss and G. Lindner, "Emission channeling and blocking," *Phys. Rep. (Rev. Sec. Phys. Lett.)*, vol. 201, pp. 121–183, March 1991.

[109] M. R. Silva, U. Wahl, J. G. Correia, L. M. Amorim, and L. M. C. Pereira, "A versatile apparatus for on-line emission channeling experiments," *Rev. Sci. Instrum.*, vol. 84, p. 073506, July 2013.

[110] Z. Rong, R. Malik, P. Canepa, G. S. Gautam, M. Liu, A. Jain, K. Persson, and G. Ceder, "Materials design rules for multivalent ion mobility in intercalation structures," *Chem. Mater.*, vol. 27, pp. 6016–6021, September 8 2015.

[111] Y. Wang, W. D. Richards, S. P. Ong, L. J. Miara, J. C. Kim, Y. Mo, and G. Ceder, "Design principles for solid-state lithium superionic conductors," *Nat. Mater.*, vol. 14, pp. 1026–1031, October 2015.

[112] A. De Vita, *The energetics of defects and impurities in metals and ionic materials from first principles*. PhD thesis, Keele University, Aug 1992.

[113] J. D. Hunter, "Matplotlib: A 2D graphics environment," *Computing In Science & Engineering*, vol. 9, no. 3, pp. 90–95, 2007.

[114] "Numpy developers, http://numpy.org/."

[115] A. Jain, S. P. Ong, W. Chen, B. Medasani, X. Qu, M. Kocher, M. Brafman, G. Petretto, G.-M. Rignanese, G. Hautier, D. Gunter, and K. A. Persson, "Fireworks: a dynamic workflow system designed for high-throughput applications," *Concurrency and Computation: Practice and Experience*, vol. 27, no. 17, pp. 5037–5059, 2015. CPE-14-0307.R2.

[116] P. A. Schultz and O. A. von Lilienfeld, "Simple intrinsic defects in gallium arsenide," *Modelling and Simulation in Materials Science and Engineering*, vol. 17, no. 8, p. 084007, 2009.

[117] F. El-Mellouhi and N. Mousseau, "Self-vacancies in gallium arsenide: An *ab initio* calculation," *Phys. Rev. B*, vol. 71, p. 125207, Mar 2005.

[118] J. T. Schick, C. G. Morgan, and P. Papoulias, "First-principles study of As interstitials in GaAs: Convergence, relaxation, and formation energy," *Phys. Rev. B*, vol. 66, p. 195302, Nov 2002.

[119] H.-P. Komsa and A. Pasquarello, "Identification of defect levels at As/oxide interfaces through hybrid functionals," *Microelectronic Engineering*, vol. 88, no. 7, pp. 1436 – 1439, 2011. Proceedings of the 17th Biennial International Insulating Films on Semiconductor Conference17th Biennial International Insulating Films on Semiconductor Conference.

[120] J. E. Northrup and S. B. Zhang, "Energetics of the As vacancy in GaAs: The stability of the 3+ charge state," *Phys. Rev. B*, vol. 50, pp. 4962–4964, Aug 1994.

[121] H.-P. Komsa and A. Pasquarello, "Assessing the accuracy of hybrid functionals in the determination of defect levels: Application to the As antisite in GaAs," *Phys. Rev. B*, vol. 84, p. 075207, Aug 2011.

[122] K. Lejaeghere, G. Bihlmayer, T. Bjoerkman, P. Blaha, S. Bluegel, V. Blum, D. Caliste, I. E. Castelli, S. J. Clark, A. Dal Corso, S. de Gironcoli, T. Deutsch, J. K. Dewhurst, I. Di Marco, C. Draxl, M. Dulak, O. Eriksson, J. A. Flores-Livas, K. F. Garrity, L. Genovese, P. Giannozzi, M. Giantomassi, S. Goedecker, X. Gonze, O. Granaes, E. K. U. Gross, A. Gulans, F. Gygi, D. R. Hamann, P. J. Hasnip, N. A. W. Holzwarth, D. Iusan, D. B. Jochym, F. Jollet, D. Jones, G. Kresse, K. Koepernik, E. Kuecuekbenli, Y. O. Kvashnin, I. L. M. Locht, S. Lubeck, M. Marsman, N. Marzari, U. Nitzsche, L. Nordstrom, T. Ozaki, L. Paulatto, C. J. Pickard, W. Poelmans, M. I. J. Probert, K. Refson, M. Richter, G.-M. Rignanese, S. Saha, M. Scheffler, M. Schlipf, K. Schwarz, S. Sharma, F. Tavazza, P. Thunstroem, A. Tkatchenko, M. Torrent, D. Vanderbilt, M. J. van Setten, V. Van Speybroeck, J. M. Wills, J. R. Yates, G.-X. Zhang, and S. Cottenier, "Reproducibility in density functional theory calculations of solids," *Science*, vol. 351, pp. 1415–U81, March 25 2016.

[123] G. J. Snyder and E. S. Toberer, "Complex thermoelectric materials," in *Materials For Sustainable Energy: A Collection of Peer-Reviewed Research and Review Articles from Nature Publishing Group*, pp. 101–110, World Scientific, 2011.

[124] B. Orr, A. Akbarzadeh, M. Mochizuki, and R. Singh, "A review of car waste heat recovery systems utilising thermoelectric generators and heat pipes," *Applied Thermal Engineering*, vol. 101, pp. 490–495, 2016.

[125] Y. Pei, H. Wang, and G. Snyder, "Band engineering of thermoelectric materials," *Adv Mater*, vol. 24, no. 46, pp. 6125–6135, 2012.

[126] U. Aydemir, J. Pöhls, H. Zhu, G. Hautier, S. Bajaj, Z. Gibbs, W. Chen, G. Li, S. Ohno, D. Broberg, S. Kang, M. Asta, G. Ceder, M. White, K. Persson, A. Jain, and G. Snyder,

"$YCuTe_2$: a member of a new class of thermoelectric materials with $CuTe_4$-based layered structure," *J Mater Chem A*, vol. 4, no. 7, pp. 2461–2472, 2016.

[127] L. Zhao, S. Lo, Y. Zhang, H. Sun, G. Tan, C. Uher, C. Wolverton, V. P. Dravid, and M. G. Kanatzidis, "Ultralow thermal conductivity and high thermoelectric figure of merit in SnSe crystals," *Nature*, vol. 508, no. 7496, p. 373, 2014.

[128] L. Zhao, G. Tan, S. Hao, J. He, Y. Pei, H. Chi, H. Wang, S. Gong, H. Xu, V. P. Dravid, C. Uher, J. G. Snyder, C. Wolverton, and M. G. Kanatzidis, "Ultrahigh power factor and thermoelectric performance in hole-doped single-crystal SnSe," *Science*, vol. 351, no. 6269, pp. 141–144, 2016.

[129] A. Khan, I. Khan, I. Ahmad, and Z. Ali, "Thermoelectric studies of IV–VI semiconductors for renewable energy resources," *Mat Sci Semicon Proc*, vol. 48, pp. 85–94, 2016.

[130] R. Guo, X. Wang, Y. Kuang, and B. Huang, "First-principles study of anisotropic thermoelectric transport properties of IV-VI semiconductor compounds SnSe and SnS," *Phys Rev B*, vol. 92, no. 11, p. 115202, 2015.

[131] L. Makinistian and E. Albanesi, "On the band gap location and core spectra of orthorhombic IV–VI compounds SnS and SnSe," *Phys Status Solidi B*, vol. 246, no. 1, pp. 183–191, 2009.

[132] T. Kerber, M. Sierka, and J. Sauer, "Application of semiempirical long-range dispersion corrections to periodic systems in density functional theory," *Journal of computational chemistry*, vol. 29, no. 13, pp. 2088–2097, 2008.

[133] T. Bučko, S. Lebègue, J. Hafner, and J. G. Ángyán, "Improved density dependent correction for the description of london dispersion forces," *Journal of chemical theory and computation*, vol. 9, no. 10, pp. 4293–4299, 2013.

[134] T. Björkman, "Testing several recent van der waals density functionals for layered structures," *J Chem Phys*, vol. 141, no. 7, p. 074708, 2014.

[135] T. Chattopahyay, J. Pannetier, and H. G. von Schnering, "Neutron diffraction study of the structural phase transition in SnS and SnSe," vol. 5, no. 4, pp. 53–54, 0.

[136] D. Broberg, B. Medasani, N. Zimmermann, G. Yu, A. Canning, M. Haranczyk, M. Asta, and G. Hautier, "PyCDT: a python toolkit for modeling point defects in semiconductors and insulators," *Comput Phys Commun*, vol. 226, pp. 165–179, 2018.

[137] Y. Huang, C. Wang, X. Chen, D. Zhou, J. Du, S. Wang, and L. Ning, "First-principles study on intrinsic defects of SnSe," *Rsc Adv*, vol. 7, no. 44, pp. 27612–27618, 2017.

[138] A. Dewandre, O. Hellman, S. Bhattacharya, A. H. Romero, G. K. Madsen, and M. J. Verstraete, “Two-Step phase transition in SnSe and the origins of its high power factor from first principles,” *Phys Rev Lett*, vol. 117, no. 27, p. 276601, 2016.

[139] A. Walsh and G. W. Watson, “Influence of the anion on lone pair formation in Sn(II) monochalcogenides: A DFT study,” *J Phys Chem B*, vol. 109, no. 40, pp. 18868–18875, 2005.

[140] K. F. Hsu, S. Loo, F. Guo, W. Chen, J. S. Dyck, C. Uher, T. Hogan, E. K. Polychroniadis, and M. G. Kanatzidis, “Cubic $AgPb_mSbTe_{2+m}$: bulk thermoelectric materials with high figure of merit,” *Science*, vol. 303, no. 5659, pp. 818–821, 2004.

[141] C. Persson, Y.-J. Zhao, S. Lany, and A. Zunger, “n-type doping of $CuInSe_2$ and $CuGaSe_2$,” *Physical Review B*, vol. 72, no. 3, p. 035211, 2005.

[142] T. K. Todorov, K. B. Reuter, and D. B. Mitzi, “High-efficiency solar cell with earth-abundant liquid-processed absorber,” *Advanced materials*, vol. 22, no. 20, pp. E156–E159, 2010.

[143] S. Chen, A. Walsh, Y. Luo, J.-H. Yang, X. Gong, and S.-H. Wei, “Wurtzite-derived polytypes of kesterite and stannite quaternary chalcogenide semiconductors,” *Physical Review B*, vol. 82, no. 19, p. 195203, 2010.

[144] F. Gamble, F. DiSalvo, R. Klemm, and T. Geballe, “Superconductivity in layered structure organometallic crystals,” *Science*, vol. 168, no. 3931, pp. 568–570, 1970.

[145] L. Mattheiss, “Band structures of transition-metal-dichalcogenide layer compounds,” *Physical Review B*, vol. 8, no. 8, p. 3719, 1973.

[146] M. S. Whittingham, “Chemistry of intercalation compounds: metal guests in chalcogenide hosts,” *Progress in Solid State Chemistry*, vol. 12, no. 1, pp. 41–99, 1978.

[147] E. Levi, G. Gershinsky, D. Aurbach, O. Isnard, and G. Ceder, “New insight on the unusually high ionic mobility in chevrel phases,” *Chemistry of materials*, vol. 21, no. 7, pp. 1390–1399, 2009.

[148] A. Nozik, “Quantum dot solar cells,” *Physica E: Low-dimensional Systems and Nanostructures*, vol. 14, no. 1-2, pp. 115–120, 2002.

[149] H.-J. Eisler, V. C. Sundar, M. G. Bawendi, M. Walsh, H. I. Smith, and V. Klimov, “Color-selective semiconductor nanocrystal laser,” *Applied physics letters*, vol. 80, no. 24, pp. 4614–4616, 2002.

[150] S. Jia, H. Ji, E. Climent-Pascual, M. Fuccillo, M. Charles, J. Xiong, N. Ong, and R. Cava, “Low-carrier-concentration crystals of the topological insulator Bi_2Te_2Se,” *Physical Review B*, vol. 84, no. 23, p. 235206, 2011.

[151] M. Chhowalla, H. S. Shin, G. Eda, L.-J. Li, K. P. Loh, and H. Zhang, "The chemistry of two-dimensional layered transition metal dichalcogenide nanosheets," *Nature chemistry*, vol. 5, no. 4, p. 263, 2013.

[152] G. K. Behrh, M. Isobe, F. Massuyeau, H. Serier-Brault, E. E. Gordon, H.-J. Koo, M.-H. Whangbo, R. Gautier, and S. Jobic, "Oxygen-vacancy-induced midgap states responsible for the fluorescence and the long-lasting phosphorescence of the inverse spinel Mg(Mg,Sn)O_4," *Chemistry of Materials*, vol. 29, no. 3, pp. 1069–1075, 2017.

[153] S. M. Griffin, M. Reidulff, S. M. Selbach, and N. A. Spaldin, "Defect chemistry as a crystal structure design parameter: Intrinsic point defects and Ga substitution in $InMnO_3$," *Chemistry of Materials*, vol. 29, no. 6, pp. 2425–2434, 2017.

[154] P. Canepa, S. Bo, G. Gautam, B. Key, W. D. Richards, T. Shi, Y. Tian, Y. Wang, J. Li, and G. Ceder, "High magnesium mobility in ternary spinel chalcogenides," vol. 8, no. 1, 2017.

[155] P. Canepa, G. Sai Gautam, D. C. Hannah, R. Malik, M. Liu, K. G. Gallagher, K. A. Persson, and G. Ceder, "Odyssey of multivalent cathode materials: open questions and future challenges," *Chemical reviews*, vol. 117, no. 5, pp. 4287–4341, 2017.

[156] N. Kamaya, K. Homma, Y. Yamakawa, M. Hirayama, R. Kanno, M. Yonemura, T. Kamiyama, Y. Kato, S. Hama, K. Kawamoto, *et al.*, "A lithium superionic conductor," *Nature materials*, vol. 10, no. 9, p. 682, 2011.

[157] P. Canepa, G. Gautam, D. Broberg, S. Bo, and G. Ceder, "Role of point defects in spinel Mg chalcogenide conductors," *Chem Mater*, 2017.

[158] L. Gastaldi and A. Lapiccirella, "Three different methods of determining the cation distribution in spinels: A comparison," *Journal of Solid State Chemistry*, vol. 30, no. 2, pp. 223–229, 1979.

[159] J. A. Weil, "A review of electron spin spectroscopy and its application to the study of paramagnetic defects in crystalline quartz," *Physics and Chemistry of Minerals*, vol. 10, no. 4, pp. 149–165, 1984.

[160] S. Livraghi, M. C. Paganini, E. Giamello, A. Selloni, C. Di Valentin, and G. Pacchioni, "Origin of photoactivity of nitrogen-doped titanium dioxide under visible light," *Journal of the American Chemical Society*, vol. 128, no. 49, pp. 15666–15671, 2006.

[161] M. Brian, J. Sites, M. Brian, and J. Sites, *Cadmium Telluride Solar Cells*. Wiley, 2010.

[162] W. Shockley and H. J. Queisser, "Detailed balance limit of efficiency of p-n junction solar cells," *J Appl Phys*, vol. 32, no. 3, pp. 510–519, 1961.

[163] C. D. Bailie and M. M. D, “High-efficiency tandem perovskite solar cells,” *Mrs Bull*, vol. 40, no. 8, pp. 681–686, 2015.

[164] M. Graetzel, R. Janssen, D. Mitzi, and S. E. Nature, “Materials interface engineering for solution-processed photovoltaics,” *Nature*, 2012.

[165] M. A. Green, H. Anita, and H. J. Snaith, “The emergence of perovskite solar cells,” *Nat Photonics*, vol. 8, no. 7, pp. 506–514, 2014.

[166] H. J. Snaith, “Perovskites: The emergence of a new era for Low-Cost, High-Efficiency solar cells,” *J Phys Chem Lett*, vol. 4, no. 21, pp. 3623–3630, 2013.

[167] “The National Renewable Energy Laboratory’s Best Research-Cell Efficiencies Chart.” https://www.nrel.gov/pv/cell-efficiency.html, 2019.

[168] W. Yin, J. Yang, J. Kang, Y. Yan, and S. Wei, “Halide perovskite materials for solar cells: a theoretical review,” *J Mater Chem A*, vol. 3, no. 17, pp. 8926–8942, 2014.

[169] G. Niu, X. Guo, and L. Wang, “Review of recent progress in chemical stability of perovskite solar cells,” vol. 3, no. 17, pp. 8970–8980, 2014.

[170] I. Chung and M. G. Kanatzidis, “$CsSnI_3$: semiconductor or metal? high electrical conductivity and strong Near-Infrared photoluminescence from a single material. high hole mobility and Phase-Transitions,” 2012.

[171] L.-y. Huang and W. R. Lambrecht, “Electronic band structure trends of perovskite halides: Beyond Pb and Sn to Ge and Si,” *Phys Rev B*, vol. 93, no. 19, p. 195211, 2016.

[172] D. Krasikov and I. Sankin, “Beyond thermodynamic defect models: A kinetic simulation of arsenic activation in CdTe,” *Phys Rev Mater*, vol. 2, no. 10, p. 103803, 2018.

[173] D. De Nobel, “Phase equilibria and semiconducting properties of cadmium telluride,” *Philips. Res. Repts.*, vol. 14, 1959.

[174] A. Alkauskas, P. Broqvist, and A. Pasquarello, “Defect levels through hybrid density functionals: Insights and applications,” *Phys Status Solidi B*, vol. 248, no. 4, pp. 775–789, 2011.

[175] Q. Chen, M. Hillert, B. Sundman, W. Oates, S. Fries, and S. R, “Phase equilibria, defect chemistry and semiconducting properties of CdTe(s)—Thermodynamic modeling,” vol. 27, no. 8, pp. 961–971, 1998.

[176] C. Freysoldt, B. Lange, J. Neugebauer, Q. Yan, J. L. Lyons, A. Janotti, and C. G. de Walle, “Electron and chemical reservoir corrections for point-defect formation energies,” vol. 93, no. 16, 2016.

[177] A. Rowberg, L. Weston, and C. Walle, "Optimizing proton conductivity in zirconates through defect engineering," *Acs Appl Energy Mater*, 2019.

[178] A. Rowberg, L. Weston, and C. Walle, "Ion-transport engineering of alkaline-earth hydrides for hydride electrolyte applications," *Chem Mater*, 2018.

[179] J. B. Varley, A. Samanta, and V. Lordi, "Descriptor-Based approach for the prediction of cation vacancy formation energies and transition levels.," *J Phys Chem Lett*, vol. 8, no. 20, pp. 5059–5063, 2017.

[180] S. Dixon, S. Sathasivam, B. Williamson, D. Scanlon, C. Carmalt, and I. Parkin, "Transparent conducting n-type ZnO:Sc – synthesis, optoelectronic properties and theoretical insight," *J Mater Chem C*, vol. 5, no. 30, pp. 7585–7597, 2017.

[181] Q. Miguel, B. Williamson, S. Carlos, A. Kafizas, N. Boscher, Q. Raul, D. Scanlon, C. Carmalt, and I. Parkin, "A deeper understanding of interstitial Boron-Doped anatase thin films as a multifunctional layer through theory and experiment," *J Phys Chem C*, 2017.

[182] J. Swallow, B. Williamson, T. Whittles, M. Birkett, T. Featherstone, N. Peng, A. Abbott, M. Farnworth, K. Cheetham, P. Warren, D. Scanlon, V. Dhanak, and T. Veal, "Self-Compensation in transparent conducting F-Doped SnO_2," *Adv Funct Mater*, vol. 28, no. 4, p. 1701900, 2018.

[183] S. D. Ponja, B. A. Williamson, S. Sathasivam, D. O. Scanlon, I. P. Parkin, and C. J. Carmalt, "Enhanced electrical properties of antimony doped tin oxide thin films deposited via aerosol assisted chemical vapour deposition," *J Mater Chem C*, vol. 6, no. 27, pp. 7257–7266, 2018.

[184] M. Powell, B. Williamson, S. Baek, J. Manzi, D. Potter, D. Scanlon, and C. Carmalt, "Phosphorus doped SnO_2 thin films for transparent conducting oxide applications: synthesis, optoelectronic properties and computational models," *Chem Sci*, vol. 9, no. 41, pp. 7968–7980, 2018.

[185] N. Adamski, Z. Zhu, D. Wickramaratne, C. Walle, N. Adamski, Z. Zhu, D. Wickramaratne, and C. Walle, "Hybrid functional study of native point defects and impurities in $ZnGeN_2$," *J Appl Phys*, vol. 122, no. 19, p. 195701, 2017.

[186] W. Chen, J. Pöhls, G. Hautier, D. Broberg, S. Bajaj, U. Aydemir, Z. M. Gibbs, H. Zhu, M. Asta, J. G. Snyder, B. Meredig, M. White, K. Persson, and A. Jain, "Understanding thermoelectric properties from high-throughput calculations: trends, insights, and comparisons with experiment," *J Mater Chem C*, vol. 4, no. 20, pp. 4414–4426, 2016.

[187] M. H. Naik and M. Jain, "CoFFEE: corrections for formation energy and eigenvalues for charged defect simulations," vol. 226, pp. 114–126, 2018.

[188] A. D. Becke, "A new mixing of Hartree–Fock and local density-functional theories," *J Chem Phys*, vol. 98, no. 2, pp. 1372–1377, 1993.

[189] S. Wei and S. Zhang, "Chemical trends of defect formation and doping limit in II-VI semiconductors: The case of CdTe," 2002.

[190] M. Leslie and M. Gillan, "The energy and elastic dipole tensor of defects in ionic crystals calculated by the supercell method," 0.

[191] A. Alkauskas, P. Broqvist, and A. Pasquarello, "Defect energy levels in density functional calculations: Alignment and band gap problem," *Phys Rev Lett*, vol. 101, no. 4, p. 046405, 2008.

[192] K. Bystrom, D. Broberg, S. Dwaraknath, K. A. Persson, and M. Asta, "Pawpyseed: Perturbation-extrapolation band shifting corrections for point defect calculations," 2019.

[193] K. Mathew, J. H. Montoya, A. Faghaninia, S. Dwarakanath, M. Aykol, H. Tang, I.-h. Chu, T. Smidt, B. Bocklund, M. Horton, J. Dagdelen, B. Wood, Z. Liu, J. Neaton, S. Ong, K. Persson, and A. Jain, "Atomate: A high-level interface to generate, execute, and analyze computational materials science workflows," *Comp Mater Sci*, vol. 139, pp. 140–152, 2017.

[194] S. Dwaraknath, "emmet." Github: https://github.com/materialsproject/emmet, 2017.

[195] G. Kresse and J. Hafner, "Ab initio molecular-dynamics simulation of the liquid-metal-amorphous-semiconductor transition in germanium," *Phys. Rev. B*, vol. 49, p. 14251, 1994.

[196] G. Kresse and J. Furthmüller, "Efficient iterative schemes for ab initio total-energy calculations using a plane-wave basis set," *Phys Rev B*, vol. 54, no. 16, pp. 11169–11186, 1996.

[197] P. Blöchl, "Projector augmented-wave method," *Phys Rev B*, vol. 50, no. 24, pp. 17953–17979, 1994.

[198] P. Mooney, "Deep donor levels (DX centers) in III-V semiconductors," vol. 67, no. 3, pp. R1–R26, 1990.

[199] T. Angsten, L. W. Martin, and M. Asta, "Orientation-dependent properties of epitaxially strained perovskite oxide thin films: Insights from first-principles calculations," *Physical Review B*, vol. 95, no. 17, p. 174110, 2017.

APPENDIX A

Charge States from Literature for PyCDT Charge Analysis

Table A.1: Charge states from literature; brackets refer to hybrid functional rather than (semi-)local functional results.

Structure	Defect	Charge States		Ref.
		from	to	
C	V_C	+2	−2	88
	N_C	+1	−1	
AlP	V_{Al}	0	−3	73
	V_P	+1	−2	
	Al_P	+1	−2	89
	P_{Al}	+2	−2	
AlAs	V_{Al}	0	−3	73
	V_{As}	+1	−2	
	Al_{As}	+1	−2	89
	As_{Al}	+1	−1	
AlSb	V_{Al}	0	−3	73
	V_{Sb}	+1	−3	
	Al_{Sb}	0	−2	89
	Sb_{Al}	+1	−1	
Si	V_{Si}	+2	−2	90
ZnS	V_S	+2	0	91
	V_{Zn}	0 (+1)	−2	91 (28)
	S_{Zn}	0	−2	91
	Zn_S	+2	0	
	Zn_i	+2	0	
	S_i	0	−2	

To be continued on next page.

Structure	Defect	Charge States from	to	Ref.
ZnSe	V_{Se}	+2	−2	92
	V_{Zn}	+2	−2	
	Cl_{Se}	+2	−1	
	F_{Se}	+1	−2	
	F_{Zn}	−2	−2	
ZnTe	V_{Zn}	0 (+1)	−2	28
GaN	V_{Ga}	0 (+1)	−3	93 (28)
	V_{N}	+1	+1	93
	Ga_{N}	+1	−2	
	N_{Ga}	+2	−1	
	N_i	+3	−1	
	Ga_i	+3	+1	
	C_{N}	0 (+1)	−1	28
GaP	V_{Ga}	0	−3	73
	V_{P}	+1	−3	
	Ga_{P}	0	−2	89
	P_{Ga}	+2	−2	
GaAs	V_{Ga}	−1	−3	73
	V_{As}	+1	−3	
	Ga_{As}	0	−3	89
	As_{Ga}	+1	−2	
GaSb	V_{Ga}	0	−3	73
	V_{Sb}	0	−3	
	Ga_{Sb}	0	−2	89
	Sb_{Ga}	+1	−1	
CdS	V_{S}	+2	0	59
	V_{Cd}	0	−2	
	Cd_{S}	+2	+2	
	S_{Cd}	+4	−2	
	Cd_i	+2	+2	
	S_i	+4	−2	
	Mn_{Cd}	+1	0	
	Fe_{Cd}	+2	0	
	Co_{Cd}	+1	0	
	Ni_{Cd}	+1	0	
	Mn_i	+3	+2	
	Fe_i	+3	+2	
	Co_i	+3	+2	
	Ni_i	+2	+1	

To be continued on next page.

Structure	Defect	Charge States from	to	Ref.
InP	V_{In}	0	-3	73
	V_{P}	$+1$	-1	
	In_{P}	$+1$	-2	89
	P_{In}	$+2$	-1	
InAs	V_{In}	0	-2	73
	V_{As}	$+1$	0	
	$\mathrm{In}_{\mathrm{As}}$	0	-1	89
	$\mathrm{As}_{\mathrm{In}}$	$+1$	0	
InSb	V_{In}	-1	-2	73
	V_{Sb}	$+1$	0	
	$\mathrm{In}_{\mathrm{Sb}}$	0	-1	89
	$\mathrm{Sb}_{\mathrm{In}}$	$+1$	0	

APPENDIX B

Practical Notes on PyCDT

B.1 Overview of PyCDT Codebase

In Chapter 2, we gave an overview of PyCDT and described how PyCDT can be used from command line. PyCDT is implemented in Python and leverages the language's flexibility. For those users interested in using PyCDT for high-throughput defect calculations or customizing PyCDT, in this Appendix, the core classes in PyCDT are briefly described. Python snippets are given to showcase few usage scenarios. To use PyCDT in python scripts, we expect the users to be familiar with the pymatgen codebase also. For more details, python's help command would be helpful.

PyCDT consists of classes implementing a specific functionality as well as scripts that use the defined classes in accomplishing the desired tasks. The implementation of PyCDT's command line is nothing but a python script calling different classes based on user input arguments. For minor customization, editing the PyCDT command line script should suffice. Based on the functionality implemented, PyCDT can be broadly divided into three components: a) code to set up defect calculations, b) post-processing the defect calculations including corrections to various errors associated with density functional theory based supercell formalism, and c) defect thermodynamics.

B.1.1 Set up of Defect Supercell Calculations

In PyCDT, setting up defect supercell calculations is accomplished in three stages. Generating defect supercells, assigning charges to the defects, and generating DFT inputs corresponding to each supercell and charge state.

Defect Charge Assignment

To assign defect charges, we need to know the oxidation state of the ions in the crystal as well as the range of oxidation states admitted by the ions in the crystal. While the latter can be easily obtained by referring to the commonly available ion oxidation tables, the former is evaluated using a bond-valence based charge assignment procedure. This procedure developed by the authors and implemented in pymatgen as *ValenceIonicRadiusEvaluator* class had been tested on hundreds of crystal structures and was found to work even in mixed valence compounds. Once the charge of the ions in the crystal were determined, the range of the defect charges was calculated based on defect type, the range of valences of the ions in the crystal. The abstract base class *DefectCharger* in *pycdt.core.defectsmaker* defines the prototype class of charge assignment. The users have the choice to assign various charges ranges for defects based on whether the crystal is ionic or semiconductor compound. Both the charge assignment procedures were implemented in *DefectChargerInsulator*, and *DefectChargerSemiconductor* respectively. For ionic compounds, for example MgO, Mg vacancy admits [0, -1, -2] charges and the anion vacancy admits [0, 1, 2] charges. A sample script to obtain the defect charges in MgO is given below.

```
# Get MgO structure from MP database
from pymatgen.ext.matproj import MPRester
with MPRester() as mpr:
    mgo_struct = mpr.get_structure_by_material_id('mp-1265')
# Automatic Defect Charge Assignment for ionic crystals
from pycdt.core.defectsmaker import DefectChargerInsulator
defect_charger = DefectChargerInsulator(mgo_struct)
# Charges for Mg vacancy
mg_vac_charges = defect_charger.get_charges('vacancy', site_specie='Mg')
```

Defect Supercell Generation

To generate vacancy, substitutional, and antisite defects, the symmetry of the input structure is analyzed and each of the symmetrically distinct site is used as a defect site. For interstitials, bond-order parameter based interstitial generation algorithm which performs a grid-search is utilized. The development of the above mentioned algorithms precedes the development of PyCDT and were implemented in pymatgen by the developers. An alternative version for interstitial generation based on Voronoi decomposition was also implemented by the authors in pymatgen. For interstitial generation algorithm to be effective, correct ionic radii are required. To accurately predict ionic radii that are based on valence of ions in the crystal, we utilized the ionic valences identified in *ValenceIonicRadiusEvaluator*. The class returns the ionic radii of the symmetrically distinct ions in the crystal. Further, PyCDT generates maximally cubic defect supercells by minimizing the differences in a, b, c of the defect supercells.

DFT Settings

The DFT settings for defect calculations are automatically generated by classes *DefectRelaxSet* and *DefectStaticSet*. Both are subclassed from *MPRelaxSet* and *MPStaticSet* classes in pymatgen to take advantage of the heuristic knowledge encoded in pymatgen to perform high-throughput DFT calculations. *MP*{*Relax,Static*}*Set* classes can automatically set up many VASP parameters based on the input crystal structure including LDA+U parameters without any user input. In the defect subclasses, some parameters are added or modified to suit defect calculations, for example setting VASP parameters *LVTOT* and *LVHAR* to True to compute finite size electrostatic corrections. Users can alter any settings or give new settings as keyword arguments to the classes. A python snippet generating DFT inputs to a particular defect structure is given below.

```python
# Vasp Input Generation for Defect Structure
from pycdt.core.defectsmaker import ChargedDefectsStructures
charged_defects_structs = ChargedDefectsStructures(mgo_struct)
from pycdt.utils.vasp import DefectRelaxSet
defect_struct = charged_defects_structs.get_ith_supercell_of_defect_type(
           0, 'vacancies')
vasp_input = DefectRelaxSet(defect_struct) # defect_struct is defect supercell
vasp_input.write_input(output_dir) # Writes VASP inputs to output_dir
# To change functional to PW91 input the choice as keyword argument
vasp_input = DefectRelaxSet(defect_struct, potcar_functional="PW91")
# Alternatively to input multiple settings
user_settings = {
           'potcar_functional': 'PW91',
           'user_incar_settings': {
                 'EDIFFG': -1e-3, 'EDIFF': 1e-8, 'LASPH': True}}
vasp_input = DefectRelaxSet(defect_struct, **user_settings)
```

When working from command line, the same settings can be given from a yaml file with the following syntax.

```yaml
POTCAR:
  functional: PW91
INCAR:
  EDIFF: 1e-8
  defects:
    EDIFFG: -1e-3
    EDIFF: 1e-7
    LASPH: True
  dielectric:
    EDIFF: 1e-9
```

When the functional is changed, in practice, it is changed for all the calculations related to defects, bulk, dielectric, and chemical potential evaluations. The full format of the YAML file is given below.

```
POTCAR:
  <keyword1_all>: <value1_all>
  <keyword2_all>: <value2_all>
  ...
INCAR:
  <keyword1_all>: <value1_all>
  <keyword2_all>: <value2_all>
  ...
  bulk:
    <keyword1_bulk>: <value1_bulk>
    <keyword2_bulk>: <value2_bulk>
    ...
  defects:
    <keyword1_defects>: <value1_defects>
    <keyword2_defects>: <value2_defects>
    ...
  dielectric:
    <keyword1_dielectric>: <value1_dielectric>
    <keyword2_dielectric>: <value2_dielectric>
    ...
chempot:
  <keyword1_chempot>: <value1_chempot>
  <keyword2_chempot>: <value2_chempot>
  ...
```

In the above file, *keyword1_all* and *value1_all* are the keyword, value pair that applies to all the calculations. The keyword, value pairs that fall under under either of bulk, defects, dielectric, chempot sections apply only to relevant calculations. If a *keyword_defects* equals a *keyword_all*, then the corresponding *value_defects* overrides the corresponding *value_all* for defect calculations. The same logic applies to other sections as well.

B.1.2 Chemical Potentials

The class *ChemPotAnalyzer* is used to compute the atomic chemical potentials based on the computed phase diagram of a material. The thermodynamic aspects of this approach are described at length in Section 2.3.3 of the main text. To provide chemical potentials from the Materials Project database, the *MPChemPotAnalyzer* is subclassed from *ChemPotAnalyzer*. This subclass is capable of pulling a Pymatgen *PhaseDiagram* object from the Materials Project database based on a given bulk composition. Once this object is pulled, the relevant facets of the phase diagram that are adjacent to the composition of interest are identified. With these facets, the subclass then makes use of the linear programming aspects of *ChemPotAnalyzer* to determine numerical values for the chemical potentials in the various growth extremes of the phase diagram. A sample script for obtaining the atomic chemical potentials of GaAs is provided below.

```
from pycdt.core.chemical_potentials import MPChemPotAnalyzer
from monty.serialization import dumpfn
from monty.json import MontyEncoder
cpa = MPChemPotAnalyzer(mpid='mp-2534') #this is mp-id for GaAs
chempot_data = cpa.analyze_GGA_chempots()
dumpfn(chempot_data, 'chempots.json', cls=MontyEncoder, indent=2)
```

As identified in the main text, it is also possible to set up and parse chemical potentials in the case of a user computed phase diagram. This is important if a user decides to calculate the formation energetics on a level of DFT that is not pre-computed by the Materials Project (i.e. spin-orbit coupling, hybrid functionals etc.).

The class *UserChemPotInputGenerator* is provided for pulling the structure objects from the Materials Project phase diagram. The code provided below allows for set up of the relevant phases of a GaAs calculation in a local directory called 'PhaseDiagram'. By default only the structure files are provided for set up, however, additional file set up is straight forward by using the methods outlined in the DFT Settings section of this Appendix.

```
from pycdt.core.chemical_potentials import UserChemPotInputGenerator
from pymatgen.core.composition import Composition
cpa = UserChemPotInputGenerator(Composition({'Ga': 1, 'As': 1}))
cpa.setup_phase_diagram_calculations()
```

After the calculations that were set up in the 'PhaseDiagram' directory have been run, the user can make use of the *UserChemPotAnalyzer*, which has also been subclassed from the *ChemPotAnalyzer*. The following example code allows for a user to run follow-up parsing of the chemical potentials. Here we make use of the ease of conversion of VASP's vasprun.xml files to ComputedEntry objects with pymatgen. This can be expanded to arbitrary DFT codes by similarly instantiating a ComputedEntry object from the code's output files.

```
from pycdt.core.chemical_potentials import UserChemPotAnalyzer
from pymatgen.io.vasp import Vasprun
from monty.serialization import dumpfn
from monty.json import MontyEncoder
bulk_vr = Vasprun('path_to_bulk/vasprun.xml') #provide a path to the computed
    bulk vasprun file
bulk_ce = bulk_vr.get_computed_entry()
cpa = UserChemPotAnalyzer(bulk_ce)
chempot_data = cpa.analyze_GGA_chempots()
dumpfn(chempot_data, 'chempots.json', cls=MontyEncoder, indent=2)
```

It is possible that additional phases which were not documented in the ICSD (and therefore may not exist in the MP database) may influence the determination of the atomic chemical potentials. If the user knows of such a structure, then they can compute the structure on their own and achieve manual insertion of the computed entry into the phase diagram by including the files within the local PhaseDiagram folder.

As a comment on computational time saved for this method, if a user desires to run this procedure on their own, many steps would be required. They would first need to research the structures that are stable within the phase diagram of their composition of interest. As an example case where this become an arduous task, consider the phase diagram of the Fe-P-O system considered by Jain *et al.* [77]. In this system they find a total of 20 phases, with close competition for stability in the middle of the phase diagram. If a user wished to perform defect calculations on a material in this system, they must both set up and run the structures adjacent to the composition of interest in the phase diagram. Considerable computational time can be saved by either making use of PyCDT's quick queries of the calculations already performed by the MP or by making use of PyCDT's quick set up feature for the intial starting point of the MP documented structures. The user would then need to formulate a system of equations (a procedure discussed at length within Section 2.3.3) and solve for the atomic chemical potentials in the various regions of interest. While many have gone through the practice of setting up their own codes to perform this task, PyCDT provides an open source, robust interface for expediting this process.

B.1.3 Post-processing

The class *ComputedDefect* in *pycdt.core.defects_analyzer* is used to represent the data of a relaxed defect, such as its structure, total energy from the defect calculation, any corrections associated with the energy, multiplicity, etc.

After the DFT calculations of the defects in a material are completed, the computed data of all the defects as well as the bulk data required for defect thermodynamics can be obtained with *PostProcess* class. This class is somewhat similar to the *BorgQueen* class in pymatgen. The calculations pertaining to defect supercells, dielectric constant, and bulk supercell, whose inputs are generated with PyCDT, can be parsed with few of lines of code.

```
from pycdt.utils.parse_calculations import PostProcess
from monty.serialization import dumpfn
from monty.json import MontyEncoder
defect_data = PostProcess(root_dir, mpid).compile_all()
dumpfn(defect_data, 'data.json', cls=MontyEncoder, indent=2)
```

Finite Size Electrostatic Error Correction

Two correction schemes were implemented to reduce the electrostatic error due to finite size supercells. Freysoldt, Neugebauer, Van de Walle (FNV) scheme and its anisotropic counterpart by Kumagai and Oba can be used for isotropic and anisotropic systems [34, 35]. The code snippet below shows how to call FNV correction on a charged defect calculation.

```
from pymatgen.io.vasp.outputs import Locpot
from pycdt.corrections.finite_size_charge_correction import \
          get_correction_freysoldt
blk_locpot = Locpot.from_file('bulk_locpot_path')
fnv_correction, = get_correction_freysoldt(
          defect, blk_locpot, epsilon, title='example_fnv')
#Here defect is ComputedDefect object
#blk_locpot is the LOCPOT object from bulk supercell calculation
#epsilon is the dielectric constant
#Names of any plots generated start with example_fnv
```

Calling anisotropic charge correction is slightly more involved as shown in the code snippet below.

```
from pycdt.corrections.finite_size_charge_correction import \
          get_correction_kumagai
from pycdt.corrections.kumagai_correction import KumagaiBulkInit
kumagai_init = KumagaiBulkInit(blk_locpot.structure, blk_locpot.dim,
                              epsilon, encut, tolerance=1e-4)
anistropic_fnv_correction = get_correction_kumagai(
          defect, path_blk, kumagai_init, bulk_locpot=blk_locpot,
          title='example_aniso_fnv')
```

B.1.4 Defect Thermodynamics

The class *DefectsAnalyzer* is used to compute the thermodynamics of the defects in a material. As such, the class requires the bulk properties such as bulk structure, total energy of the bulk structure, dielectric constant, band structure details, etc. In addition the optimized defects represented by the ComputedDefect objects are also input to the class.

Based on the above data, the class provides method functions to compute transition levels, defect formation energies, and band gap related corrections to the formation energies.

```
#To initialize DefectsAnalyzer, supply the bulk properties as below
#bulk_entry is pymatgen ComputedStructureEntry object
#vbm: Valence Band Minimum
#mu: Chemical potentials in python dictionary format at the phase boundaries
#bandgap: Experimental bandgap
da = DefectsAnalyzer(blk_entry, vbm, mu, bandgap)
#Add a defect
da.add_computed_defect(defect) # defect is ComputedDefect object
#Once all the defects are added, get transition levels as
```

```
da.get_transition_levels()
#To plot formation, input DefectsAnalyzer object to DefectPlotter
plotter = DefectPlotter(da)
form_en_plot = plotter.get_plot_form_energy()
#form_en_plot is a matplotlib object. It can be saved to the formats supported
form_en_plot.savefig('defect_formation_energy.png')
```

B.2 Example Customization of PyCDT Core Functionality

B.2.1 Interstitial charge state screening

Determining the relevant charge state and stability of self-interstitials can be difficult. For example, when considering defects that contain nitrogen, a large range of possible oxidation states can occur as a result of the variety of oxidation states that nitrogen can assume. One solution is to run the defects in a large variety of possible oxidation states. However, this procedure introduces the possibility of computing many excess charges which do not have the lowest formation energy for all values of the Fermi level within the gap. This wasted computational time becomes particularly important to consider if one wishes to perform defects on the scale of high-throughput with reasonable computational resources. In this subsection, we demonstrate a manner for adapting the core functionality of PyCDT to calculate relevant charge states for a defect in a computationally efficient manner.

Initialization of defect files can be done through the manner described in Section 3 or through custom adaptations of the ChargedDefectsStructures class of PyCDT. Rather than running DFT calculations of all of these charges at once, an alternate procedure is to incrementally consider additional charge states of the defects through use of the PyCDT core functionality. The procedure goes as follows:

1. Run the neutral charge state of each defect produced by PyCDT.
2. Use the DefectsAnalyzer to determine the minimum formation energy from each chemical potential region, for each defect.
3. Only run follow up analysis on defects which have a neutral formation energy less than some set tolerance
4. Parse and pull together results within the DefectsAnalyzer module of PyCDT to quantify the position of the transition states relative to the band edges.
5. For each defect, check to see if the transition to a more stable positive (negative) charge state is above (below) the valence band (conduction band). If it is not, then use the

ChargedDefectsStructures to set up the next positive (negative) charge state for the defect and run the DFT calculation.

6. Repeat from Step (4) until both positive and negative charge states have transition levels outside of the band gap.

This procedures provides one example for how the core set of PyCDT can be customized to perform any number of custom tasks for expediting high-thoughput DFT calculations of point defects in semiconductors.

APPENDIX C

Materials Used in PyCDT Data Set

	Name	Spacegroup	Materials Project ID
1	AlP	$F\bar{4}3m$	mp-1550
2	AlAs	$F\bar{4}3m$	mp-2172
3	AlSb	$F\bar{4}3m$	mp-2624
4	BP	$F\bar{4}3m$	mp-1479
5	C	$F\bar{4}3m$	mp-66
6	CdS	$F\bar{4}3m$	mp-2469
7	CdSe	$F\bar{4}3m$	mp-2691
8	CdTe	$F\bar{4}3m$	mp-406
9	GaAs	$F\bar{4}3m$	mp-2534
10	GaN	$F\bar{4}3m$	mp-830
11	GaP	$F\bar{4}3m$	mp-2490
12	GaSb	$F\bar{4}3m$	mp-1156
13	Si	$F\bar{4}3m$	mp-149
14	ZnS	$F\bar{4}3m$	mp-10695
15	ZnSe	$F\bar{4}3m$	mp-1190
16	ZnTe	$F\bar{4}3m$	mp-2176
17	ZnO	$P6_3mc$	mp-2133
18	Cu_2O	$Pn\bar{3}m$	mp-361
19	Ag_3PO_4	$P\bar{4}3n$	mp-4198
20	Rb_3AuO	$Pm\bar{3}m$	mp-4405
21	K_3AuO	$Pm\bar{3}m$	mp-9200

Table C.1: Table of Materials from Test Set of Chapter 2

APPENDIX D

Details on Workflow for Defect Automation

This section describes the workflow that was used for full automation of charged defect calculations with DFT. The functionalities displayed here are extensions of the PyCDT code base [136] which were refactored into the pymatgen [76], atomate [193] and emmet [194] code bases to produce a fully automated defect workflow which is compatible with the Materials Project infrastructure [36]. All of these codes are openly available for use on their respective github pages. The overall workflow process for defect calculations is displayed in Figure D.1.

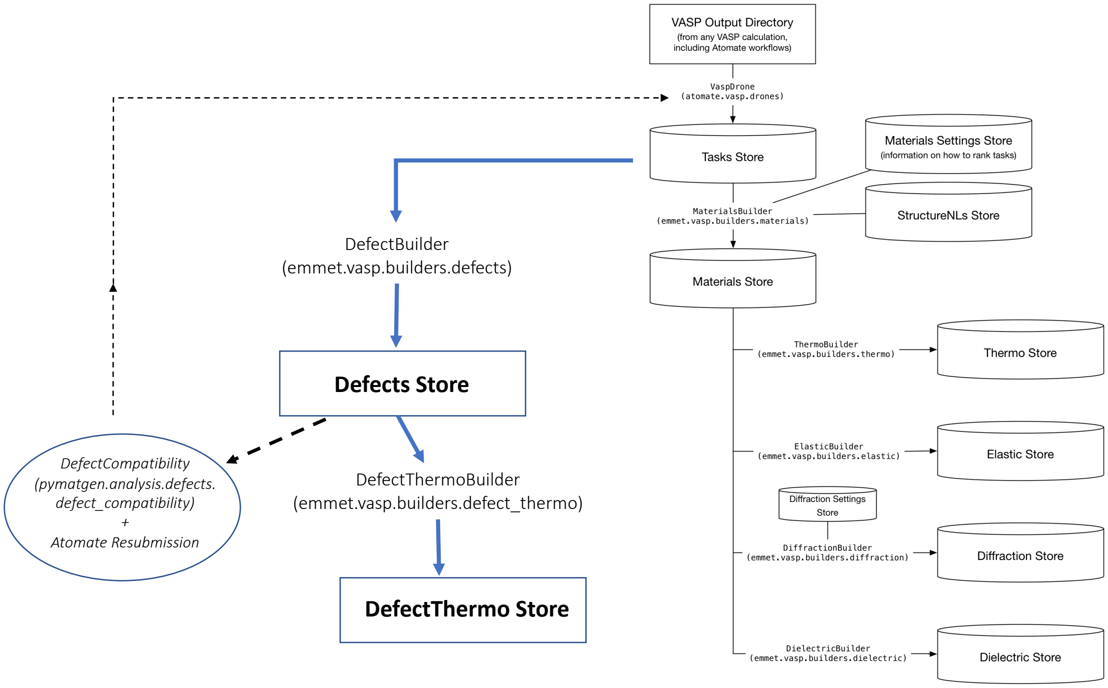

Figure D.1: Diagram of database management within Materials Project (right) and within automated defect calculations used in this work (left).

Following the practice of data provenance observed by the Materials Project database (right side of Figure D.1), a database of first principles calculations is removed from the processing stage by designating separate databases (or “Stores” in the parlance of the emmet code base). The Tasks Store contains raw information from the first principles calculations, while all other Stores contain material or thermodynamic data to be used for high-throughput screening or to be displayed on the Materials Project website. Builder objects, defined within the emmet code base, manipulate data from a given store and then push it to another store. For more information on stores and builders, refer to the emmet documentation [194].

The DefectBuilder and DefectThermoBuilder work to create the DefectsStore and DefectThermo Stores, respectively. The DefectsStore contains single Defect class objects from pymatgen, which store all metadata required for follow up corrections and formation energy analysis. The DefectThermo Store then accumulates a set of defects from the DefectsStore which have identical bulk structures and metadata for the run (same pseudopotentials etc.). After defects have been initialized within the DefectsStore, the DefectCompatibility from pymatgen works in tandem with atomate functionality to resubmit any defect calculations which are deemed incompatible based on several delocalization metrics described further in Section 4.4.1 (potential alignment sampling region variance, free carrier delocalization, or excessive structural relaxation far from the defect). Several quantitative decisions must be made when performing such an analysis, and this newly integrated code is designed to allow for customization of the values which trigger follow up calculations to be performed.

APPENDIX E

Bulk Systems Used for Benchmark Study

Table E.1: Bulk systems used for benchmark study. “mp-id” corresponds to the materials project id of each bulk structure. Hybrid version corresponds to the type of hybrid used in the corresponding reference, with α specifying the amount of exact exchange included. All gap values given in eV. “Ref. band gap” is the band gap from the corresponding Reference (Ref.) number, “Auto HSE06 gap” is the band gap from the automated HSE06 bandstructure calculation used for band gap corrections of the GGA-PBE defect calculations, and “GGA-PBE” is the band gap of the band structure computed with the GGA-PBE functional. Chemical potential facet is a list of phases which define the chemical potentials within the GGA-PBE computed phase diagram.

Name	mp-id	Hybrid flavor	Reference	Published gap	Automated HSE06 gap	PBE-GGA gap	Chemical potential facet
$CaZrO_3$_orthorhombic	mp-4571	HSE06 ($\alpha = 0.25$)	[177]	5.38	5.40	3.83	$CaZrO_3$-Zr_3O-ZrO_2-$Zr_8Sc_2O_{19}$-$Y_2Zr_8O_{19}$
SrH_2_orthorhombic	mp-23714	HSE06 ($\alpha = 0.25$)	[178]	4.18	4.22	3.15	H_2-SrH_2-KH-CsH-RbH-NaH
$BaZrO_3$_cubic	mp-3834	HSE06 ($\alpha = 0.25$)	[177]	4.52	4.44	3.04	$BaZrO_3$-Zr_3O-ZrO_2-$Zr_8Sc_2O_{19}$
ZnO_hexagonal	mp-2133	HSE ($\alpha = 0.375$)	[180]	3.39	2.40	0.73	O_2-ZnO-$Sc2O_3$
BaH_2_orthorhombic	mp-23715	HSE06 ($\alpha = 0.25$)	[178]	3.85	3.85	2.87	BaH_2-H_2-CsH-RbH-KH-NaH
ZnGeN2_orthorhombic	mp-2979	HSE06 ($\alpha = 0.25$)	[185]	3.19	3.03	1.70	Ge-Ge_3N_4-$ZnGeN_2$-Ge_2N_2O
CaH_2_orthorhombic	mp-23713	HSE06 ($\alpha = 0.25$)	[178]	4.09	4.15	3.03	CaH_2-H_2-KH-RbH-NaH
B6O_trigonal	mp-1346	HSE ($\alpha = 0.32$)	[50]	3.11	2.78	1.85	B_6O-B
TiO_2_tetragonal	mp-390	HSE06 ($\alpha = 0.25$)	[181]	3.42	3.55	2.05	O_2-TiO_2-$B2O_3$
SnO_2_tetragonal	mp-856	PBE0	[182–184]	3.65	2.26	0.65	O_2-SnO_2-SnP_2O_7-SnF_4-Sb_2O_5
BeO_cubic	mp-1778	HSE ($\alpha = 0.36$)	[179]	9.52	8.76	6.85	BeO-Be
InP_cubic	mp-20351	HSE ($\alpha = 0.32$)	[179]	1.43	1.24	0.47	InP-In
BSb_cubic	mp-997618	HSE ($\alpha = 0.32$)	[179]	1.06	1.20	0.75	B-Sb
AlP_cubic	mp-1550	HSE ($\alpha = 0.32$)	[179]	2.48	2.33	1.63	AlP-Al
ZnO_cubic	mp-1986	HSE ($\alpha = 0.36$)	[179]	3.34	2.29	0.63	ZnO-Zn
BP_cubic	mp-1479	HSE ($\alpha = 0.32$)	[179]	2.11	2.02	1.24	BP-P
ZnTe_cubic	mp-2176	HSE ($\alpha = 0.36$)	[179]	2.40	2.05	1.03	ZnTe-Te
MgTe_cubic	mp-13033	HSE ($\alpha = 0.36$)	[179]	3.53	3.13	2.32	$Mg_{149}Te$-MgTe
ZnSe_cubic	mp-1190	HSE ($\alpha = 0.36$)	[179]	2.83	2.26	1.17	ZnSe-Zn
MgS_cubic	mp-13032	HSE ($\alpha = 0.36$)	[179]	5.26	4.43	3.37	$Mg_{149}S$-MgS
BeS_cubic	mp-422	HSE ($\alpha = 0.36$)	[179]	4.54	4.21	3.15	BeS-S
MgSe_cubic	mp-13031	HSE ($\alpha = 0.36$)	[179]	4.17	3.50	2.55	$Mg_{149}Se$-MgSe
BAs_cubic	mp-10044	HSE ($\alpha = 0.32$)	[179]	1.86	1.86	1.20	B_6As-As

APPENDIX F

Formation Energy Plots for Benchmark Study

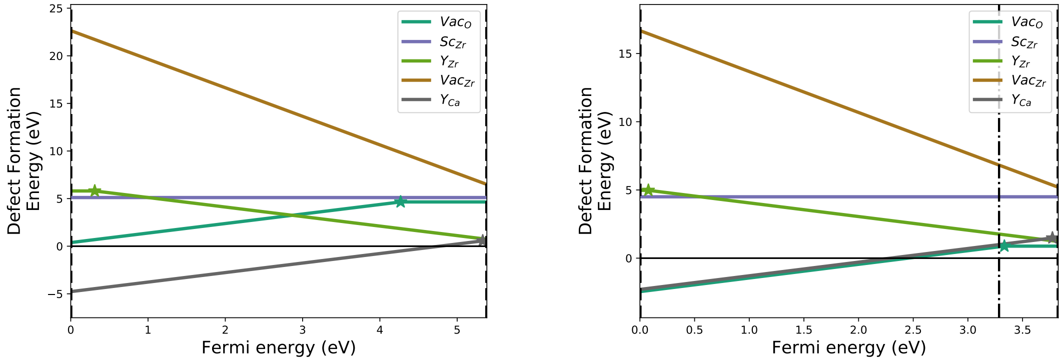

(a) Hybrid Benchmark **(b)** no_bes

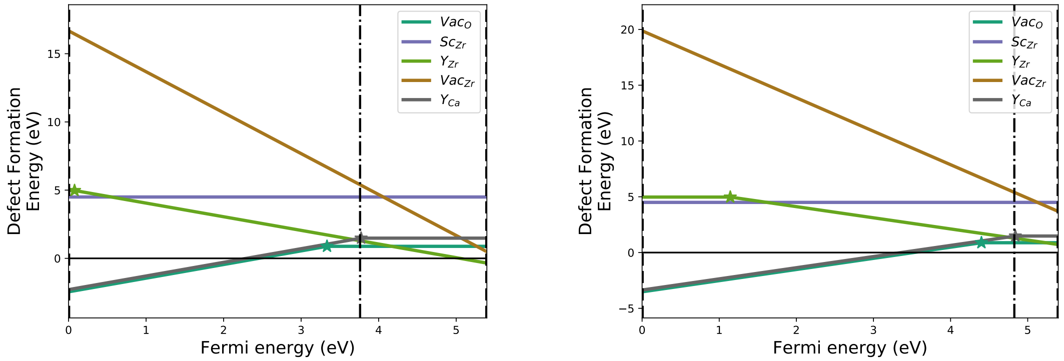

(c) BS_bes **(d)** bes

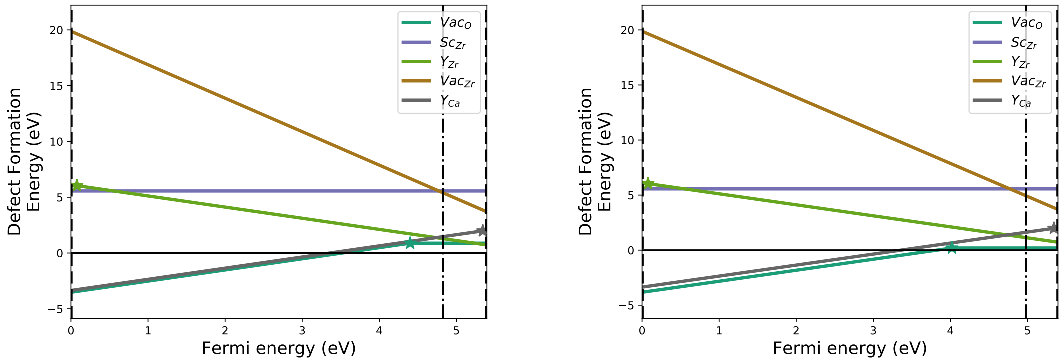

(e) dls1 **(f)** dls2

Figure F.1: CaZrO3_orthorhombic

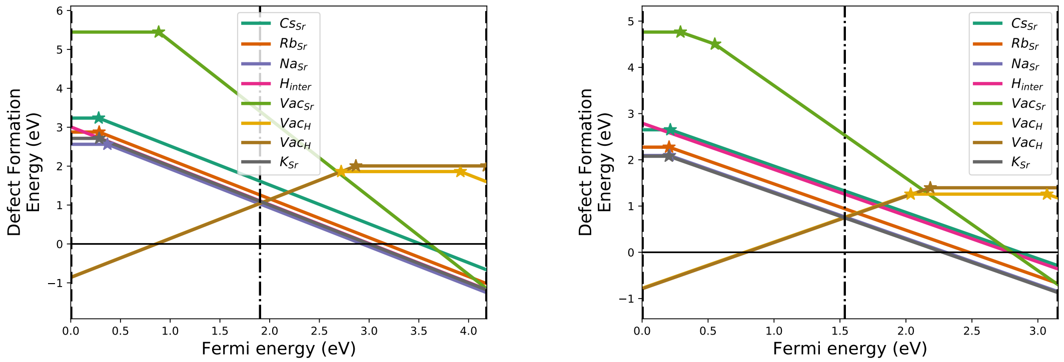

(a) Hybrid Benchmark **(b)** no_bes

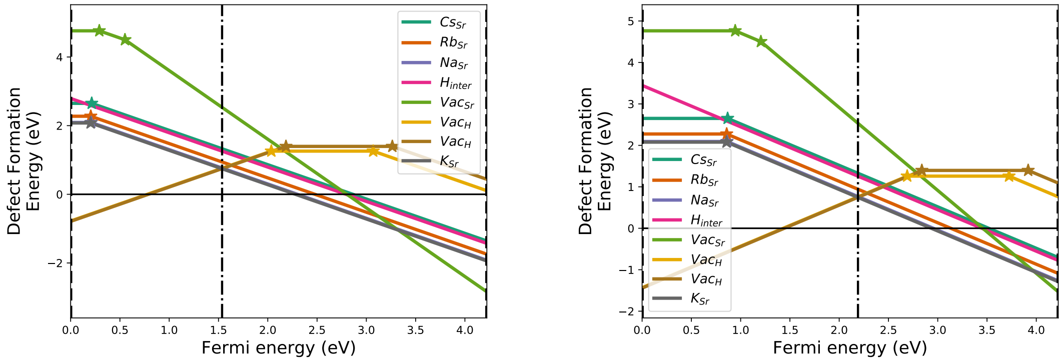

(c) BS_bes **(d)** bes

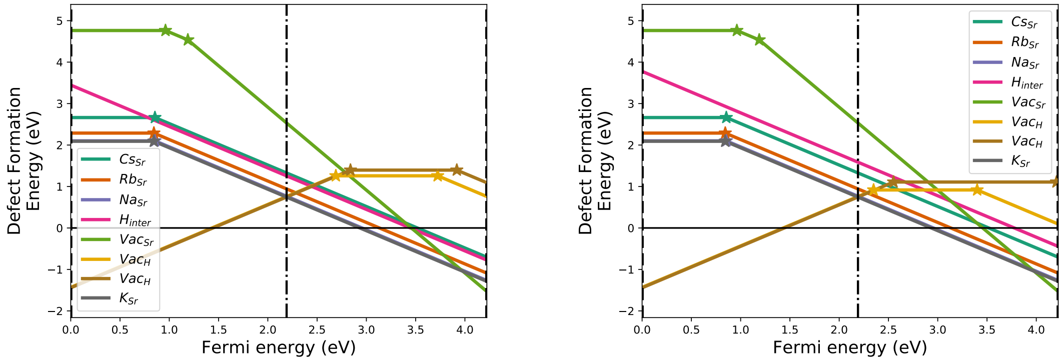

(e) dls1 **(f)** dls2

Figure F.2: SrH2_orthorhombic

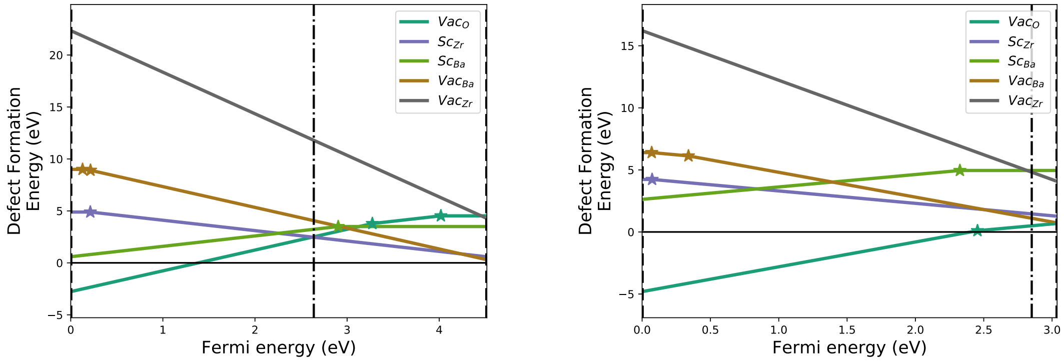

(a) Hybrid Benchmark **(b)** no_bes

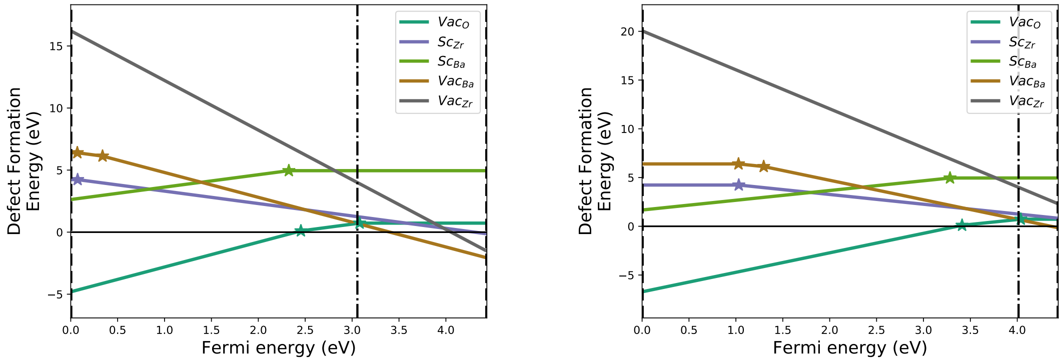

(c) BS_bes **(d)** bes

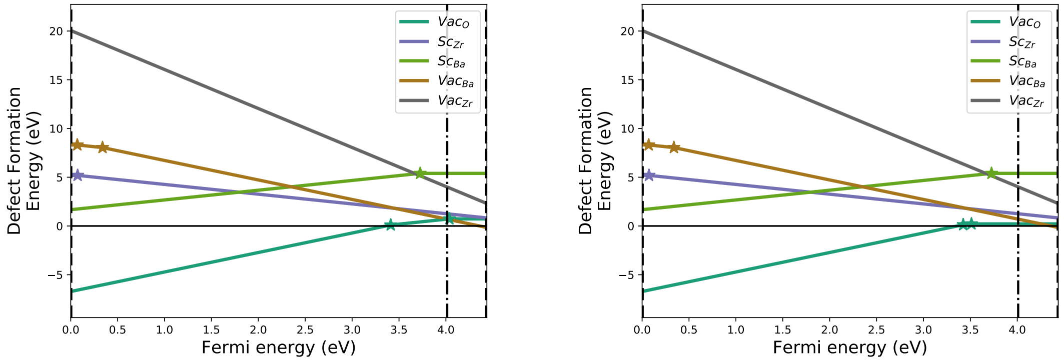

(e) dls1 **(f)** dls2

Figure F.3: BaZrO3_cubic

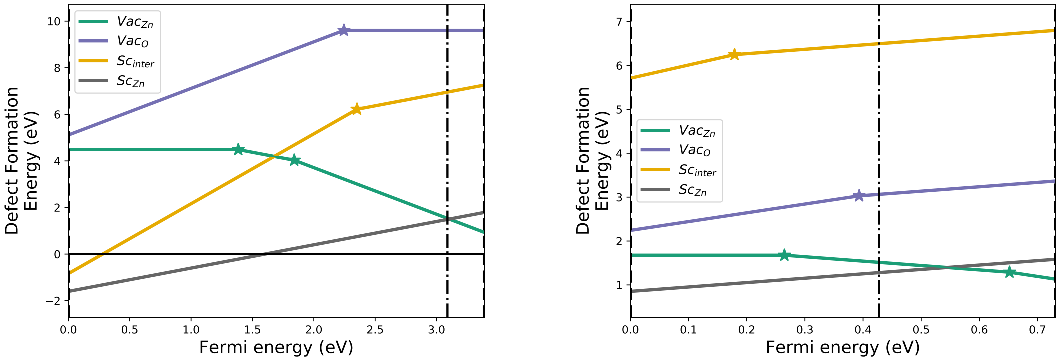

(a) Hybrid Benchmark **(b)** no_bes

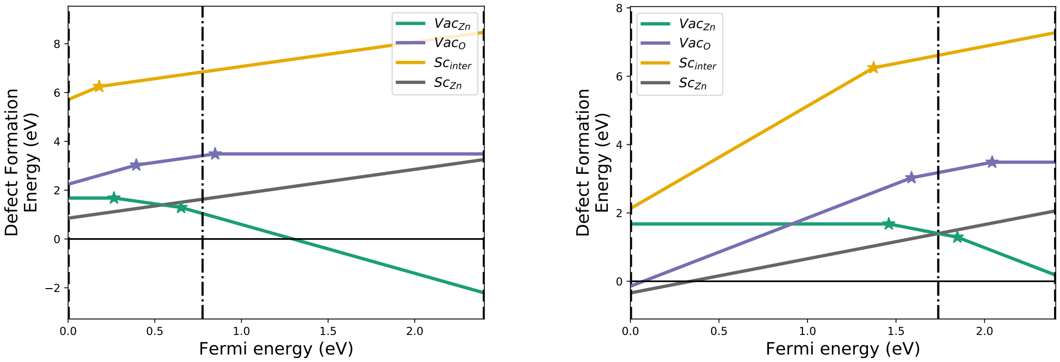

(c) BS_bes **(d)** bes

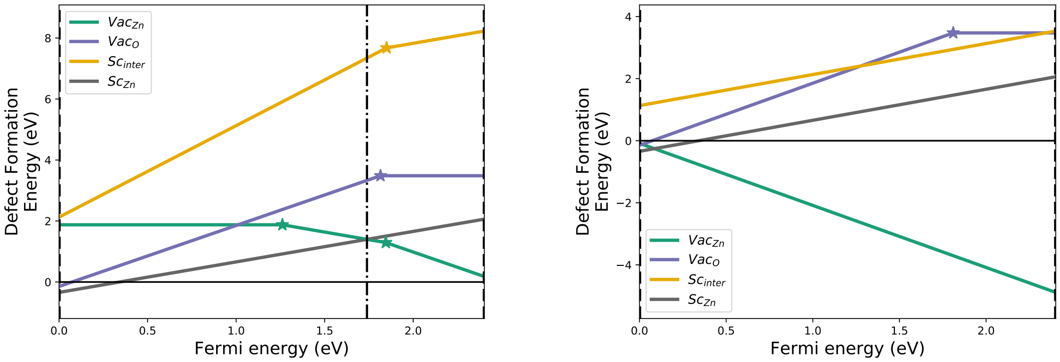

(e) dls1 **(f)** dls2

Figure F.4: ZnO_hexagonal

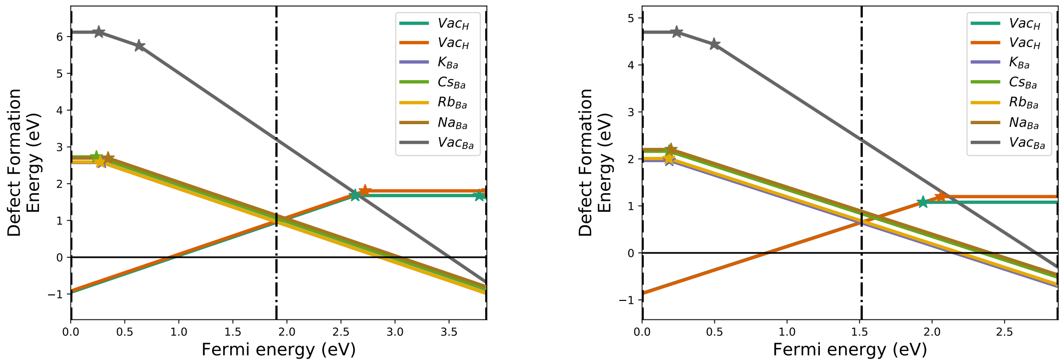

(a) Hybrid Benchmark **(b)** no_bes

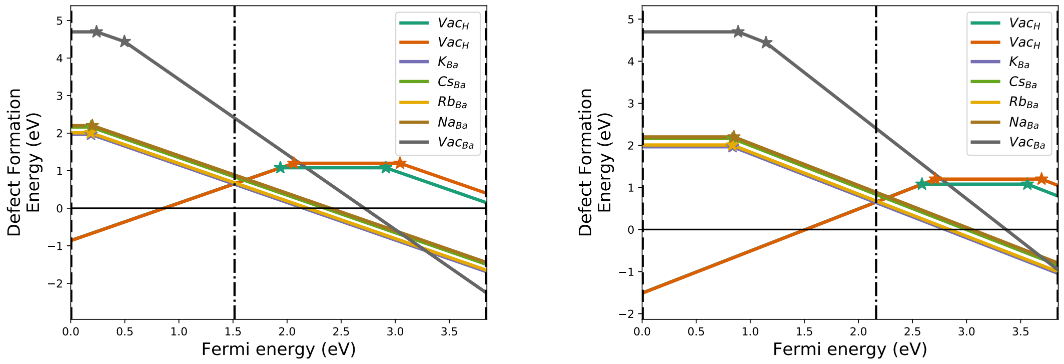

(c) BS_bes **(d)** bes

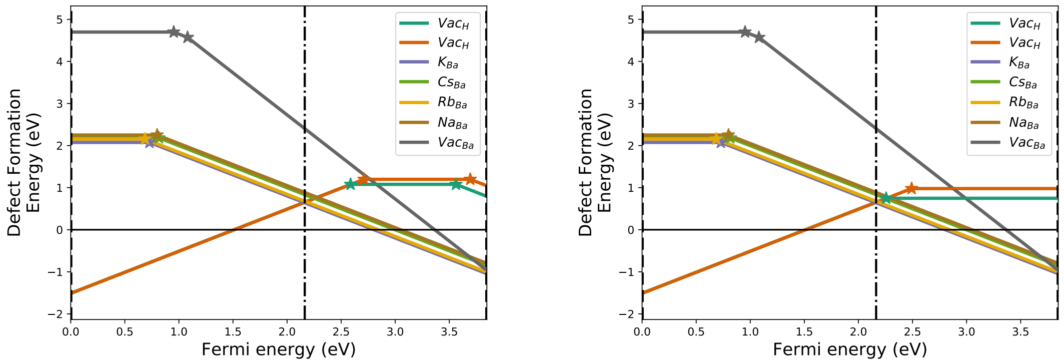

(e) dls1 **(f)** dls2

Figure F.5: BaH2_orthorhombic

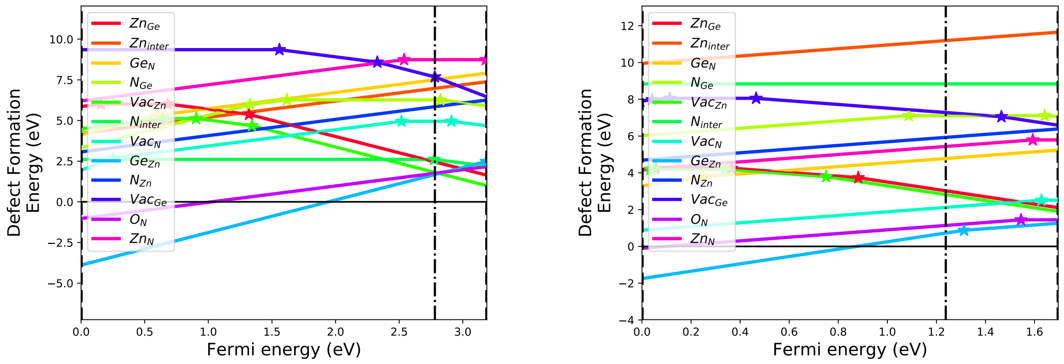

(a) Hybrid Benchmark

(b) no_bes

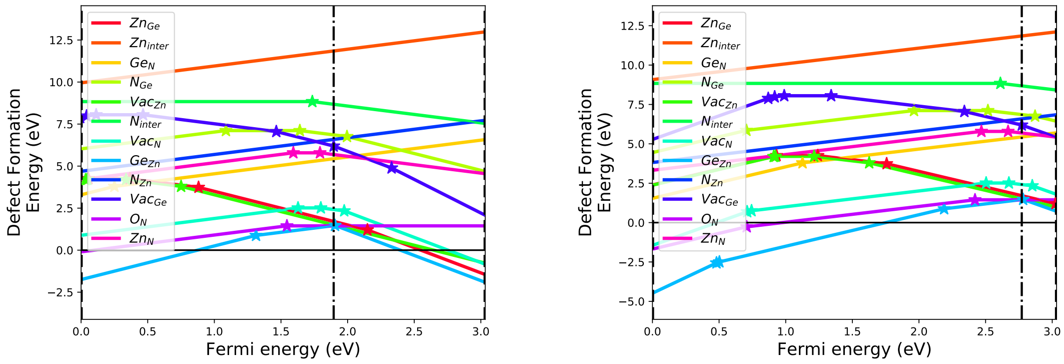

(c) BS_bes

(d) bes

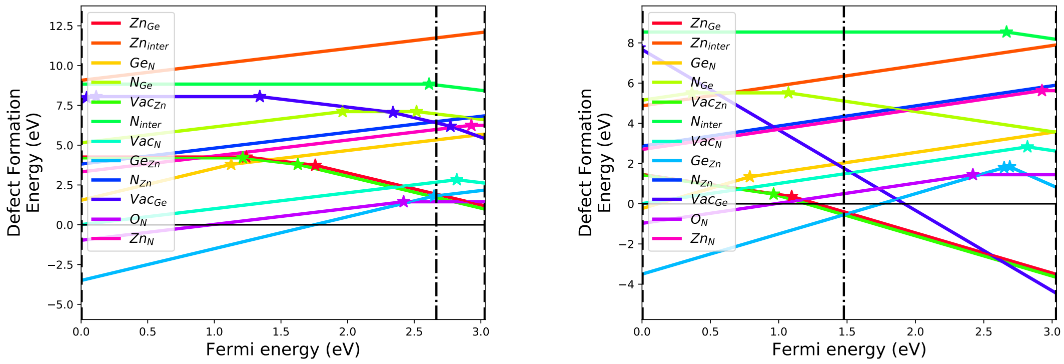

(e) dls1

(f) dls2

Figure F.6: ZnGeN2_orthorhombic

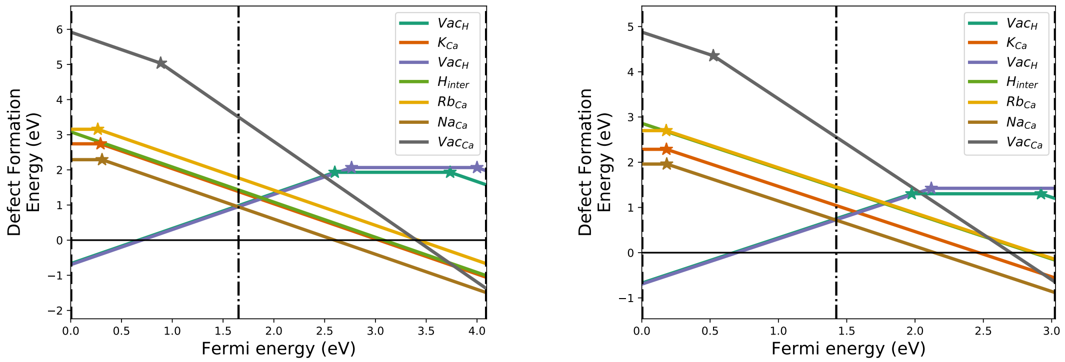

(a) Hybrid Benchmark **(b)** no_bes

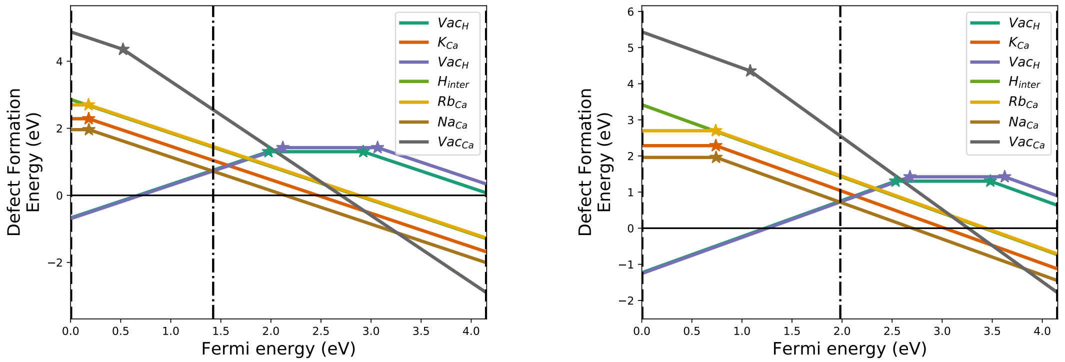

(c) BS_bes **(d)** bes

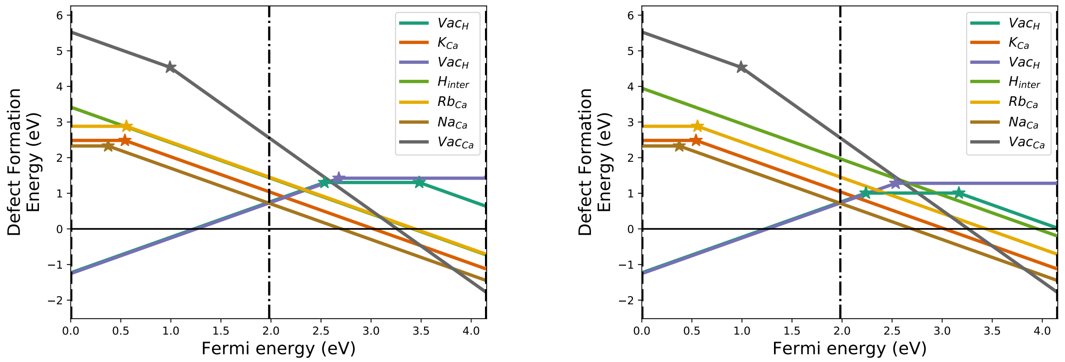

(e) dls1 **(f)** dls2

Figure F.7: CaH2_orthorhombic

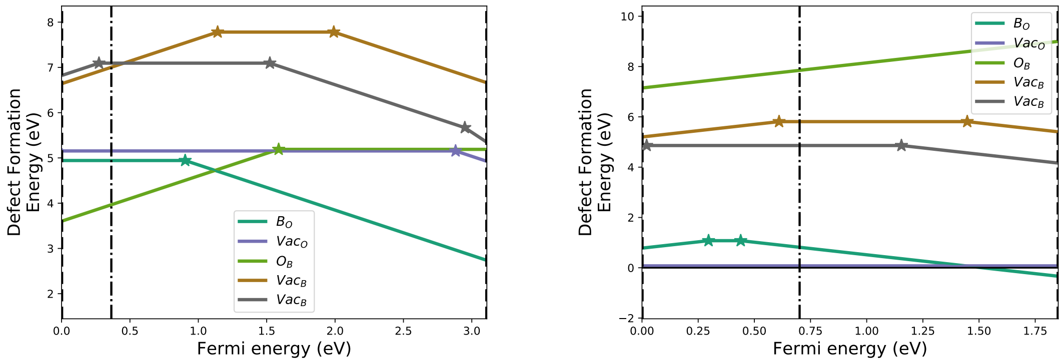

(a) Hybrid Benchmark **(b)** no_bes

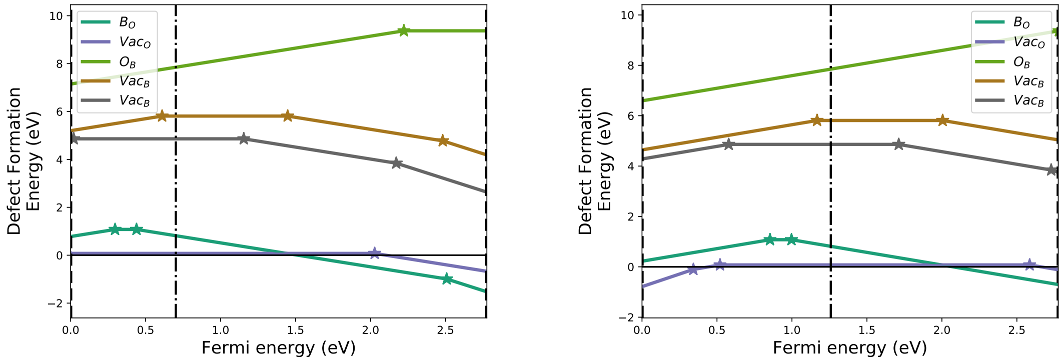

(c) BS_bes **(d)** bes

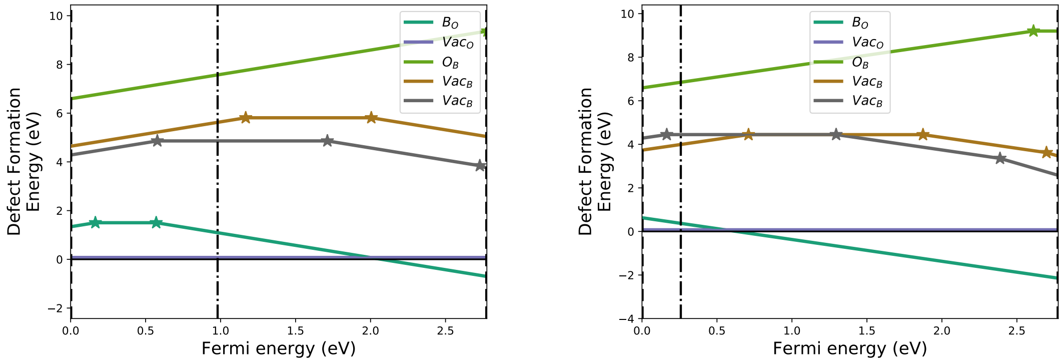

(e) dls1 **(f)** dls2

Figure F.8: B6O_trigonal

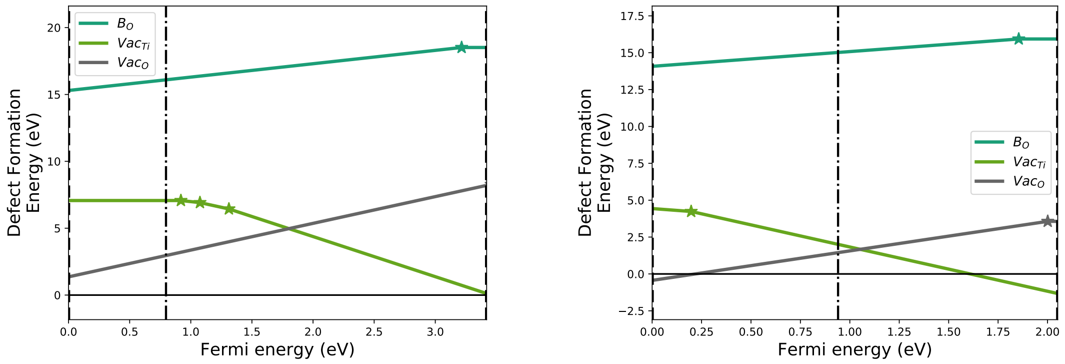

(a) Hybrid Benchmark **(b)** no_bes

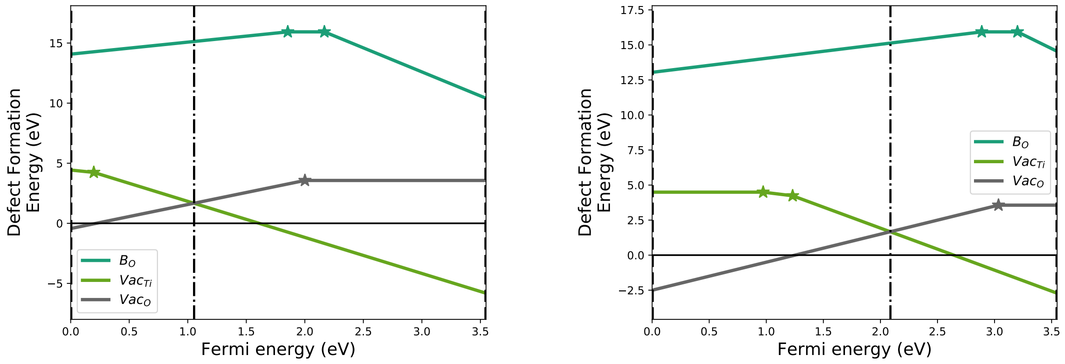

(c) BS_bes **(d)** bes

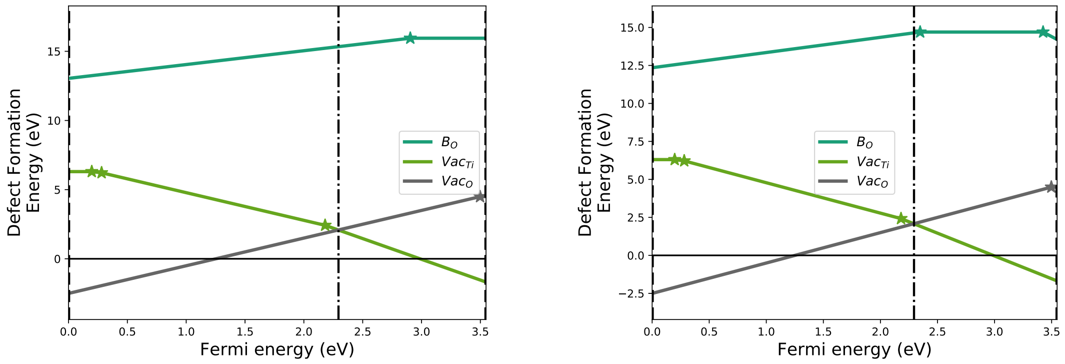

(e) dls1 **(f)** dls2

Figure F.9: TiO2_tetragonal

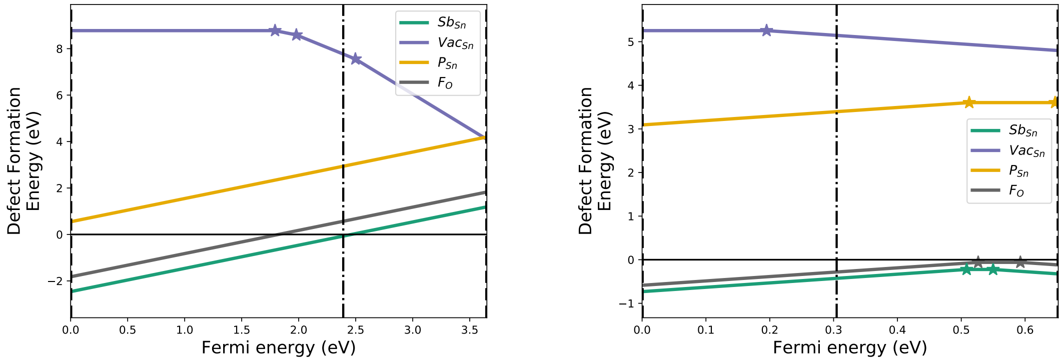

(a) Hybrid Benchmark **(b)** no_bes

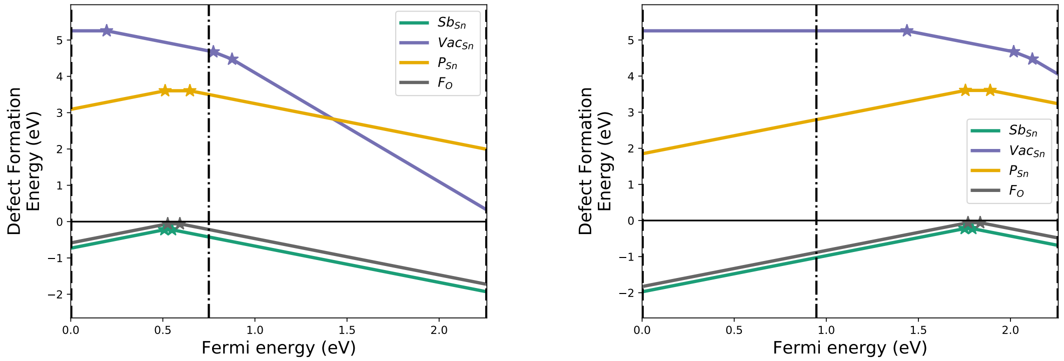

(c) BS_bes **(d)** bes

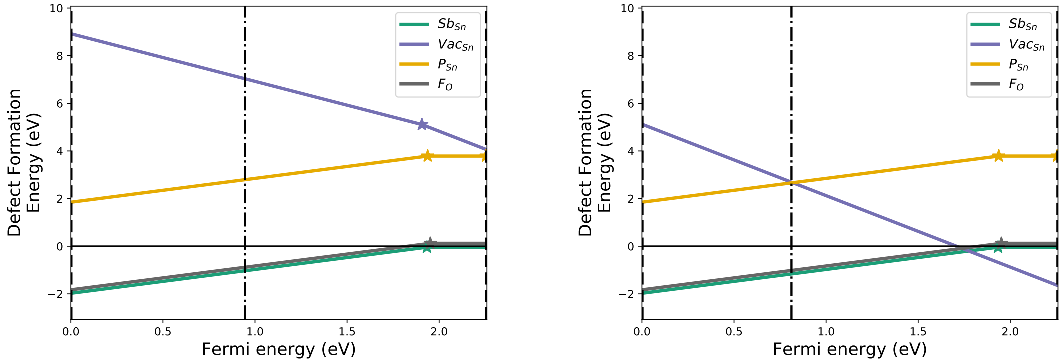

(e) dls1 **(f)** dls2

Figure F.10: SnO2_tetragonal (Fermi levels determined without Sb_{Sn} or F_O defects)

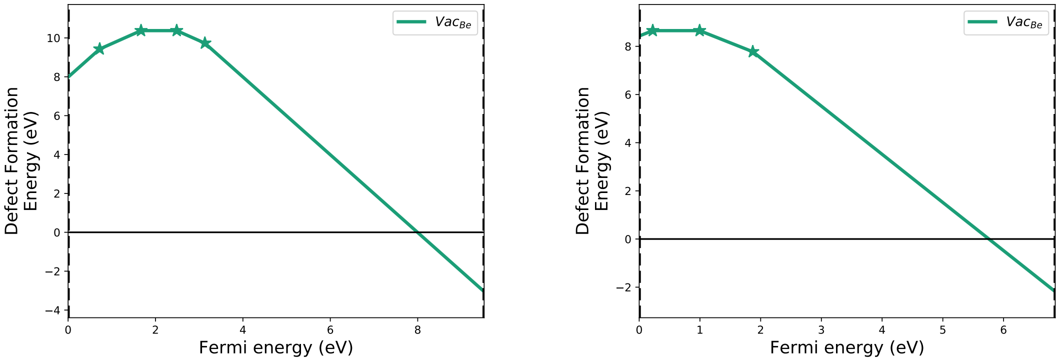

(a) Hybrid Benchmark **(b)** no_bes

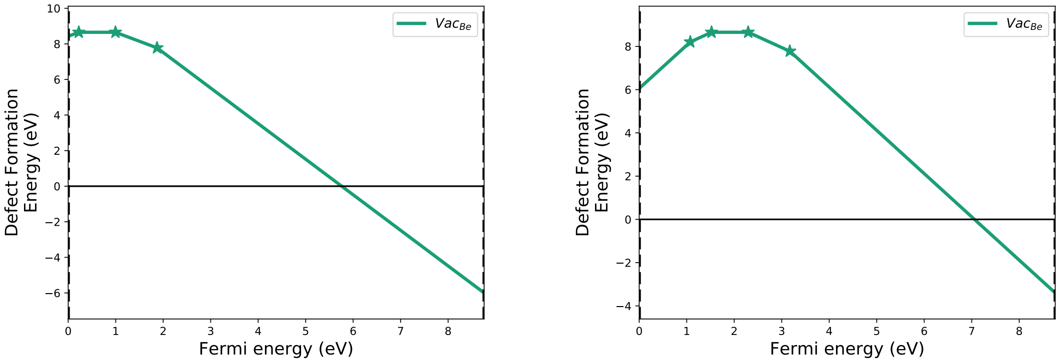

(c) BS_bes **(d)** bes

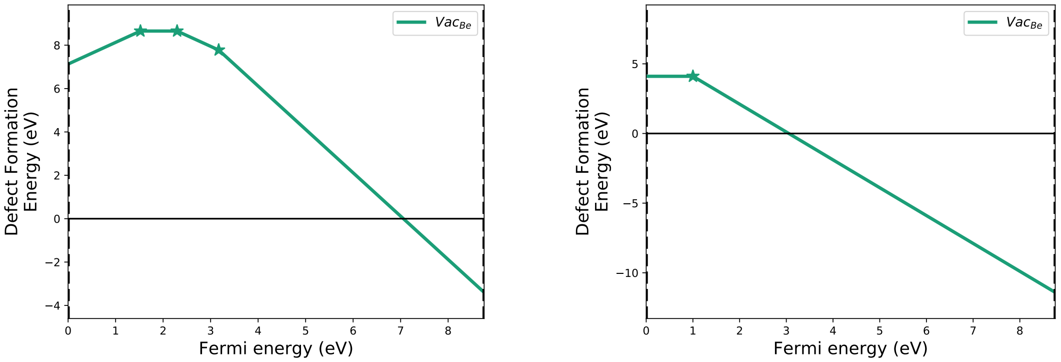

(e) dls1 **(f)** dls2

Figure F.11: BeO_cubic

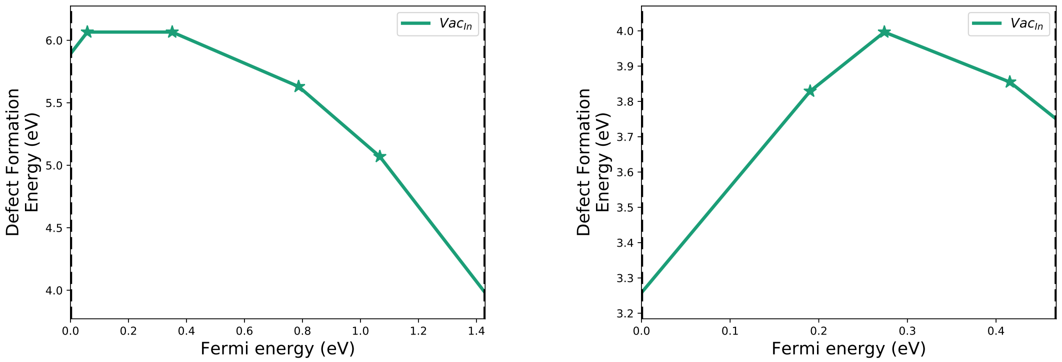

(a) Hybrid Benchmark **(b)** no_bes

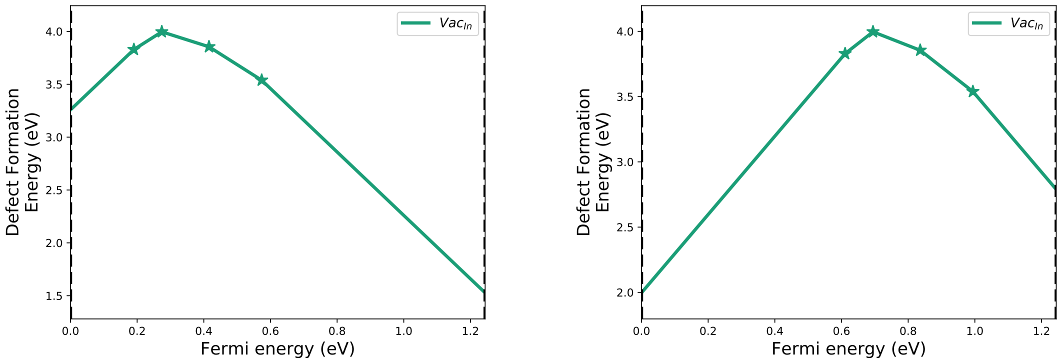

(c) BS_bes **(d)** bes

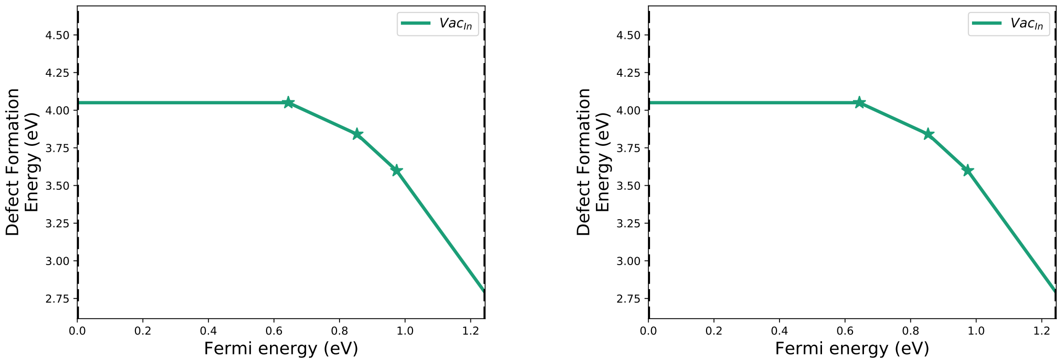

(e) dls1 **(f)** dls2

Figure F.12: InP_cubic

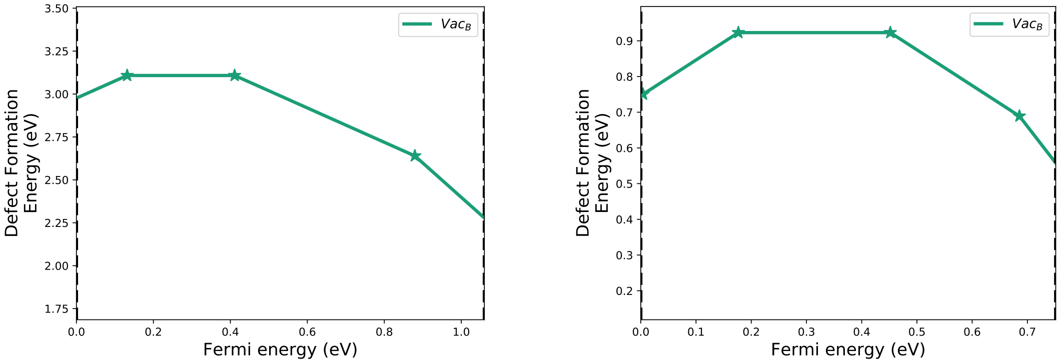

(a) Hybrid Benchmark **(b)** no_bes

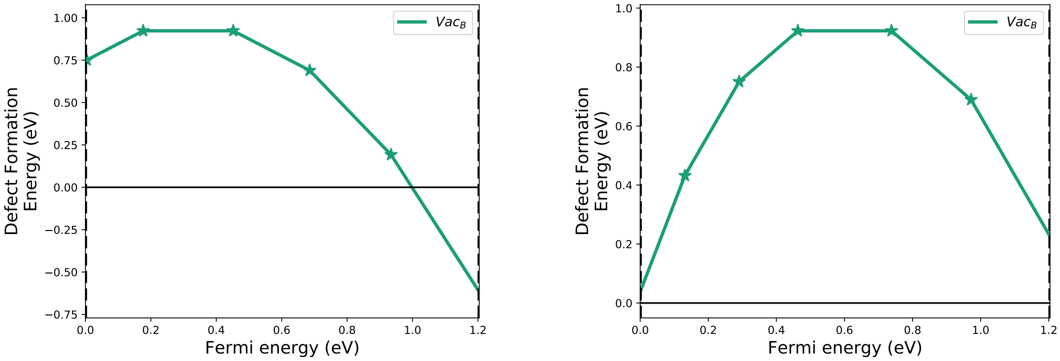

(c) BS_bes **(d)** bes

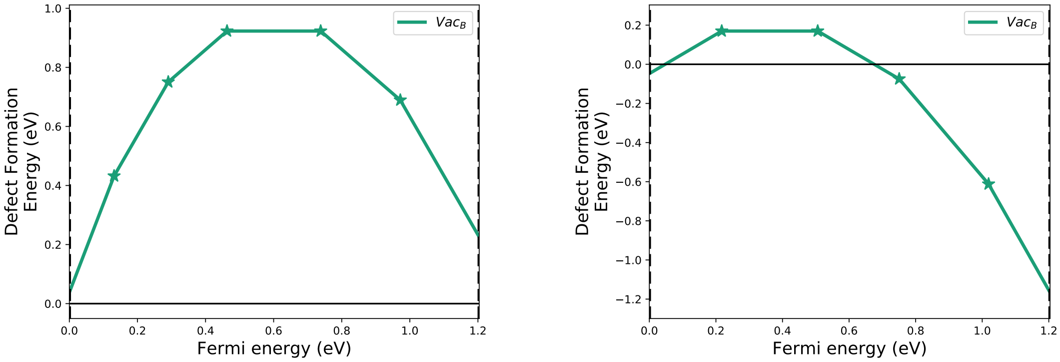

(e) dls1 **(f)** dls2

Figure F.13: BSb_cubic

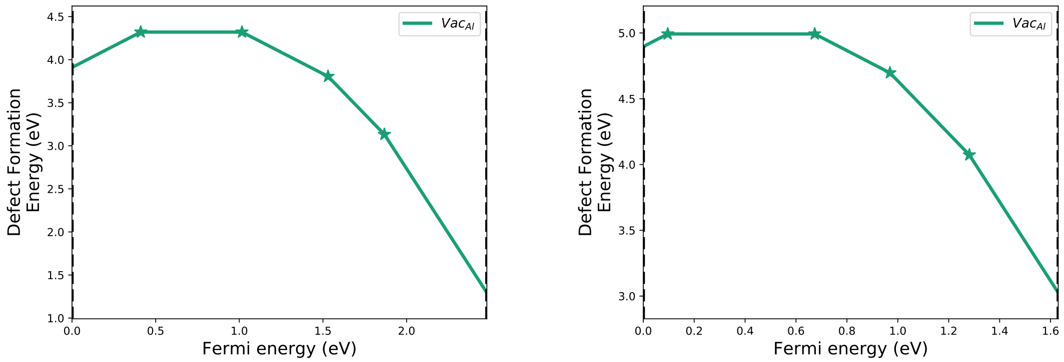

(a) Hybrid Benchmark (b) no_bes

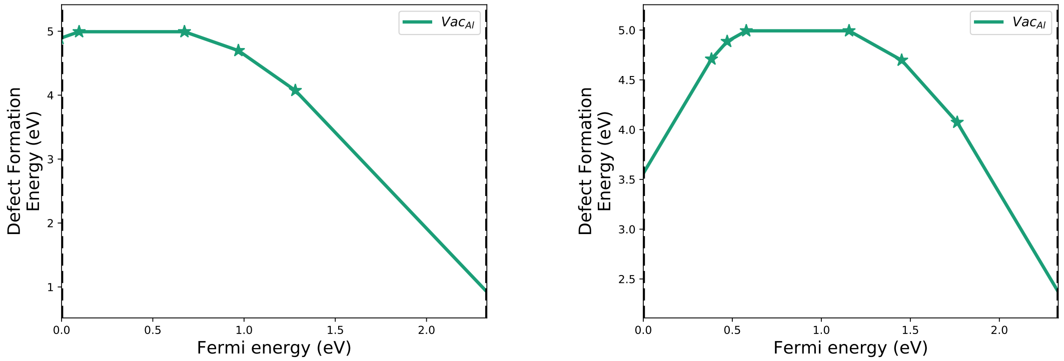

(c) BS_bes (d) bes

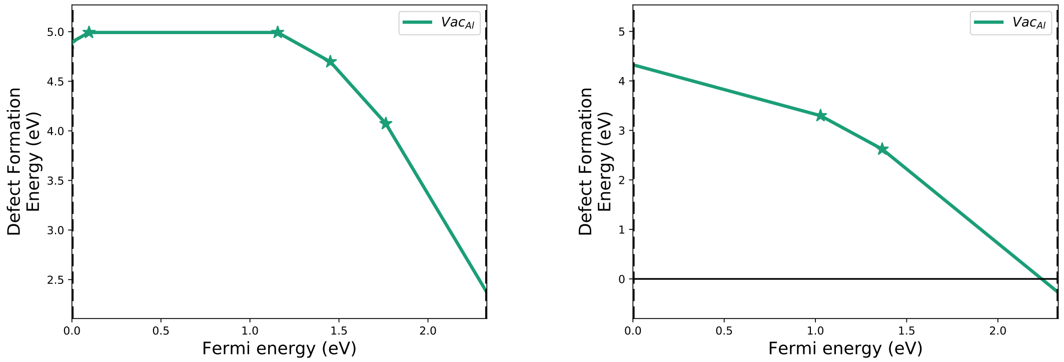

(e) dls1 (f) dls2

Figure F.14: AlP_cubic

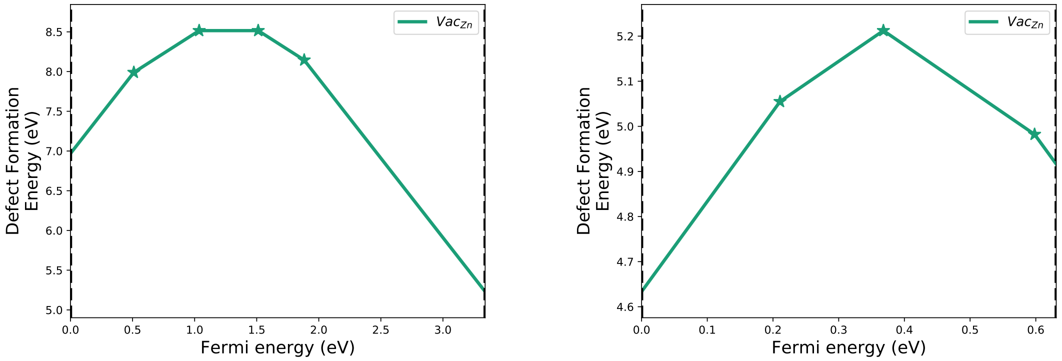

(a) Hybrid Benchmark **(b)** no_bes

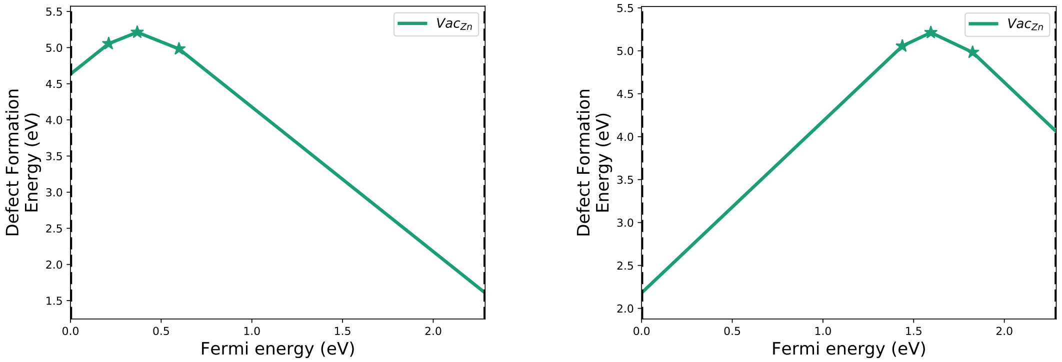

(c) BS_bes **(d)** bes

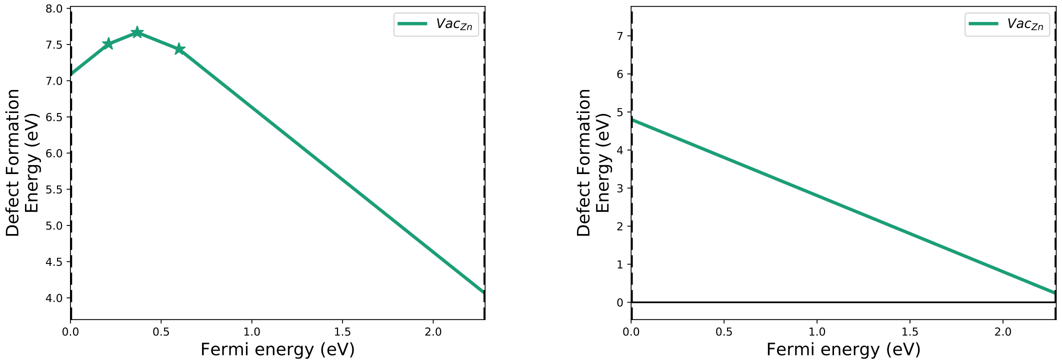

(e) dls1 **(f)** dls2

Figure F.15: ZnO_cubic

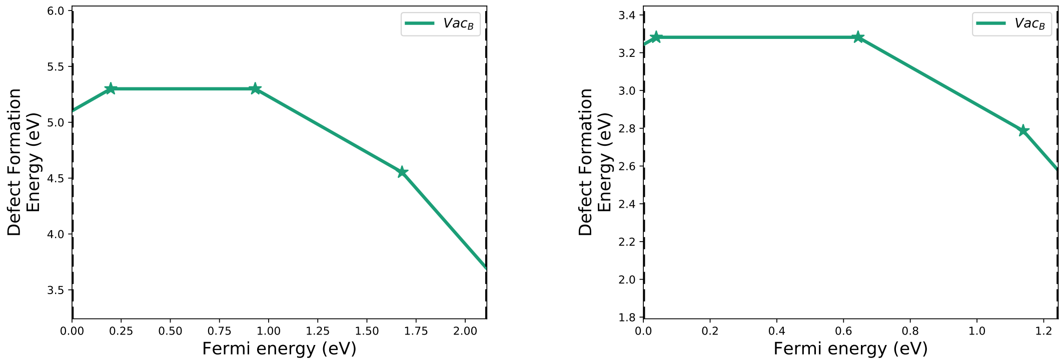

(a) Hybrid Benchmark **(b)** no_bes

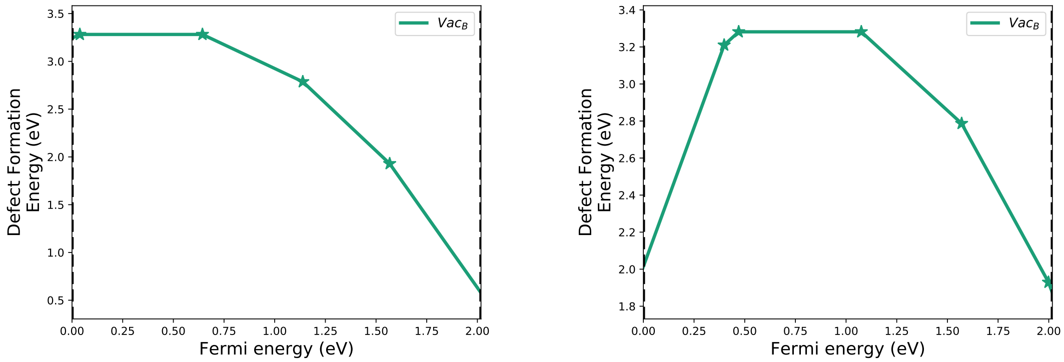

(c) BS_bes **(d)** bes

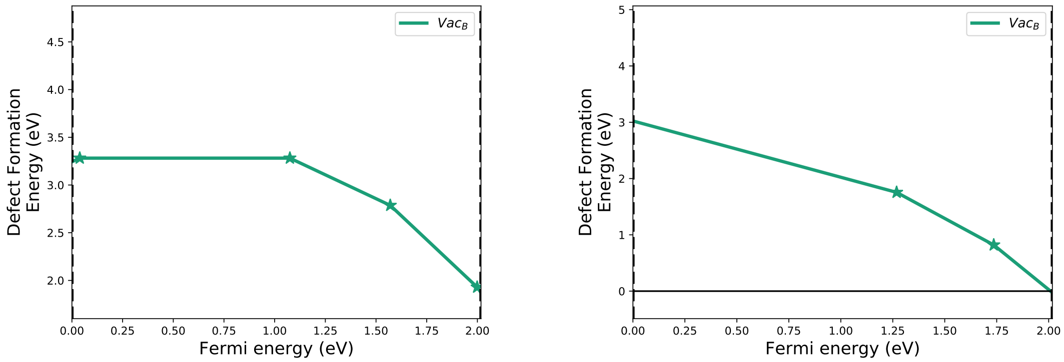

(e) dls1 **(f)** dls2

Figure F.16: BP_cubic

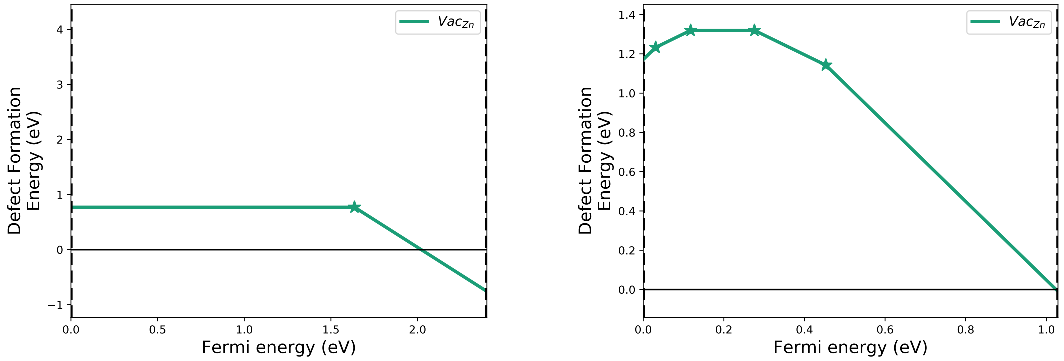

(a) Hybrid Benchmark (b) no_bes

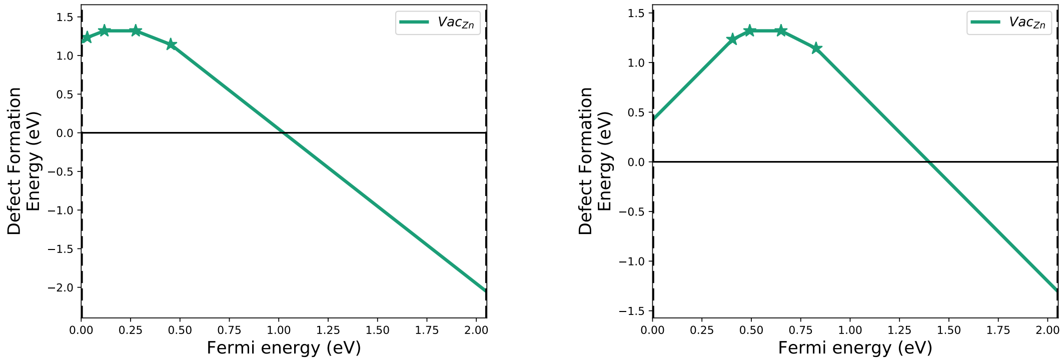

(c) BS_bes (d) bes

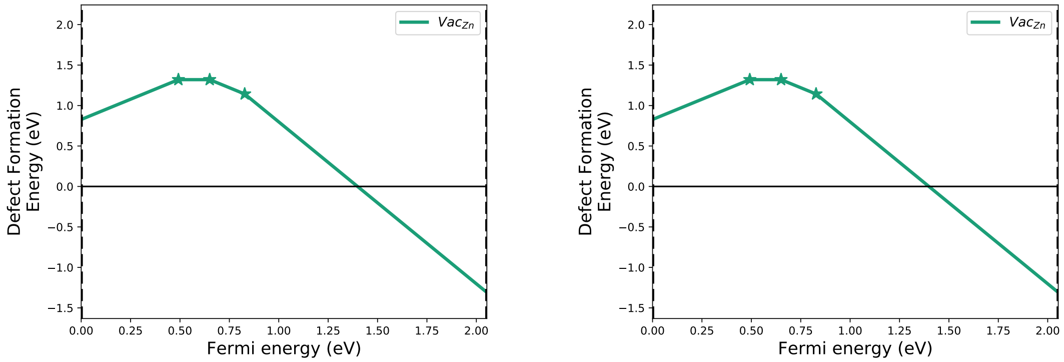

(e) dls1 (f) dls2

Figure F.17: ZnTe_cubic

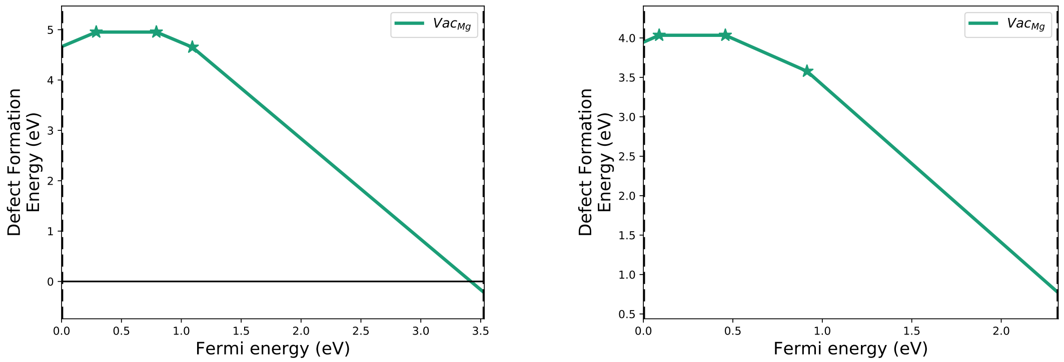

(a) Hybrid Benchmark **(b)** no_bes

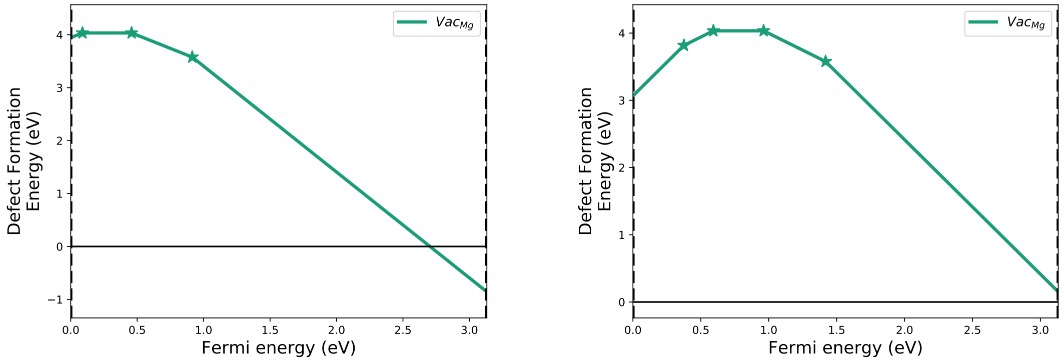

(c) BS_bes **(d)** bes

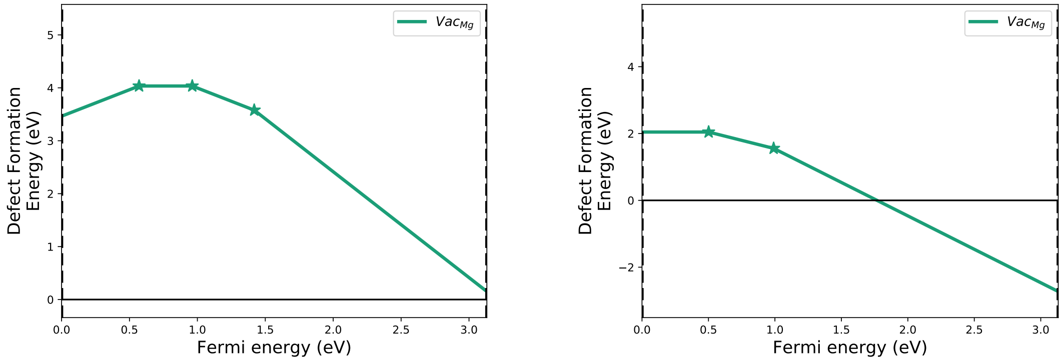

(e) dls1 **(f)** dls2

Figure F.18: MgTe_cubic

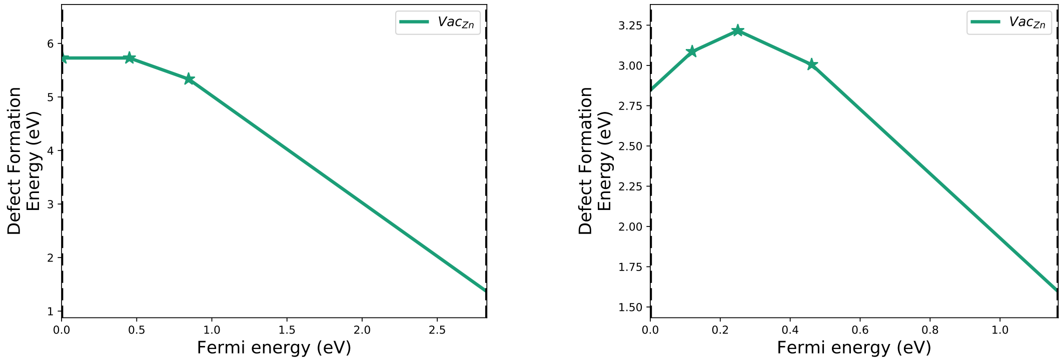

(a) Hybrid Benchmark

(b) no_bes

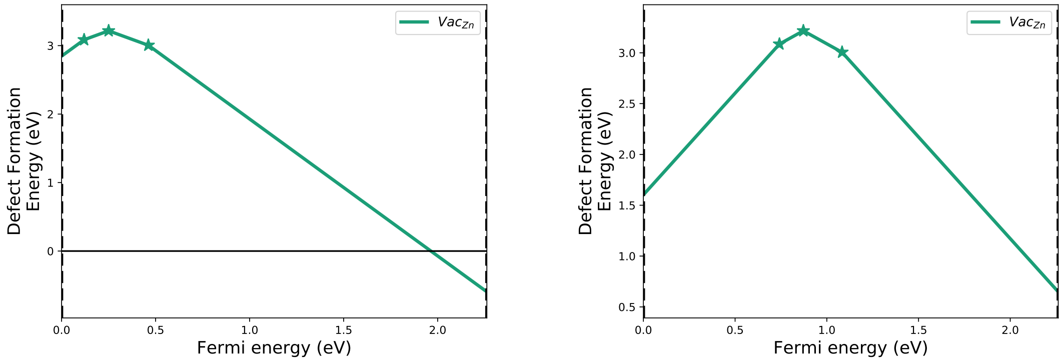

(c) BS_bes

(d) bes

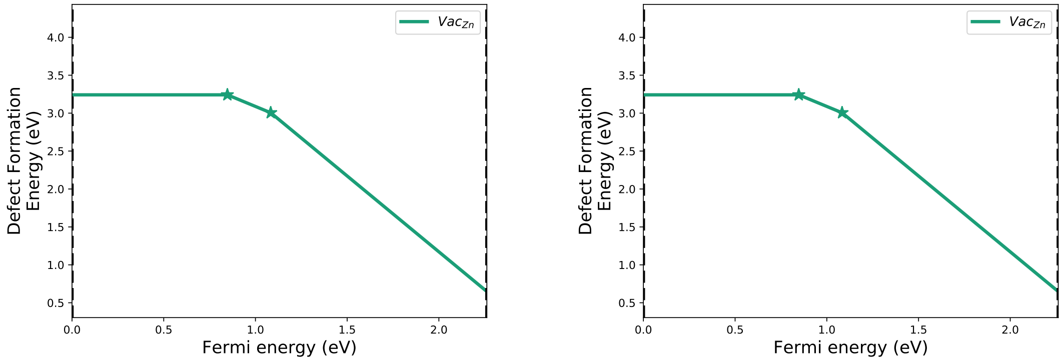

(e) dls1

(f) dls2

Figure F.19: ZnSe_cubic

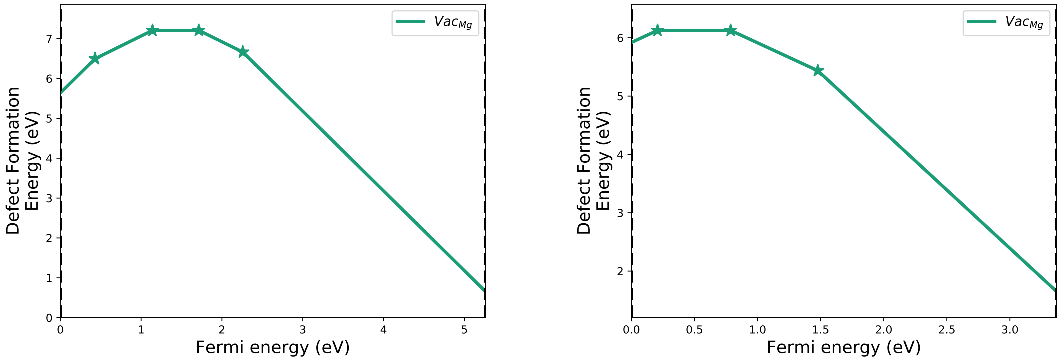

(a) Hybrid Benchmark **(b)** no_bes

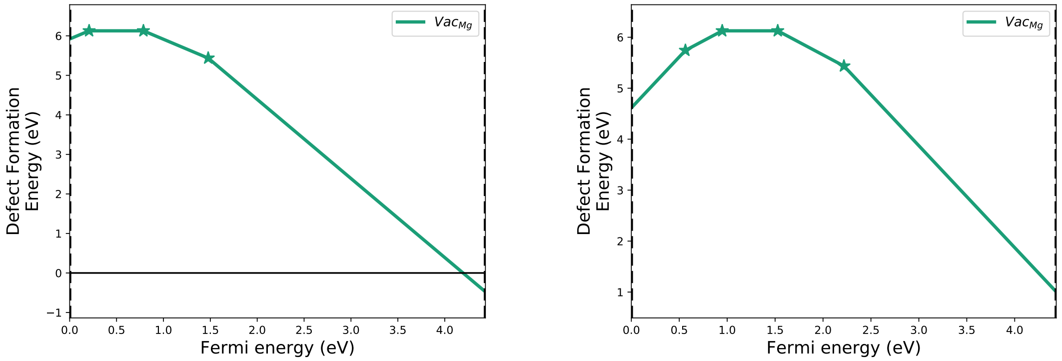

(c) BS_bes **(d)** bes

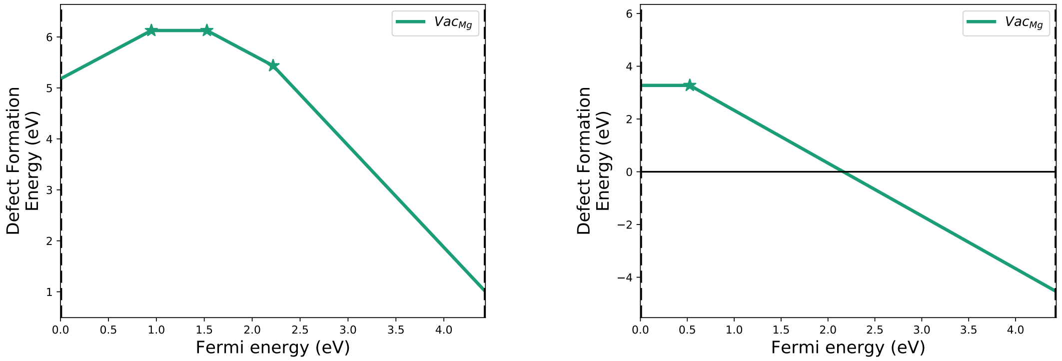

(e) dls1 **(f)** dls2

Figure F.20: MgS_cubic

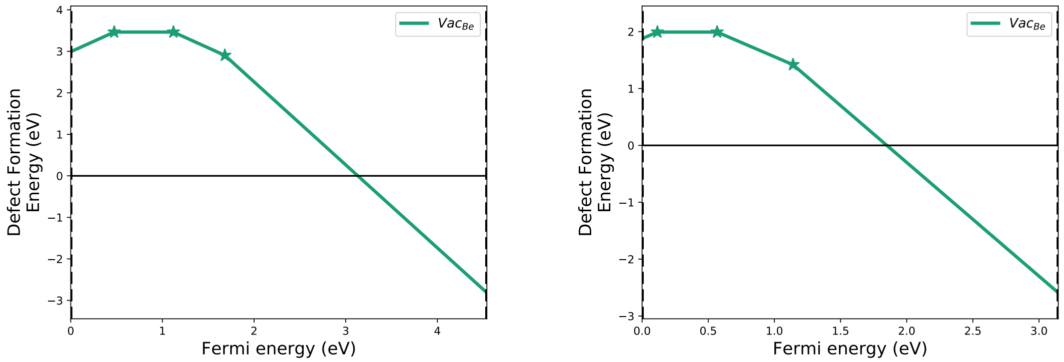

(a) Hybrid Benchmark (b) no_bes

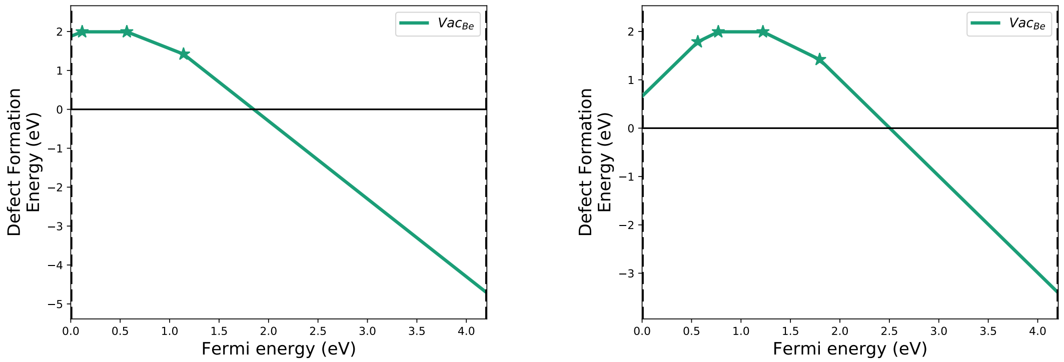

(c) BS_bes (d) bes

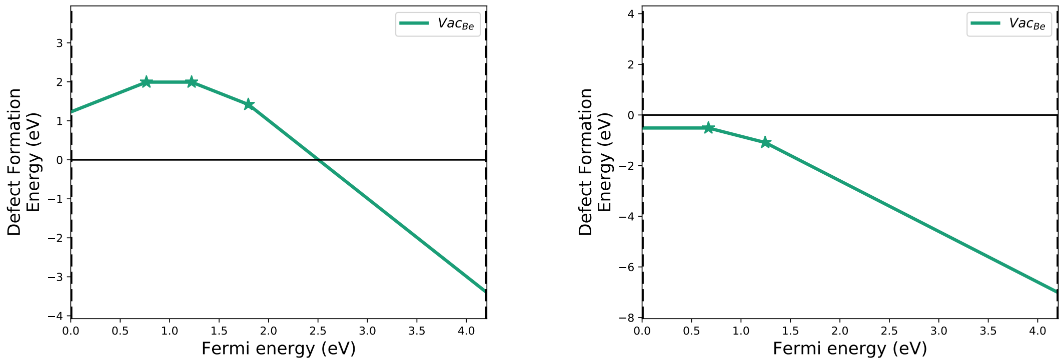

(e) dls1 (f) dls2

Figure F.21: BeS_cubic

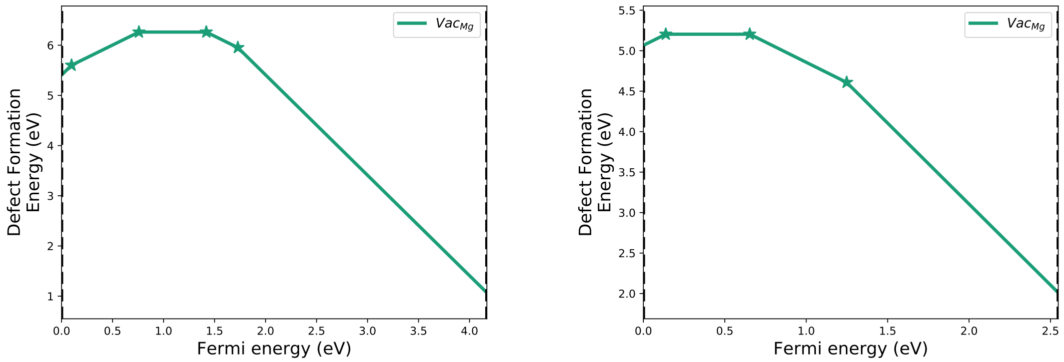

(a) Hybrid Benchmark **(b)** no_bes

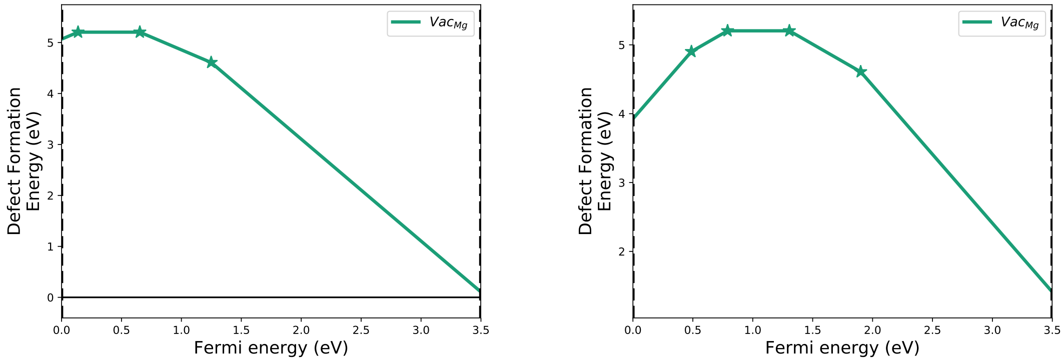

(c) BS_bes **(d)** bes

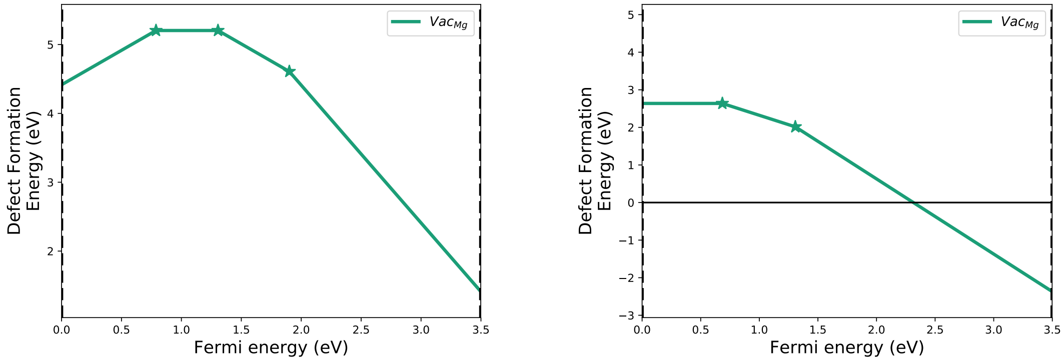

(e) dls1 **(f)** dls2

Figure F.22: MgSe_cubic

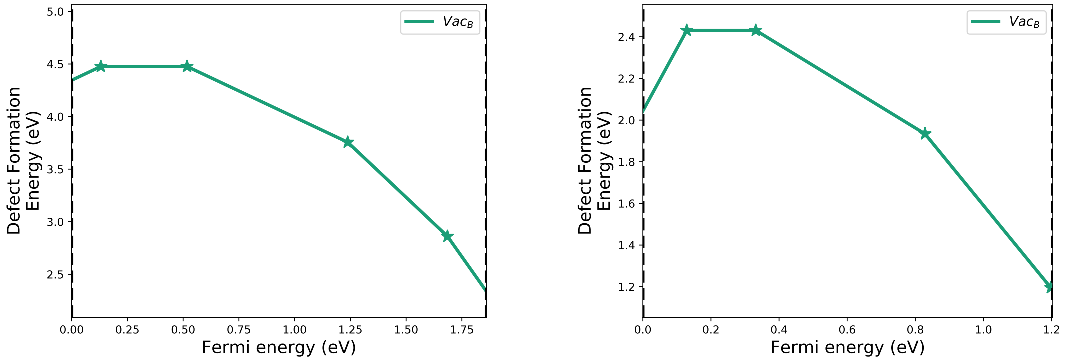

(a) Hybrid Benchmark **(b)** no_bes

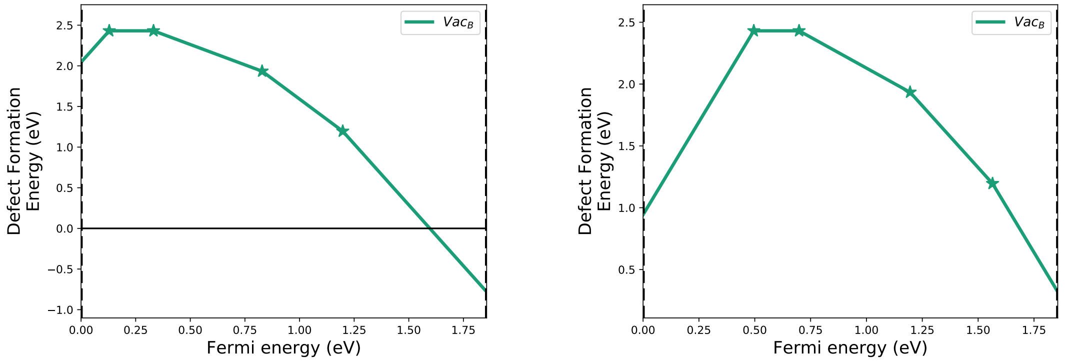

(c) BS_bes **(d)** bes

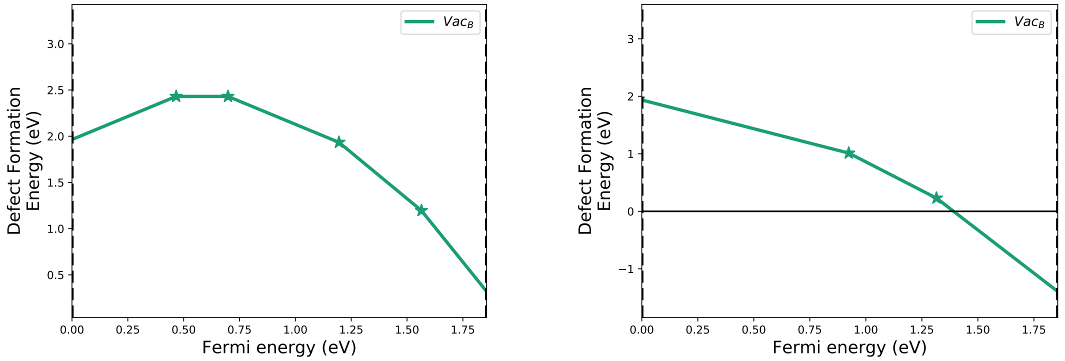

(e) dls1 **(f)** dls2

Figure F.23: BAs_cubic